12-2008

# An Investigation on Spot-Weld Modeling Complexity for Crash Simulation

Srinivasan Vimalanathan
*Clemson University*, congition_sv@yahoo.com

# AN INVESTIGATION ON SPOT-WELDING COMPLEXITY FOR CRASH SIMULATION

---

A Thesis
Presented to
the Graduate School of
Clemson University

---

In Partial Fulfillment
of the Requirements for the Degree
Master of Science
Mechanical Engineering

---

by
Srinivasan Vimalanathan
December 2008

---

Accepted by:

Dr. Lonny L. Thompson, Committee Chair
Dr. Paul F. Joseph
Dr. Sherrill B. Biggers

ABSTRACT

In order to design car body structures which are safe during crash, modern automotive manufacturers perform both full-scale experimental crash tests and computer simulation of vehicle crash events using commercially available Finite Element Analysis (FEA) packages such as ABAQUS or LS-DYNA. Use of crash simulations significantly reduces the number of real time crash experiments needed and reduces the time required for design changes. However, in order to capture accurately crash behavior during high-speed impact, a large amount of detailed FEA modeling features such as number and types of elements, mesh element size, number of components, different types of connectors, material properties, and other detailed features are needed. Crash simulation requires explicit time-stepping procedures, which can be computationally expensive for complicated full vehicle models with many components.

An important feature in crash simulation is the amount of detail included in modeling spot weld connections. Traditionally for efficiency, simple node-to-node rigid connections for modeling spot weld connections between different components are used, especially when many components are connected in a full vehicle crash model. Recent studies have shown the importance of accurate modeling including elastic stiffness and failure modes for spot welds due to high impact loads in automotive crash analysis. For efficiency and convenience, most commercially available FEA packages now include the option of creating mesh independent spot welds, which allow the user to define the location of the center point of the spot weld and define the spot weld radius on adjacent surfaces of connected components. A distributed coupling to nodes within the radius

specified is automatically created which approximates the behavior of a spot weld of finite size. In addition, the size of the rigid spot weld model provides greater accuracy compared to the simple node-to-node connection. However, it has not been until very recent that some researchers and commercially available FEA software have the ability to include important spot weld elastic properties and failure modes combining pull, peal, shear, and torsion.

In this work, different levels of complexity in spot weld modeling are examined in terms of sufficient accuracy which can be used efficiently for impact analysis of large connected components and full vehicle crash models. In order of increasing complexity, the following spot weld models are considered and results compared: (a) simple node-to-node rigid connection, (b) rigid mesh independent spot welds, (c) elastic mesh independent spot welds, and (d) elastic with failure mesh independent spot welds. In order to study the fundamental behavior of the different mesh-independent spot weld models, pullout and peal tests between two thin ductile steel plates are performed which isolate different failure modes. Comparisons of reaction force versus displacement curves and internal energy versus displacement for all the different spot weld models are given. Results indicate that the rigid connected results in peak reaction forces which are much larger than elastic spot welds. The spot weld model, which includes failure, follows the same path as the elastic weld but when reaching the particular failure force the reaction remains constant with additional applied displacement.

To better understand the behavior of the spot-weld models for crash analysis on a realistic and important automotive component which exhibits complex crushing modes

with combined axial and bending a frontal longitudinal rail designed for strength and energy absorption was studied with a node-to-node rigid spot weld compared with mesh independent rigid and elastic spot weld connections. The frontal longitudinal rail is a thin walled closed section located in between the front bumper and the firewall manufactured from two stamped sheets with spot welds on both sides of flanges at discrete intervals along the length. In addition to spot welds, the effect of various shape and size parameter changes including waves, beads, and a small rib for crush initiation that significantly increase energy absorption and crush force efficiency for the rail component are proposed.

# DEDICATION

I dedicate this thesis to my parents Vimalanathan Jayaraman and Surya Prabha Vimalanathan, and to Karuna Vimalanathan and Chiranjeevi Vimalanathan for their love and support.

# ACKNOWLEDGMENTS

I would like to express my deepest gratitude to Dr. Lonny L. Thompson, my research advisor, who supported me throughout my thesis with his patience and knowledge. I could not have done this without his guidance. I would like to thank Dr. Paul Joseph and Dr. Sherrill Biggers for serving on my committee and their support.

I am thankful to Mr. Pierre Burgers for providing me an opportunity to work at Dassault Systemes SIMULIA (ABAQUS) has intern. I would like to thank Mr. Sridhar Sankar and Mr. Martin Roswall for their support and guidance throughout my tenure at SIMULIA.

Furthermore, I would like to thank my lab mate Maya Ramachandran, for nurturing a healthy and learning work environment and finally I would like to thank my roommate Bhaskar Pandurangan for making my stay in Clemson enjoyable and unforgettable.

TABLE OF CONTENTS

Page

Table of Contents (Continued)

Page

LIST OF TABLES

LIST OF FIGURES

List of Figures (Continued)

List of Figures (Continued)

List of Figures (Continued)

List of Figures (Continued)

List of Figures (Continued)

Figure Page

# CHAPTER ONE

# INTRODUCTION

The vehicle body structure forms the foundation for automobiles and serves many functions, including strength, a stable platform for mounting components and crash safety features in case of impact. The behavior of such structures during the frontal crash depends on the joints between the various connected components which make-up the body structure. For low-cost manufacturing of automotive bodies for mass production, the vast majority of vehicles are constructed from stamped low to medium strength steel sheet materials. To form complicated shapes, stamped sheets are most often welded together to form the body and other components. For automated, fast and efficient connections, spot welds are most often used.

In order to design car body structures which are safe during crash, modern automotive manufacturers perform both full-scale experimental crash tests and computer simulation of vehicle crash events using commercially available Finite Element Analysis (FEA) packages such as ABAQUS or LS-DYNA. Use of crash simulations significantly reduces the number of real time crash experiments needed and reduces the time required for design changes. However, in order to capture accurately crash behavior during high-speed impact, a large amount of detailed FEA modeling features such as number and types of elements, mesh element size, number of components, different types of connectors, material properties, and other detailed features are needed. Crash simulation requires explicit time-stepping procedures, which can be computationally expensive for complicated full vehicle models with many components. Therefore, when simulating the

crash of an entire vehicle using commercially available FEA packages spot welds behavior plays an important role in the output obtained. Typically, thousands of spot welds are required to join all parts and components to form the body frame. During a crash event, body structures are designed to crush in a controlled manner in order to provide energy absorption, avoid penetration, and reduce peak accelerations to the occupants. During crush, spot welds between joined stamped sheets may fail. Therefore, properties of the spot-weld joints especially during failure behavior play an important role in crash simulation. The role of spot-weld modeling in the simulation of crash analysis has become an important topic in world-class automotive companies at the leading edge of technology for crash safety such as BMW and Ford. The importance of accurate and efficient spot-weld models in industry has urged the FEA commercial software package developers to add new features that are convenient and accurate in creating the spot welds in finite element models.

An important feature in crash simulation is the amount of detail included in modeling spot weld connections. Traditionally for efficiency, simple node-to-node rigid connections for modeling spot weld connections between different components are used, especially when many components are connected in a full vehicle crash model. Recent studies have shown the importance of accurate modeling including elastic stiffness and failure modes for spot welds due to excessive loads in automotive crash analysis. For efficiency and convenience, many commercially available FEA packages now include the option of creating mesh independent spot welds, which allow the user to define the location of the center point of the spot weld and define the spot weld radius on adjacent

surfaces of connected components. A distributed coupling to nodes within the radius specified is automatically created which approximates the behavior of a rigid spot weld of finite size. In addition, the size of the rigid spot weld model provides greater accuracy compared to the simple node-to-node connection. However, it has not been until very recent that some researchers and commercially available FEA software have the ability to include important spot weld elastic properties and failure modes combining pull, peal, shear, and torsion. An example of this technology is the new mesh independent spot weld feature in the latest version of ABAQUS V6.8 from Simulia, which allows the analyst to create spot welds between thin shell element meshes with both elastic, and failure behavior which combines multiple load paths. In addition, ABAQUS includes generalized failure models which allow damage initiation for spot-welds

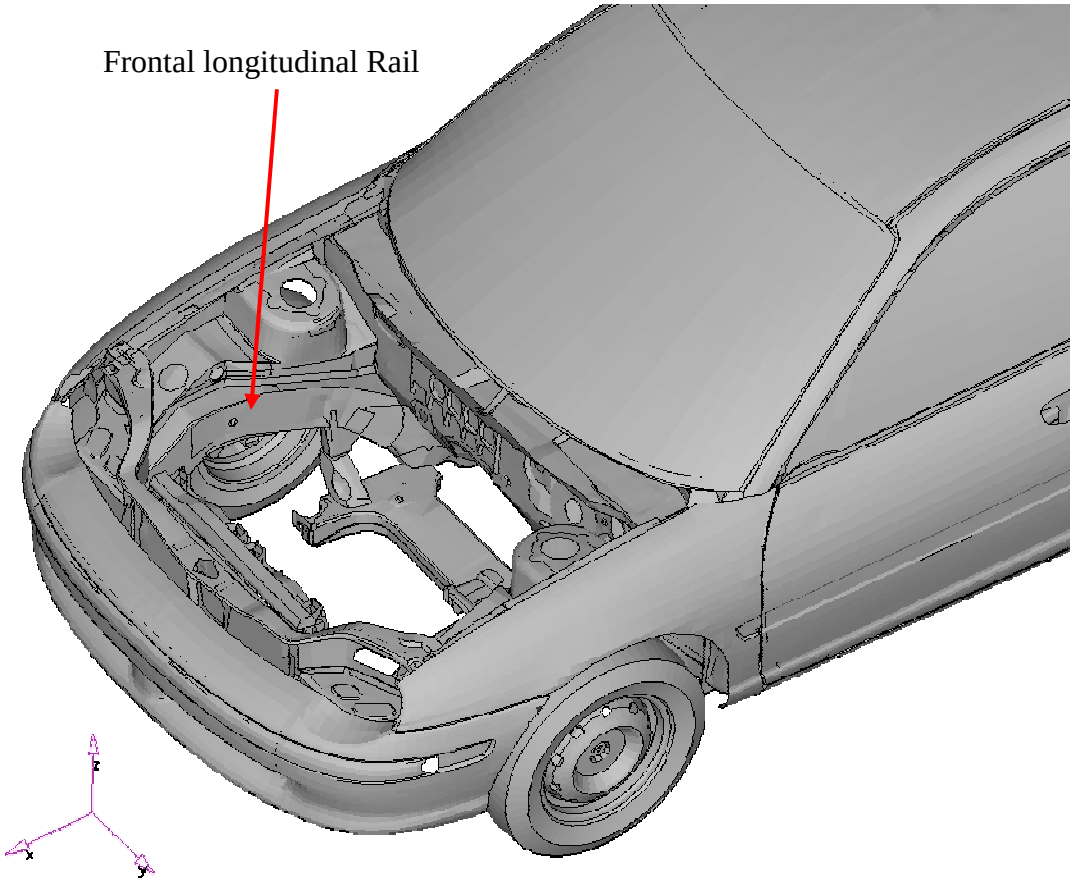


**Figure 1-1 Location of Frontal Longitudinal Rail of a Vehicle**

The front section of an automotive vehicle plays an important role in crash safety during a frontal collision or impact. In order to optimize the performance of the vehicle structure during a frontal collision the primary objective of a design engineer would be to design the frontal area with energy absorbing structures that reduce peak acceleration and forces in the occupant area. In most automotive vehicles, the front rails are major component of the vehicle structure that are designed to crush in a controllable manner and absorb kinetic energy during frontal collision. The frontal longitudinal rail is a thin walled closed section located in between the front bumper and the firewall manufactured

from two stamped sheets with spot welds on both sides of flanges at discrete intervals along the length. A key feature of the frontal longitudinal rail is that it acts as an energy absorber during frontal impact. During a frontal impact, typically 60% of the kinetic energy in the system is reduced by the plasticity of the vehicle's frame. This achievement is mainly due to the controlled crush deformation of the vehicle frontal structure [1]. For a 35mph frontal impact, the vehicle frontal region has a relatively large deformation of between 20-28 inches (0.50 m – 0.70 m).

## 1.1 Literature Review

The energy absorption in the frontal rail during crash is due to a combination of axial and bending collapse modes. The major challenge for engineers is to design a front rail that crushes axially because the axial collapse mode dissipates more energy during frontal crash when compared to the bending collapse mode. The frontal longitudinal rail is designed with more axial collapse mode by providing folds in the frontal area of the longitudinal rail. When considering individual components, an optimized design can often be achieved because of the relatively simple load paths and assumed boundary conditions. However, in case of a full vehicle, several factors like the number of components attached to the vehicle frame, variation in the material properties of the components and variation in the energy absorption of the components has to be considered ,and due to interaction, can be highly complicated. In addition, the boundary conditions and contact between surfaces vary continuously throughout the crash event in a very short time interval. The time taken for crash events is typically 200 ms. Therefore,

to predict the crash behavior of a complex structure during a frontal collision, one must characterize the crash energy management of the structure by determining the load carrying capacity or strength of each major component under various types of loading and collapse modes [2].

The crash energy management design deals with the many diverse systems of a vehicle. To optimize the energy flow in a vehicle during crash is a multidisciplinary process involving various components interacting closely with each other. While designing a vehicle for crashworthiness many diverse engineering disciplines such as biomechanics, structures, vehicle dynamics, packaging, engineering analysis and manufacturing must be considered. There are two major considerations in the design of automotive structures for crashworthiness, absorption of the kinetic energy of the vehicle and the crash resistance to sustain the crush process to maintain passenger compartment integrity. The desire for crashworthiness must be balanced with often competing goals of light weight for improved fuel economy and cost [3].

To increase energy absorption and improve fuel efficiency of the vehicle, weight reduction is one of the most effective approaches. The fuel consumption will decrease by 6 to 8% if a car weight is reduced by 10%. An automotive body structure weighs about 30 to 40% of a full vehicle. Therefore, the lightweight body structure plays a rather important part in obtaining a satisfactory weight reduction of a full vehicle. There reduction of weight of the frame structure can be achieved by replacing the existing material with new types of light materials such as aluminum alloys, magnesium alloys, engineering plastics and composite materials. The second approach is to optimize the

number of parts of the body structure. By decreasing thickness and removing material in the components weight reduced in the structure.

Axial collapse modes of thin-walled box columns are one of the most effective methods to increase the crashworthiness of a vehicle. An idealized closed tube mounted for axial collapse is illustrated in Figure 1-2. Thin wall closed structures absorbs the kinetic energy involved in the system, which will protect passengers directly exposing to these high-speed impacts. An automobile frontal longitudinal rail is a typical example of the energy absorber columns in crash energy management, since the frontal crash safety performance of a vehicle is increased by the collapse behavior of these components. The frontal area of the rail structure is generally straight to induce axial progressive collapse, which is the most efficient mode of collapse for crash energy absorption. The crashing behavior of the front-end structure is very important because it affects the overall acceleration measured at the driver compartment during impact [4].

**Figure 1-2 Axial collapse mode for closed section tube [5]**

The bending collapse mode of a frontal longitudinal rail involves formation of local hinge mechanisms and linkage-type kinematics. The bending mode collapse in

frontal longitudinal rails can be either due to a bend in the profile of a frontal longitudinal rail or in offset collision of vehicle, there will be improper distribution of the load that will create a bending mode collapse in a straight longitudinal rail. Thus, even though the frontal longitudinal rail structure absorbs more energy due to axial collapse, it fails mainly due to the bending load acting on it. Figure 1-3 shows typical bending mode collapse of a frontal longitudinal rail.

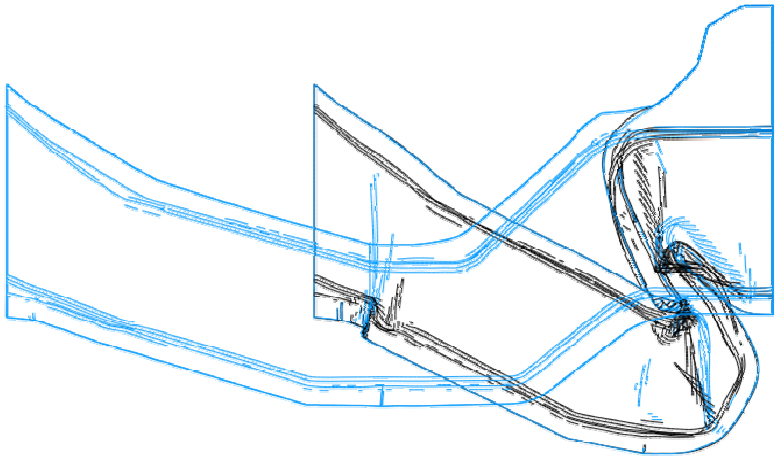

**Figure 1-3 Bending collapse mode of a closed section tube**

Thin-walled elements are the most commonly used to support the components on vehicle frame structure. The shape of the thin-walled profile and the technology of its manufacture are the main factors, which determine impact energy absorption by the car's frame. One such manufacturing technology consists of joining (resistance spot welding), two open omega-shaped profiles made of steel characterized by very high strength and plasticity (e.g. DOCOL 800DP) to form one closed profile. Such beams are mounted in the car's front section to absorb impact energy in the case of an accident. Most of

literature on thin-walled structures involves information about strength calculations of thin-walled profiles with a circular, rectangular, polygonal, solid (filled with foam) or hollow cross section, joined together by continuous bonding or welding, but there is little information about such calculations for thin-walled structures joined together by spot welding. The reported results of strength tests carried out on single spot welds are insufficient to predict the behavior of the thin-walled structure under axial compression. Taking into account the phenomena that occur when and after a thin-walled structure loses stability, the structure geometry, the kind of material used and the non-linearity due to geometrical, the designers has to precisely design and specify the calculation and methodology to determine strength for these types of thin walled structures. Since no information on thin-walled profiles joined by spot welding, subjected to axial-symmetric compression can be found in the literature, FEM-based simulations of structure crushing can be studied [5].

Automotive design companies using commercially available finite element software to simulate the crash analysis have urged developers to introduce more complex spot weld options in their packages which improve simplicity, efficiency and accuracy. MSC/NASTRAN is a widely used finite element software used in the automotive industry. MSC/NASTRAN has delayed to develop a separate tool in its menu to model spot welds for crash analysis. This is mainly due to the technical difficulties and other simple options exist, such as flexible springs and bars (CBUSH, CBAR), rigid elements (RBAR, RBE2, RBE3) and multipoint constraint that represent the spot weld in a full FEA model of vehicle. However, in recent years with the availability of high-

performance computing systems, designers and analysts are capable of running efficiently very large and detailed models with the goal of increased accuracy and correlation and validation with real physical experiments. This desire for improved accuracy and the need for modeling details of thousands of spot-welds has demanded tools for simplicity of modeling, and greatly improved accuracy of spot-welds for crash analysis [6].

As mentioned above, there are different options available in commercial FEA software to create spot weld connections in a simple manner, which does not require detailed information of the spot weld. The main reason for modeling a spot weld in a simple manner is to reduce the computational time. In case of a real structure the number of spot welds is very high. Hence, detailed modeling of each spot weld in huge structures will increase the computational and modeling time largely. For example, in a full vehicle there are about three to five thousand spot welds. The only practical approach is to model the spot welds with very coarse mesh that take care to verify that the model used accurately represents the stiffness characteristics of the real welds [6].

The spot weld plays an important role in crash simulation of a vehicle. The National Crash Analysis Center (NCAC) has been involved in crash simulation analysis for many years. Entire FEA models of the vehicle are created, and during development, intermediate validation for the performance and accuracy of the body structure is evaluated. NCAC has shown that there is a significant difference between simulation and test results in the case that only three spot welds at key locations in the entire car body is missing [7].

In [8], three different types of spot weld modeling techniques are described; a single element connection, a single hexahedron element connection, and a four hexahedron element connection, all available for crashworthiness application. Obviously, using a single beam element connection is the simplest discretization effort to model spot welds in a finite element model. In case of single element, the overall stiffness depends strongly on the position where the beam nodes are connected to shell surfaces. Secondly, the torsion stiffness of the beam cannot be activated since the corresponding degree of freedom is not available in the attached shell formulation. Considering the spot weld discretization with four hexahedron elements, the small element size would decrease the time step severely to maintain numerical stability in explicit solvers and hence additional mass scaling is required to allow larger time-steps but with loss in accuracy. The third modeling technique consists of one single hexahedron spot-weld element created between the joined components.

Failure properties of spot welds must be obtained by conducting physical tests that isolate pure load paths. Examples of these simple tests are the shear-tension, lap-shear, and coach-peel coupon tests. To conduct these tests a single spot-weld between the two thin plates. The shear-tension sample is tested in two different angles: load applied at $0^{\circ}$ creates a pure shear test, at $90^{\circ}$ creates a pure tension test on the spot weld [10].

As discussed earlier, an important feature in crash simulation is the amount of detail included in modeling spot weld connections. Traditionally for efficiency, simple node-to-node rigid connections for modeling spot weld connections between different

components are used, especially when many components are connected in a full vehicle crash model. Recent studies have shown the importance of accurate modeling including elastic stiffness and failure modes for spot welds in automotive crash analysis. For efficiency and convenience, many commercially available FEA packages now include the option of creating mesh independent spot welds, which allow the user to define the location of the center point of the spot weld and define the spot weld radius on adjacent surfaces of connected components. A distributed coupling to nodes within the radius specified is automatically created which approximates the behavior of a rigid spot weld of finite size. In addition, the size of the rigid spot weld model provides greater accuracy compared to the simple node-to-node connection. However, it has not been until very recent that some researchers and commercially available FEA software have the ability to include important spot weld elastic properties and failure modes combining pull, peal, shear, and torsion.

In this work, different levels complexity in spot weld modeling are examined in terms of sufficient accuracy which can be used efficiently for impact analysis of large connected components and full vehicle crash models. In order of increasing complexity, the following spot weld models are considered and results compared: (a) simple node-to-node rigid connection, (b) rigid mesh independent spot welds, (c) elastic mesh independent spot welds, and (d) elastic with failure mesh independent spot welds. In order to study the fundamental behavior of the different mesh-independent spot weld models, pull-out and peal tests between two thin ductile steel plates are performed which isolate different failure modes. Comparisons of reaction force versus displacement

curves and internal energy versus displacement for the different types of spot weld models are given. Results indicate that the rigid connected results in a reaction force which is much larger than elastic spot welds. The spot weld model, which includes failure, follows the same path as the elastic weld but when reaching the particular failure force the reaction remains constant with additional applied displacement.

To better understand the behavior of the spot-weld models for crash analysis on a realistic and important automotive component which exhibits complex crushing modes with combined axial and bending a frontal longitudinal rail designed for strength and energy absorption was studied with a node-to-node rigid spot weld compared with mesh independent rigid and elastic spot weld connections. In addition to spot welds, the effect of various shape and size parameter changes best suited for removal of kinetic energy for the rail component is studied.

# CHAPTER TWO

# MANUFACTURING PROCESS FOR AUTOMOTIVE STRUCTURES WITH SPOT WELDS

This chapter gives an overview of the manufacturing of thin-walled automotive structures jointed by spot welds. Stamping is the main process used to create the thin-wall automotive structures. Most passenger vehicles manufactured have a body that comprises 100–150 stamped metal parts. A stamped component in vehicle varies in size from a small like a bracket to a more complex panel such as fenders, hoods, and body sides [12]. These thin walled structures are joined to each other using spot welding process. Resistance spot welding (RSW) has been widely employed in sheet metal fabrication for several decades. The automotive industry prefers spot welding because it is can be an easily manufactured and cost-effective joining method. There are thousands of spot in every passenger vehicle. However, each spot weld in the body-in-white structure of a vehicle has different loads acting on it based on location.

The automotive front side rail is one of the most important parts in an automotive body in white, because of its energy absorption capacity during the frontal crash of a vehicle. In the past two decades extensive studies on front rails aiming to obtaining crashworthiness along with less weight have been performed. The frontal longitudinal rail is a closed thin walled structure manufactured in a stamping process with spot weld provided on both side flanges.

## 2.1 General Description on Stamping Process for Thin Walled section

Stamping is a metal working process by which sheet metal is punched using a press tool to form the sheet into a desired shape. This could be a single stage operation, where every stroke of the press produces the desired form on the sheet metal part, or a multi stage operation [11]. Generally, the body-in-white structures are sheet metal components with a thickness varying between 1.5 to 3 mm. In the stamping process, stretching of sheet metal takes place in between the dies to obtain the desired shape. Therefore, with a stamping process more intricate shapes with bend, beads and holes on sheet metal can be obtained. The alternative forming technique of forging where the metal is compressed in between dies, it is difficult to form a shape of sheet metal that has small thickness.

## 2.2 Spot Weld Manufacturing Process

Welding is the joining of two or more pieces of metal by the application of heat and sometimes pressure. In resistance spot welding, heat is generated by the resistance of the parts to the flow of an electric current at a localized area and a bond is created between the two thin sheets. The main difference between resistance welding process and other welding is that there is no need for filler metal or fluxes. In addition, the spot welding is a process in which weld is created by fusion so there no need for the application of force to forge the heated work pieces together. Figure 2-2 shows the welding of body-in-white structure in a vehicle assembly plant [11]. The projection

welding and seam welding methods also fall under the category of a resistance welding process. Spot welding is a type of resistance welding and most of the automotive body frame structures and components joined using spot welds. Spot-weld joints created by applying heat and pressure at a local area of the metals. The metal objects have provides a resistance to the current flow that make it possible for welding plates with less thickness. Compare to other process spot welding automation with robotic techniques is highly adaptable. A typical body in white contains thousand of spot weld that allows the automotive manufactures to use robotic techniques to create spot welds. With the application of robotic techniques, even the intricate locations of the components can be spot-welded. The application of robotic technique to create spot weld has allowed efficient creation of thousands of spot welds in single vehicle.

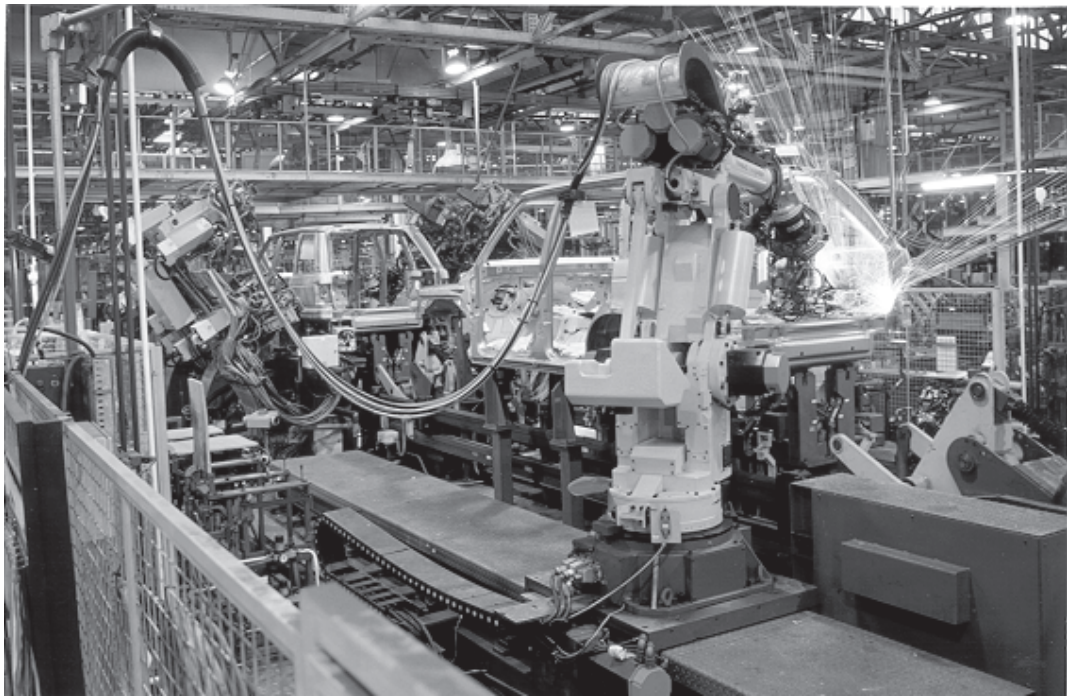

**Figure 2-2 Automated process of spot welding for Body-In-White structure [11]**

The Figure 2-3 shows a spot welding manufacturing process set-up. The spot weld process has two copper alloy electrodes and the sheet metal placed in between the electrode tip. A very high current supplied between the electrodes. The heat generated within the material by the resistance to the passage of a high current through the metal parts. Heat develops mainly at the contact area between two sheets, eventually causing the material at that location to melt, forming a molten pool and then solidify into a weld nugget. The Figure 2-4 shows the molten pool created due to the very current passed in between the electrode tip and the surrounding solid metal creates.

Spot welding is a technique generally used to bond metals shaped into sheets no thicker than 6.5 mm. Unlike other welding techniques, spot welding can create precise bonds without generating excessive heating that can affect the properties of the rest of the metal sheet. An important characteristic of the spot welding process is the time taken to create a weld. The time taken for production of a weld can be less than one second, depending on the application and the metal properties. The load carrying capacity of a spot weld mainly depends upon the quality of the spot weld manufactured. The amount of current follow between the plates through electrodes calculated based on the thickness of the sheet welded and the diameter of the spot weld. Spot welding is a widely employed technique to join sheet steels structure in the automotive industry.

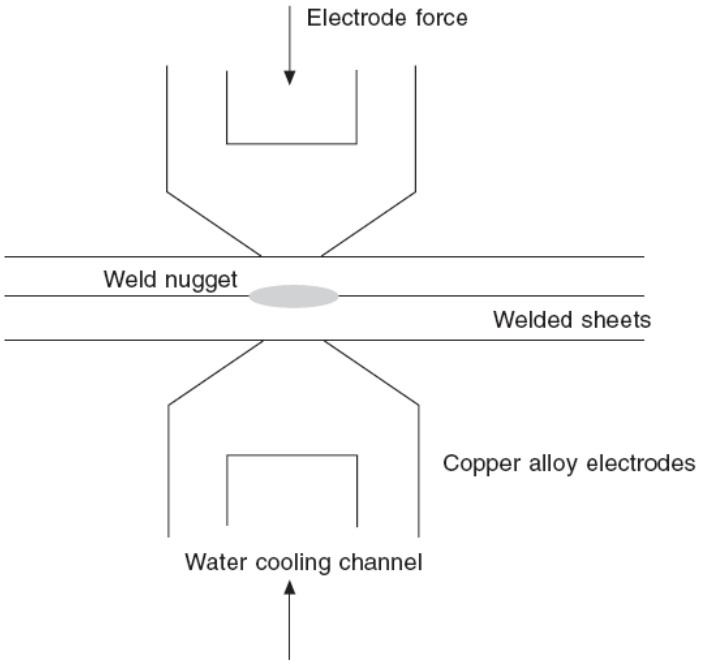


**Figure 2-3 Spot-weld manufacturing process [11]**

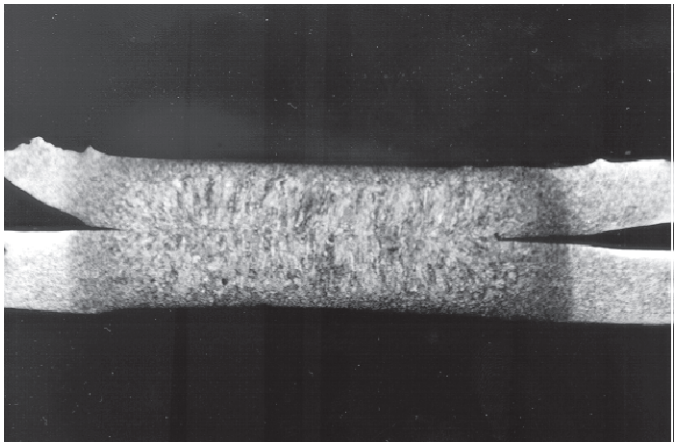

**Figure 2-4 Microscope view of a spot wed between two sheet metal parts [11]**

## 2.3 Material Model

For this study, ductile steel material is assumed for the sheets to be stamped and spot-welded to form components. Table 2-1 provides the mechanical properties of the material. The body-in-white of a vehicle is manufactured using steel even though there has been continuous study to replace it with a lightweight material like aluminum. Since the frontal longitudinal rail is studied the material properties of mild steel is considered.

| **Property** | **Metric** |
|---|---|
| Density (g/cc) | 7.89 |
| Tensile Strength, Ultimate | 693 MPa |
| Tensile Strength, Yield | 400 MPa |
| Modulus of Elasticity | 210 GPa |
| Poisson's ratio | 0.3 |

**Table 2-1: Material Properties for Steel used in this study**

# CHAPTER THREE

# SPOT WELD CONNECTION FOR CRASH ANALYSIS

In this Chapter, the various methods of spot-weld connection available for finite element crash analysis and the ways to create these options are discussed. A main goal of the investigation is to understand the performance of the different kinds of spot weld options available for crash analysis. Spot-welds plays an important role in keeping the automotive components joined with each other. In the case of studying the crash behavior of the entire vehicle, using a finite element analysis, important details about the spot weld behavior has to be provided so that the final simulation results match experimental values. The failure of a spot weld occurs due to different kinds of load acting on it. Failure can be either due to shear load, twisting load or bending load. However, most of the finite element codes until recently have used a simple node-to-node rigid connection to represent spot welds in the model. This kind of assumption leads to (1) under estimation of energy absorbed in crash analysis, (2) cannot predict the failure of the spot weld, (3) the shell elements around the connection can be unrealistically distorted when compared to the elements some distance away from the node-to-node rigid connection. Another approach for modeling spot welds is using the solid elements. This level of detail is an excessively expensive process because there are usually several thousands of spot welds in a car so it takes more time in modeling and solving. To achieve realistic finite element simulations of crash of auto-body structures, the connection between the components in the FEA models needed to be specified properly in terms of their respective materials and failure [7].

## 3.1 Various Options for Spot weld Connection for Crash Analysis

In this Section, the Mesh Independent spot weld feature which is available in ABAQUS is compared with the other kinds of spot weld connections. For this study six different spot weld models which are available in ABAQUS are consider that can be used in crash analysis application. First is the single node-to-node rigid Multi-Point Connection (MPC) between the top and bottom surface node as shown in a Figure 3-1(a). Next is to connect a set of nodes in the top and bottom surface rigidly to a reference node and a rigid MPC connection created between these references nodes has shown in Figure 3-1(b). This kind of connection attempts to simulate a rigid spot weld of finite size. Third is a mesh independent spot weld connection, created using a connector element as shown in Figure 3-1(c). Using connector elements to create a spot weld option allows the user to model very complex behavior of the connector. Like other uses of connector elements, the connection can be fully rigid or may allow for unconstrained relative motion in local connector components. In addition, deformable behavior can be specified using a connector behavior definition that can include the effects of elasticity, damping, plasticity, damage, and friction. Therefore, the third type uses a connector element to create a spot weld that will have rigid behavior properties in it. The fourth type is to create a spot weld connection that will have the elasticity properties added to it. By adding elasticity to the spot weld. The behavior of deformation will be appropriately equivalent to the experimental component deformation. The fifth type of connection is to add a failure criterion of the spot weld. By this method, a particular load on the spot weld reaches the failure load; it will fail and will allow the sheets to separate at that location.

The failure of a spot weld can be a coupled or uncoupled based on the load acting on each direction of a local co-ordinate of the spot weld. In case of a spot weld involved in a crash analysis of a vehicle or component, the failure behavior is provided in a coupled manner.

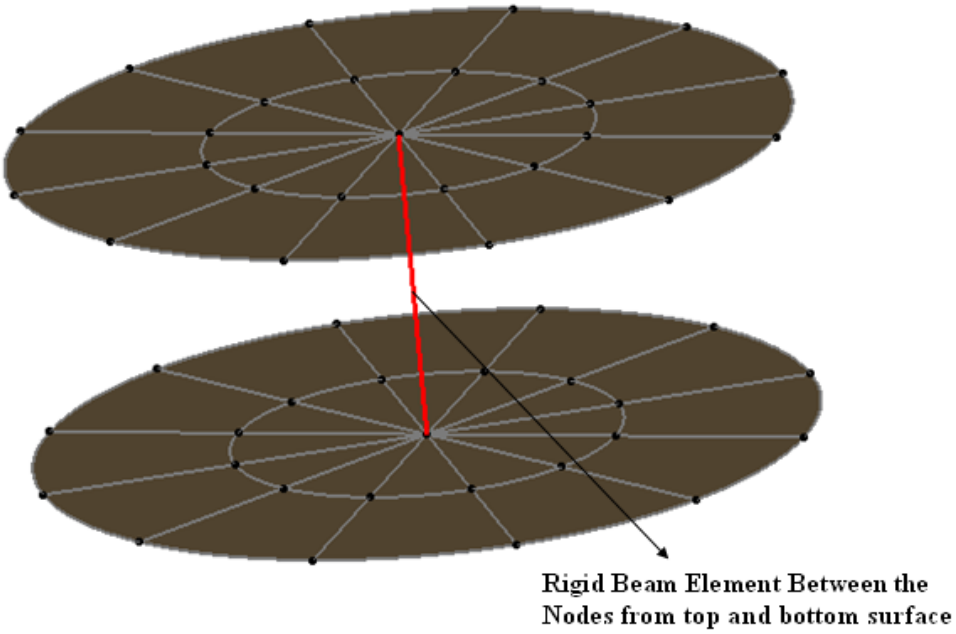


(a)

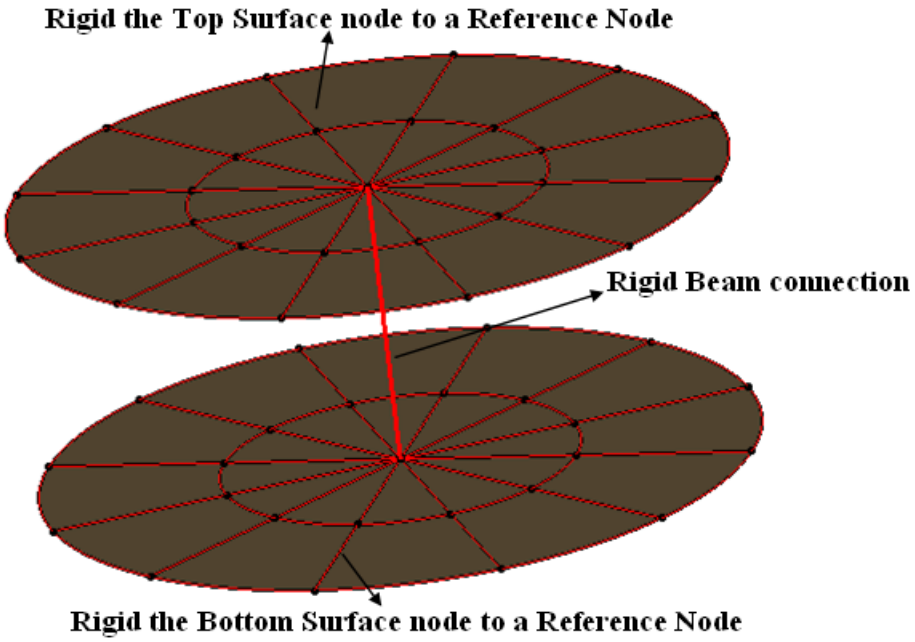


(b)

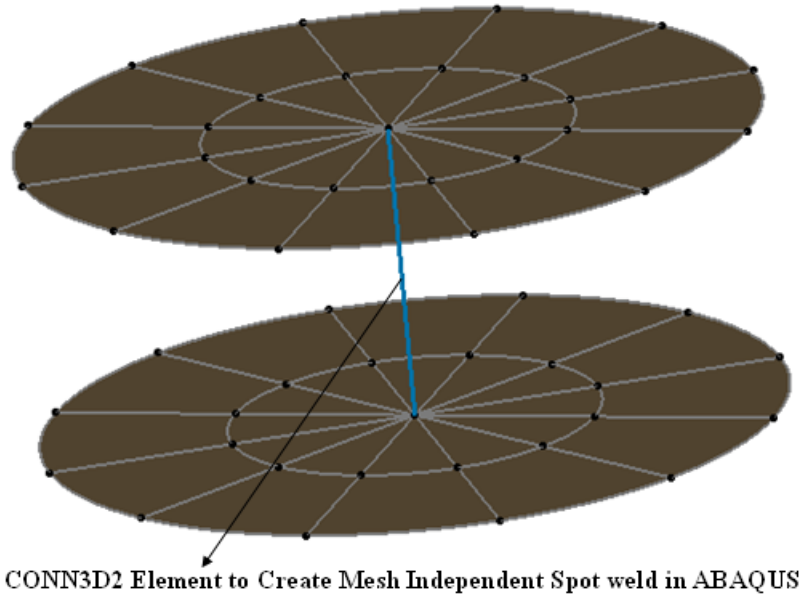


(c)

**Figure 3-1 (a) Simple node-to-node rigid spot weld connection, (b) Rigid spot weld created using rigid body and MPC, (c) Mesh independent spot weld**

## 3.2 Mesh Independent Spot Weld

There are thousands of spot weld in automotive assemblies. The manner in which spot welds undergo damage and failure during a crash can obviously influence a vehicle's structural crashworthiness. One of the most useful tools developed for crashworthiness simulation in ABAQUS is a mesh-independent fastener that can be used to simulate elastic, failure and damage behavior in spot welds. A spot weld connection used in crash simulation must behave like a point–to-point connection between two surfaces with good computationally efficiency and must be relatively easy to create. The mesh independent fastener option in ABAQUS v6.8 [16] automatically determines the locations of the spot weld based a reference node provided, and identify the two shell surfaces, which is connected by creating the distributed coupling. The mesh independent spot weld can also tie more than two shell surfaces. Either a connector element or BEAM MPCs between the two surfaces act has a local center axis for spot weld connection. Based on the spot weld radius provided, the number of nodes involved in the distributed coupling is automatically determined.

In case of mesh independent spot welds, the fastener can be defined without any relation to the nodes on the surfaces to be connected. For example, a mesh independent spot weld is created between two plates is shown in Figure 3-2. The number of nodes in the top and bottom plate involved in the spot weld is based on the radius of the spot weld specified. The location of the spot weld does not dependent upon the mesh of the plates. Even if the mesh on the plates is changed, the location of the spot weld remains

unaltered. The only difference will be the number of nodes involved in the spot weld distributed coupling would have increased has shown in Figure 3-2. The mesh-independent fastener capability in ABAQUS is designed to model the spot weld connections in a convenient manner; one that contributes to modeling efficiency and saves a great deal of time for engineers in creating the spot welds connections. Once the connection is created, the properties of the spot weld have to be provided to accurately model the complicated connection behavior of the spot-weld between two sheets.

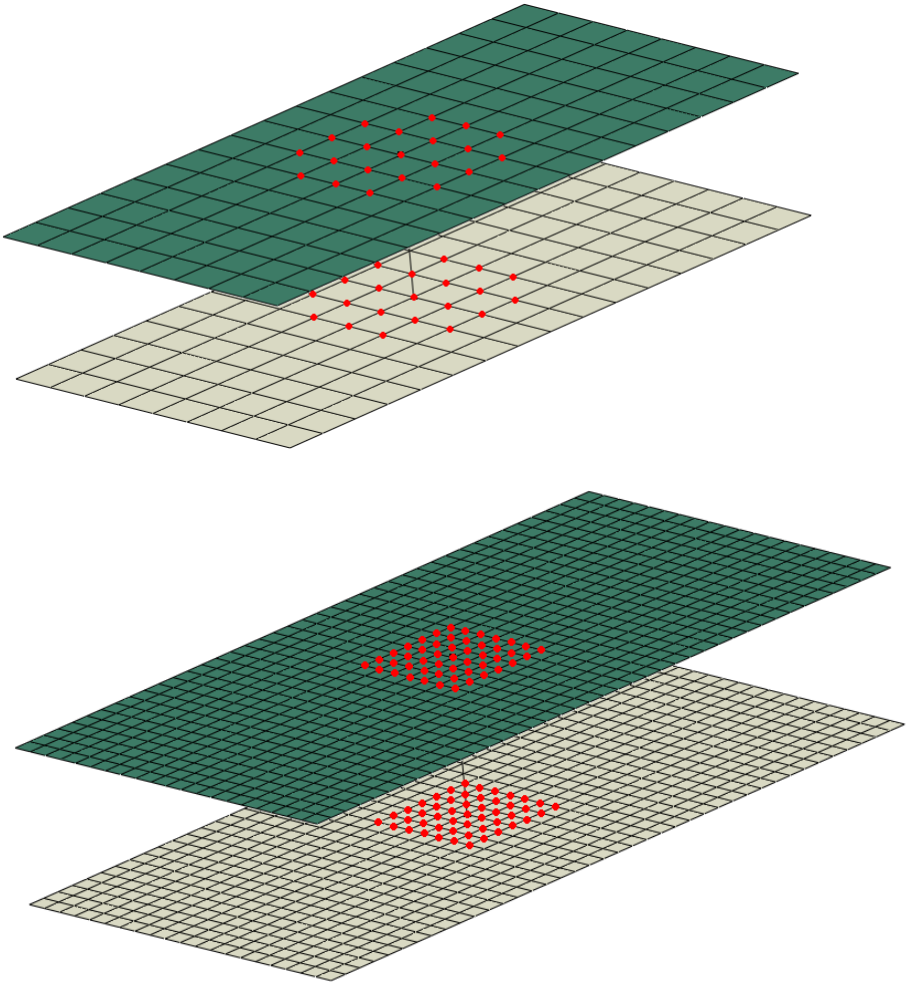

**Figure 3-2 Mesh independent spot-weld on coarse and fine mesh**

## 3.3 Mesh Independent Spot Weld Failure

Before explaining the different failures modes of a spot weld, the different load components and local coordinates of the spot weld are discussed. While modeling spot welds in ABAQUS, six loading components with respect to a global coordinate system are defined for the assembly. There are 3 force components, and 3 moment components (couples) as degree of freedom with respect to the global coordinate system. As shown in the Figure 3-4, the center of the spot weld is considered as the origin for the local coordinates system [16]. The local coordinates $x_1$ and $y_1$ are directed in the plane of the mid surface of the spot weld, and parallel to the surface of the spot weld, respectively. The axis that is perpendicular to the surface of the spot weld is considered as the local coordinate $z_1$.

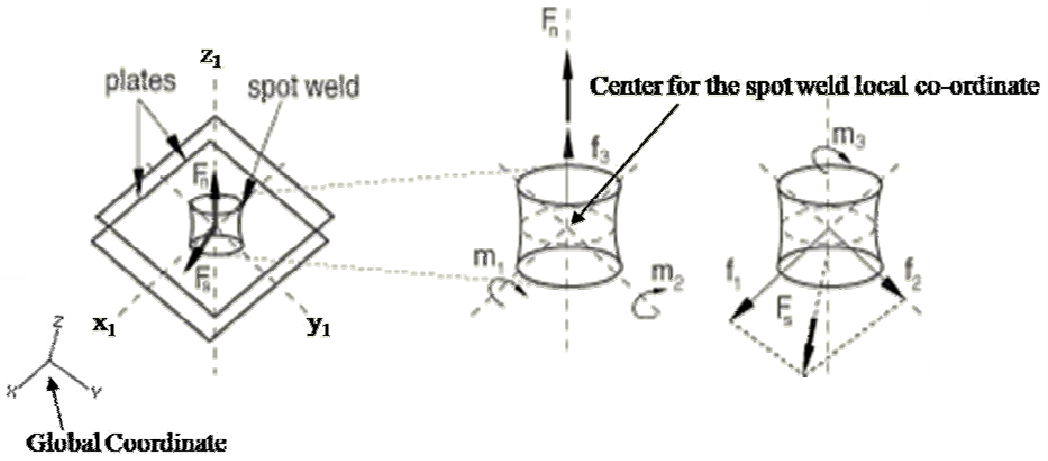


**Figure 3-3 Loading components of the Spot weld in local co-ordinate [16]**

The local in plane force components $f_y$ and $f_z$ are combined into one resultant shear force $F_s$, and the force along the out of plane axis is considered has the normal force

$F_n$. The local moment components, $m_1$ & $m_2$ are combined into one local resultant bending $M_b$ and the moment $m_3$ is considered as a twisting moment $M_t$.

There are four different types of failure modes in the spot weld. The sliding mode failure of the spot weld is due to in plane forces that act along the local axis of the spot weld. The shear failure of a spot-weld studied, creating a spot weld at the center of plates and applying a pure shear load. Tear mode failure is due to the out of plane moment $m_3$. This is due to the twisting moment acting on the spot weld connection. The other two failure modes of the spot weld are due to pulling the spot weld in the out of plane direction. This open mode failure may be evenly deformed or unevenly deformed based on the kind of force acting. In case of normal force $F_z$ failure can be studied by conducting a pull test. The uneven deformation of open mode failure is when the spot weld opens up in one side and leaves the other side unaffected. This kind of imbalanced opening of the spot weld can be studied by conducting a Peel test [1].

The above explanation described the different kinds of individual failure modes in a spot weld. However, for general loadings on structural components with spot welds, the failure modes are coupled. In ABAQUS, the failure criterion combining multiple failure modes is written into a single equation as follows: Equation (1)

$$\left(\frac{f_s}{F_s}\right)^{\alpha} + \left(\frac{m_b}{M_b}\right)^{\gamma} + \left(\frac{f_n}{F_n}\right)^{\mu} + \left(\frac{m_t}{M_t}\right)^{\beta} = 1$$

In this equation s, b, n and t represent the four independent failure modes- tensile shear, peel bending, normal pull and in-plane torsion. The denomination $F_s$, $M_b$, $F_n$ and $M_t$ represent the spot weld strengths of the four independent failure modes, and the

numerators $f_s$, $m_b$, $f_n$ and $m_t$ represent the applied loads on the corresponding failure modes. The symbols α, γ, μ and β are the unknowns that would define the failure surface between the independent modes, and must be determined by experiment [17]. This is known as a coupled failure spot weld model. Regardless of the values of α, γ, μ and β any single loading can be studied until the failure equation would be satisfied when the value of the numerator is equal to the denominator. This means that when the applied load reaches the failure load of a spot weld, the spot weld will fail for each single failure mode. This is known has uncoupled failure of a spot weld. In ABAQUS, damage models which can account for strain rate, and brittle fracture can be included as options in a generalized failure model, but are not used in this study.

For the elastic spot-weld model, a stiffness value, which depends on the plate thickness, is defined for each of the deformation modes of shear, peal, normal, and rotation. The elastic spot weld stiffness values used in this study are obtained from an empirical formula found in [16] and shown below:

$$K = C \times t_1^{n_1} \times t_2^{n_2}$$

Here, K is the stiffness of the spot weld, $t_1$ is the smaller plate thickness and $t_2$ is the larger plate thickness. A different stiffness value is determined for each deformation mode. The stiffness value depends on the thickness and material properties of the sheets [16]. Failure of a spot weld can be considered equivalent to the combination of local forces and/or moments in the different modes exceeding a maximum limit, and then setting the stiffness values to zero, so that the weld cannot carry any further load.

| Failure Mode | Thickness mm | C | $n_1$ | $n_2$ | K N/mm |
|---|---|---|---|---|---|
| Shear | 1.55/2.16 | 10307 | .2 | 0.2 | 13118.35 |
| Peel | 1.4/1.0 | 1.761 E5 | 1.667 | 0.667 | 2.2E05 |
| Normal | 1.38/1.2 | 652 | 1.3 | 0.9 | 1106.45 |
| Rotation | 0.99/0.68 | 2.0E6 | 0.55 | 0.33 | 1.6E6 |

**Table 3-1: Elastic properties for Spot Weld**

## 3.4 Rigid Body and Beam MPC Spot Weld

A rigid spot weld is created using rigid body option and Multi-point constraint. In a rigid spot-weld, a set of nodes in the top surface and bottom surface connected to a reference node has a rigid body and a MPC rigid beam created between the two reference nodes. Rigid body is a collection of nodes, elements, or surfaces whose behavior is controlled by the motion of a single reference point called the rigid body reference node. The relative positions of the nodes and elements that are included into the rigid body moves based on the reference node. A rigid body created in ABAQUS V6.8 cannot be deformed but it can move based on the reference point boundary conditions. The motion of a rigid body is prescribed by applying boundary conditions at the rigid body reference node [16]. MPC provides a rigid connection between two nodes; it will also constrain the displacement and rotation degree of freedom at the first node to the displacement and rotation degree of freedom at the second node.

CHAPTER FOUR

# FINITE ELEMENT MODEL AND TESTING PROCEDURES FOR SPOT WELD

In this study, Finite Element Analysis (FEA) is used to study the behavior of various spot weld connections used in crash analysis. The analysis is performed for two loading conditions acting on the spot weld. Failure properties for spot welds are obtained by conducting shear, pull, peel and twist coupon tests. This chapter deals with the geometric modeling, finite element meshing, loading and boundary conditions for non-linear analysis of spot weld for the pull and peel tests.

## 4.1 Spot Weld Test Procedure

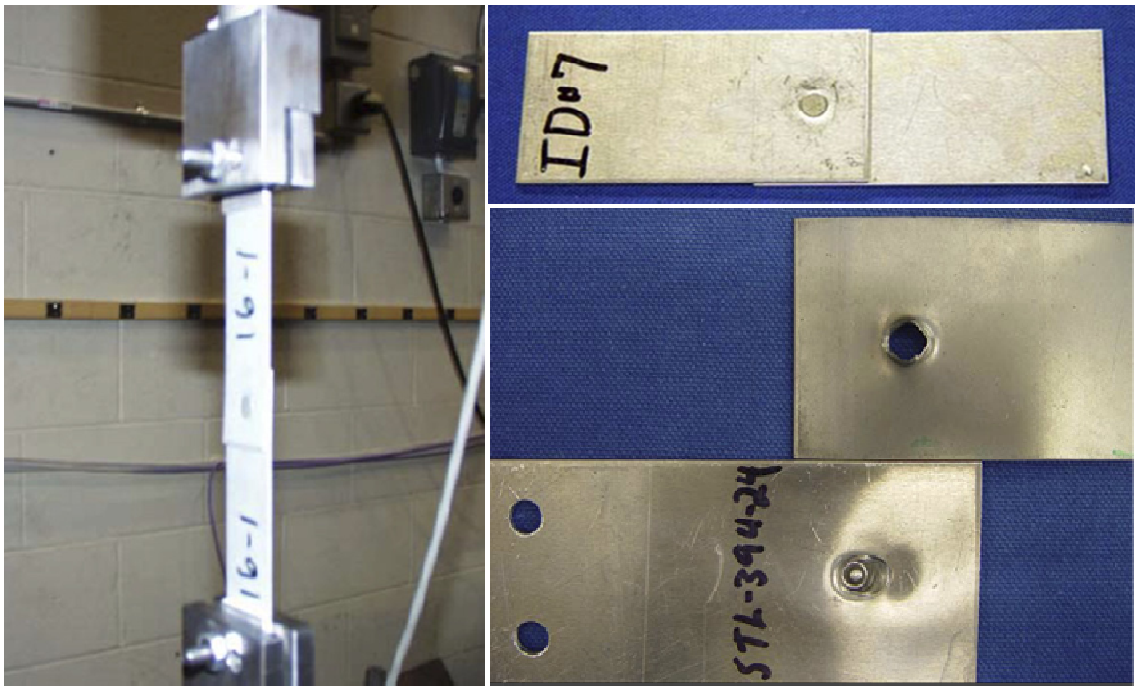


**Figure 4-1 Shear test step-up showing specimen with a spot weld and spot weld failure [14].**

Figure 4-1 shows the shear test perfomed on two sheets connected with a single spot weld. This test coupon has a two thin plates with half the length placed over each other and a spot weld is created at the center of the over lap area [14].

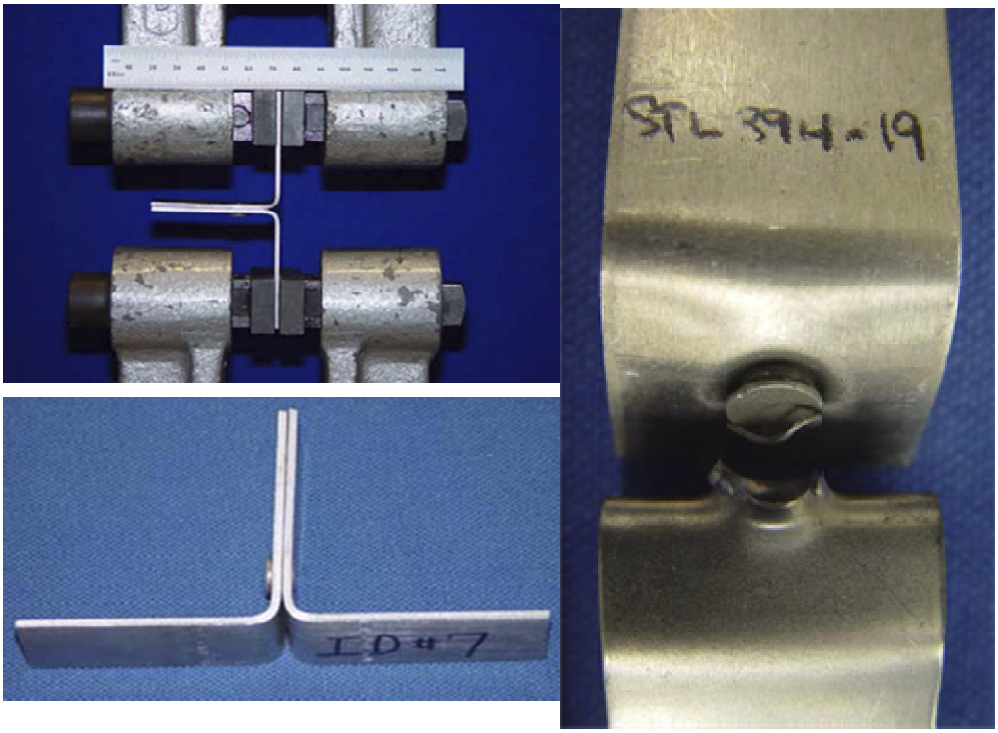

**Figure 4-2 Peel test step-up showing specimen with a spot weld and spot weld failure [14].**

Figure 4-2 shows the peel test for a spot weld specimen. For each kind of failure mode, there has been a separate test coupon and test procedure developed. This test coupon has a thin two plates with L-shape joined together. The top and bottom edges of the coupon is pulled evenly from both sides until failure occurs. The force at which the failure of the spot weld occurs ploted against the displacement.

Figure 4-3 shows the pull test for a spot weld. This test coupon has a two inverted cup shape plates and a spot weld is created in between the mating plates [14]. The two holes in the top and bottom of the cup shape plates are the mounting points on to the test fixture.

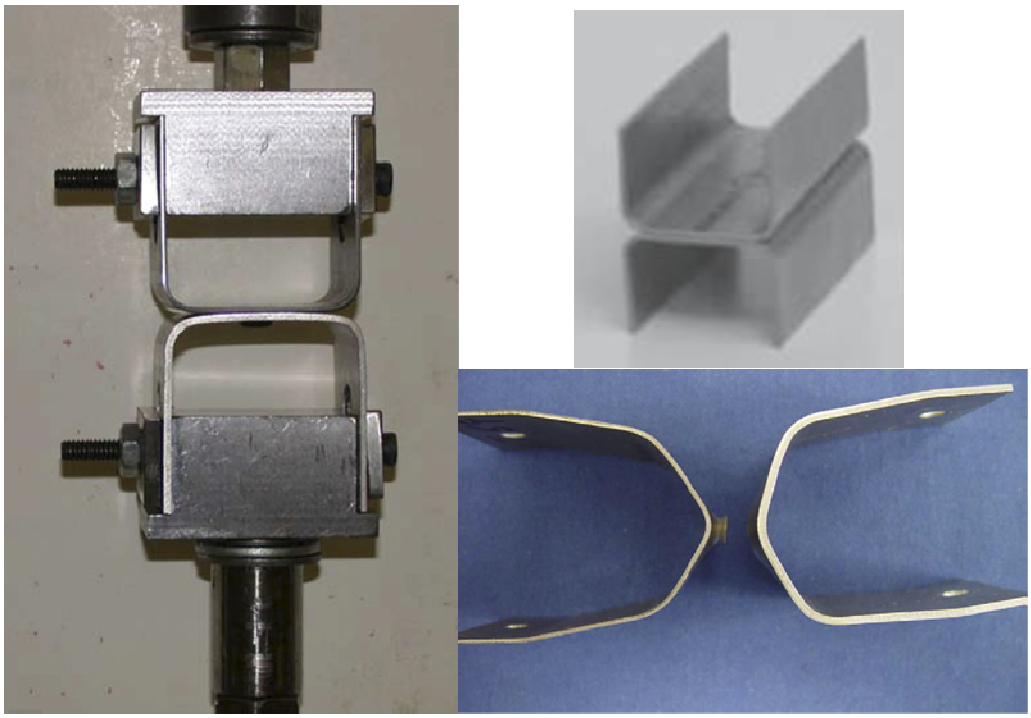

**Figure 4-3 Pull test step-up showing specimen with a spot weld and spot weld failure [14].**

4.2 Geometric modeling for the shell model of Pull and Peel Test Coupon

As mentioned previously, the (a) sliding mode failure, (b) tear mode failure, (c) even deformation due to pull mode, and (d) uneven deformation due to pull mode failure, are the four kinds of failure modes that are combined in a spot weld during crash. To compare the different kinds of spot weld models, pull and peel tests where modeled using

ABAQUS v6.8 finite element software. Separate specimen geometries for both pull and peel tests were created using CATIA V5 CAD software.

In case of the pull test, a cup-to-cup test coupon as shown in Figure 4-3 is used to determine the normal separation strength Fn and stiffness Kn of a spot weld along the out of plane axis. This is a newly designed specimen disclosed in [9], with two back-to-back cups welded at the center of the back surfaces. Each of the cups has a pair of short walls, which are butt welded to the long walls. The end of the long wall has a reinforced pinhole for loading. When loaded through the long wall pinholes, the unevenly distributed bending moment is relieved, and a nearly pure lifting force is applied evenly around the spot weld. Two different test results can be obtained by pull test coupon, the nugget shear-off or the nugget crack. The first failure is a typical nugget pullout is complete nugget shear-off around the heat affect zone. The second failure is a nugget crack is radial cracks occurred in the center area of the nugget. The load/deflection curve for this test is provided in [9], from which the normal pull strength, Fn and stiffness Kn of the spot weld is interpolated.

In case of the peel test, two L-shape plates are used to determine the peel strength $M_b$ and stiffness $K_b$. The L-shape coupon used was developed in [10], the local peel moments ml and m2 can be combined into one local resultant bending moment $M_b$.

Figure 4-4 shows the geometric CAD model of cup-to-cup test coupon used in the Pull Test, and Figure 4-5 shows a 2D drawing with all the dimensions of the plates. The CAD model is created in CATIA V5. A simple U-shape sketch is extruded along for a length of 19.5 mm. The bottom cup has the same dimensions. There is a thickness

difference between the top and bottom plates, the top plates as a thickness of 1.38 mm and the bottom plate as a thickness of 1.20 mm. The shell created represent the middle surface of the plates so the gap between the top and bottom cup is equal to summation of the half the thickness of top and bottom plates. The both plates are place at an offset distance of 1.29 mm. A fillet radius of 2.5 mm is provided to the sharp edges of the model.

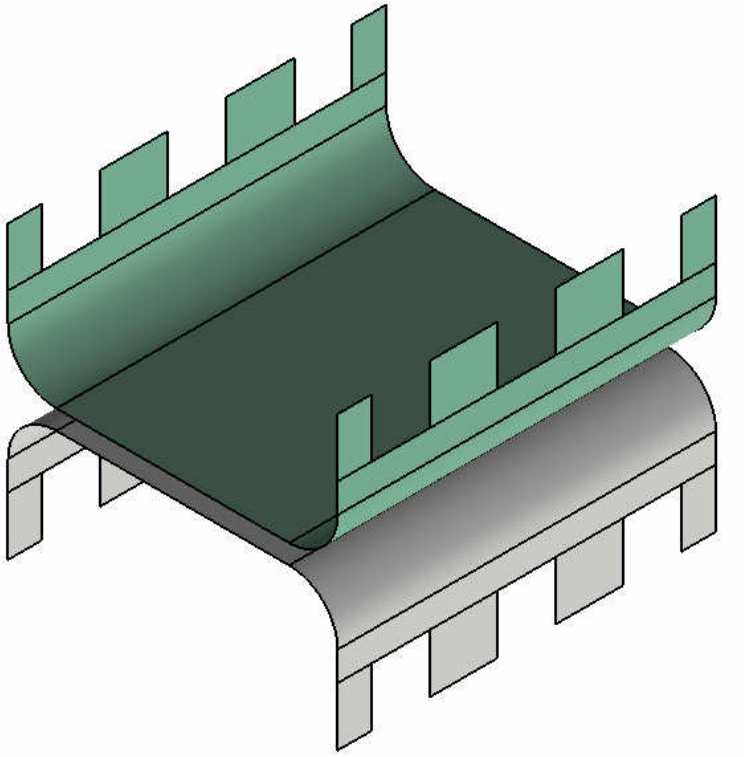

**Figure 4-4 Pull test CAD model created in CATIA V5**

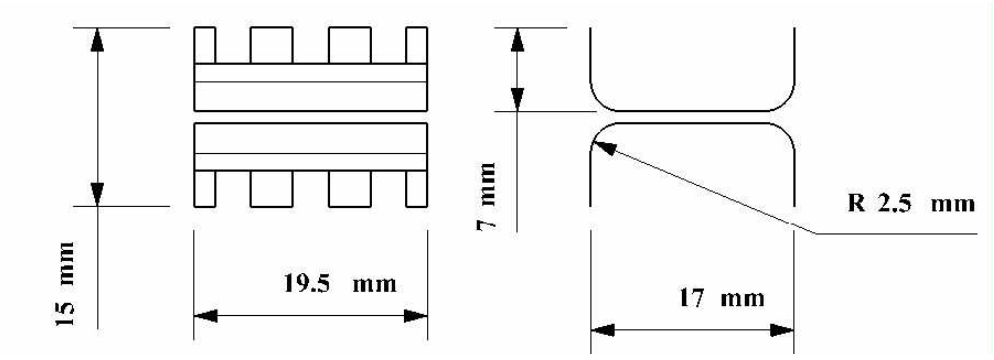


**Figure 4-5 Dimensions of the pull test specimen created in CATIA V5**

Figure 4-6 shows the CAD model of two L-shape test coupons used in the Peel Test) and Figure 4-7 shows a 2D drawing with all the dimensions of the plates. Using CATIA V5, an L-shape sketch is extruded to a length of 20 mm to create the top L-shape plate. The bottom L-shape plate has the same dimensions. There is a thickness difference between the top and bottom plates, the top plates as a thickness of 1.40 mm and the bottom plate as a thickness of 1.00 mm. The sheet created represents the middle surface of the plates so the gap between the top and bottom cup is equal to summation of the half the thickness of top and bottom plates. The both plates are place at an offset distance of 1.20 mm. A fillet radius of 4 mm is provided to the sharp edges of the model.

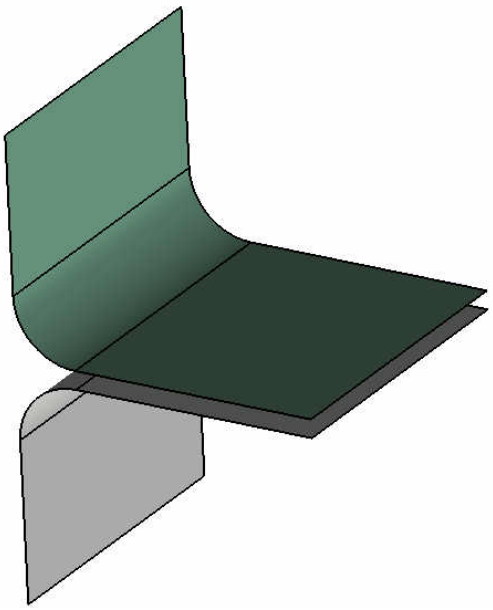

**Figure 4-6 Peel test CAD Model Created in CATIA**

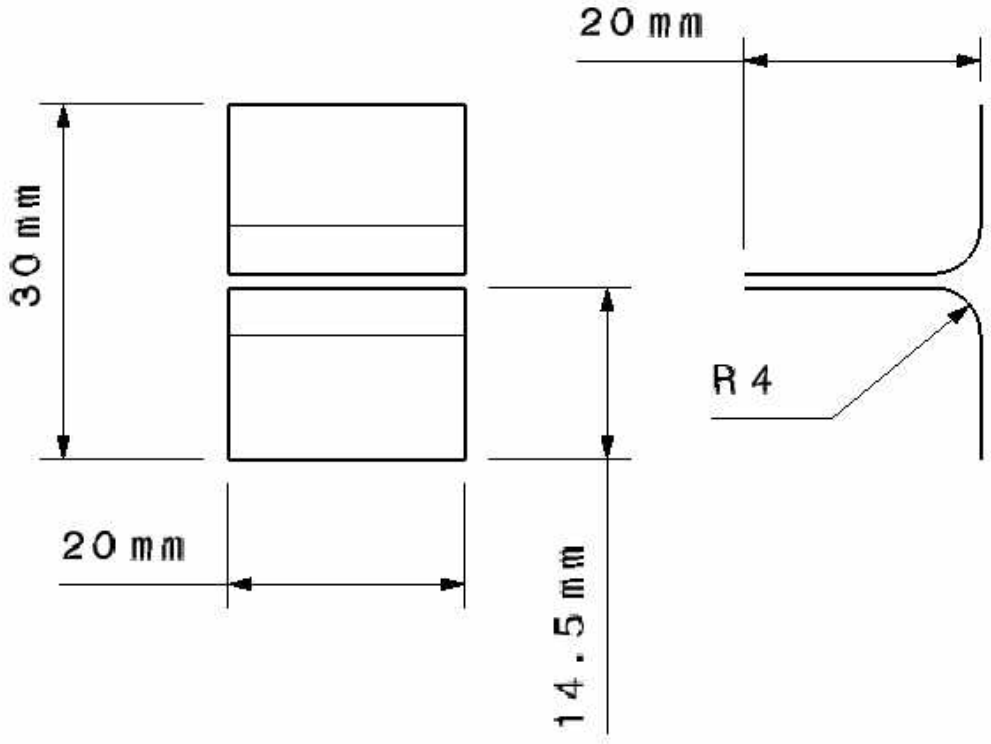


**Figure 4-7 Dimensions of the Peel Test Specimen**

## 4.3 Finite Element Mesh for the pull and peel test coupon

The surfaces of the geometric model are meshed using HYPERMESH with shell elements of 0.75 mm element size for the pull test and 1 mm element size for peel test. The CAD model created in CATIA V5 is imported into HYPERMESH in the IGES format. The surface is meshed with 4-node doubly curved thin or thick shell, reduced integration, hourglass control, finite member strain element (S4RS). The mesh from HYPERMESH is saved as an ABAQUS v6.8 input. A total of 1962 nodes and 1784 elements are present in the finite element mesh of the pull test geometric model and 1407 nodes and 1300 elements are present in the finite element mesh of the peel test geometric model. Figures 4-8 and 4-7 shows the mesh detail of both the pull and peel test specimens.

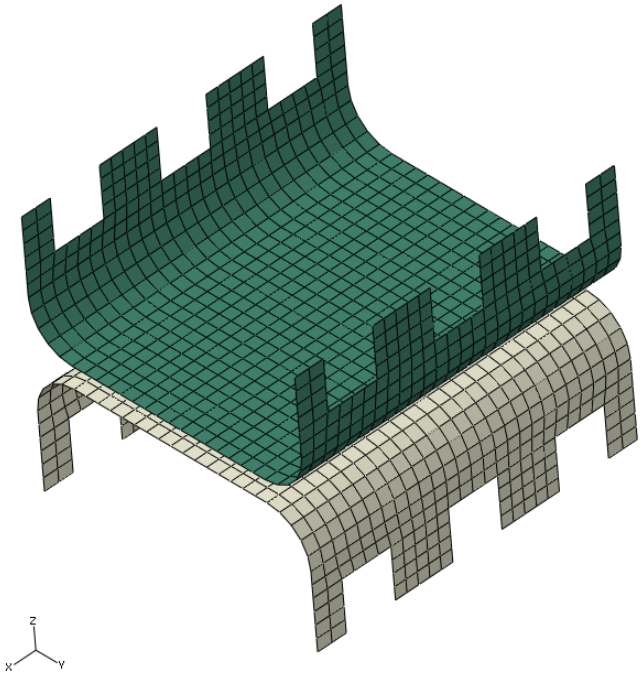


**Figure 4-8 Mesh for the pull test specimen**

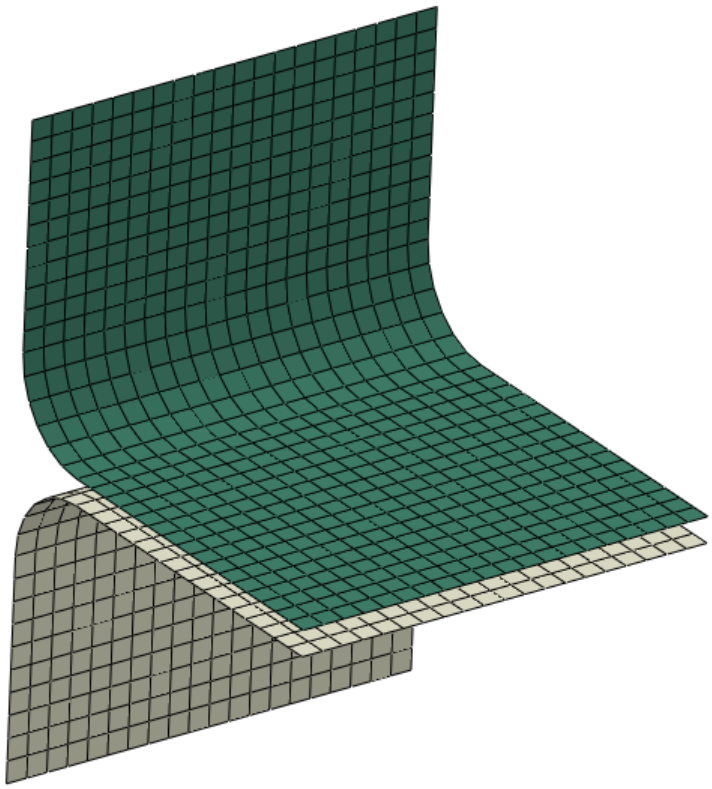

**Figure 4-9 Mesh for the peel test specimen**

## 4.4 Boundary conditions for the pull and peel test

Pull and peel-coupon tests are modeled with the different types of spot-weld connections discussed in Section 3-1. The loads and boundary conditions are different for both pull and peel test. In case of a cup-to-cup test coupon a displacement of 8 mm along the z-direction is applied to the both rigid body reference points. To obtain a proper lift of the cup, the walls on both sides of the plate shown in Figure 4-10 are rigid connected to a central reference point. Both the top and bottom cups have a central reference point to which loads are applied.

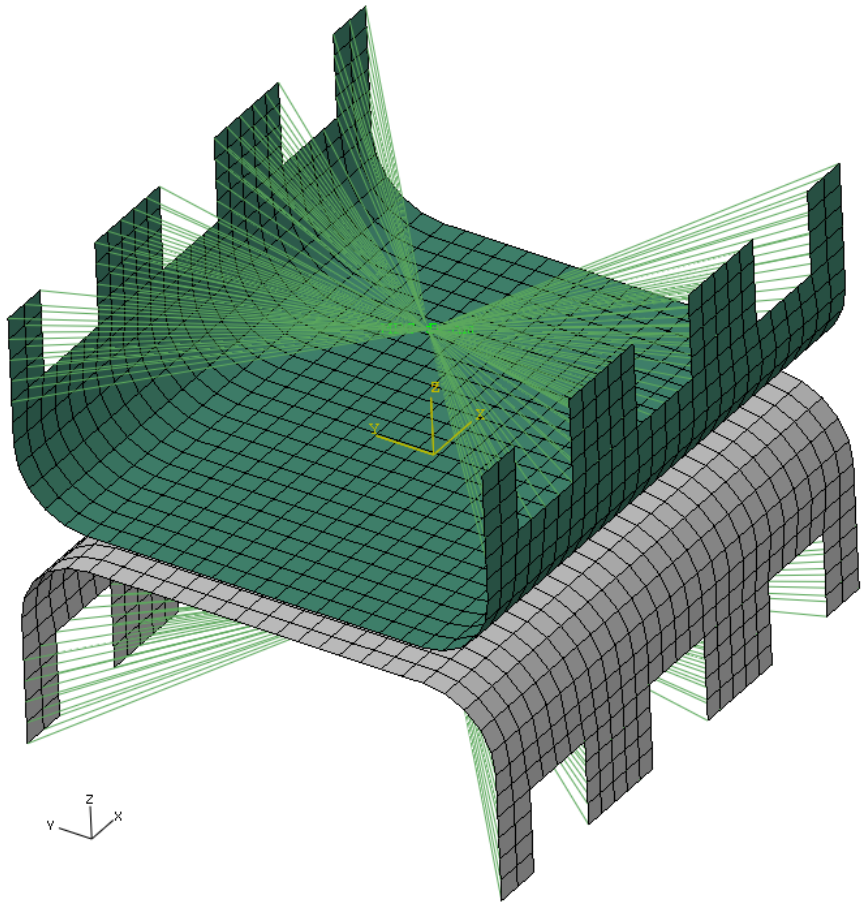

**Figure 4-10 Sidewalls of the cup shape plates are rigidly connected to a central reference point**

A displacement boundary condition is applied to the both center reference nodes. The top and bottom reference points are allowed to translate in z-direction alone with other degrees-of-freedom restricted. A displacement of 8mm is provided to the both top and bottom rigid body reference point in opposite directions. Figure 4-11 shows the boundary conditions applied for the pull test.

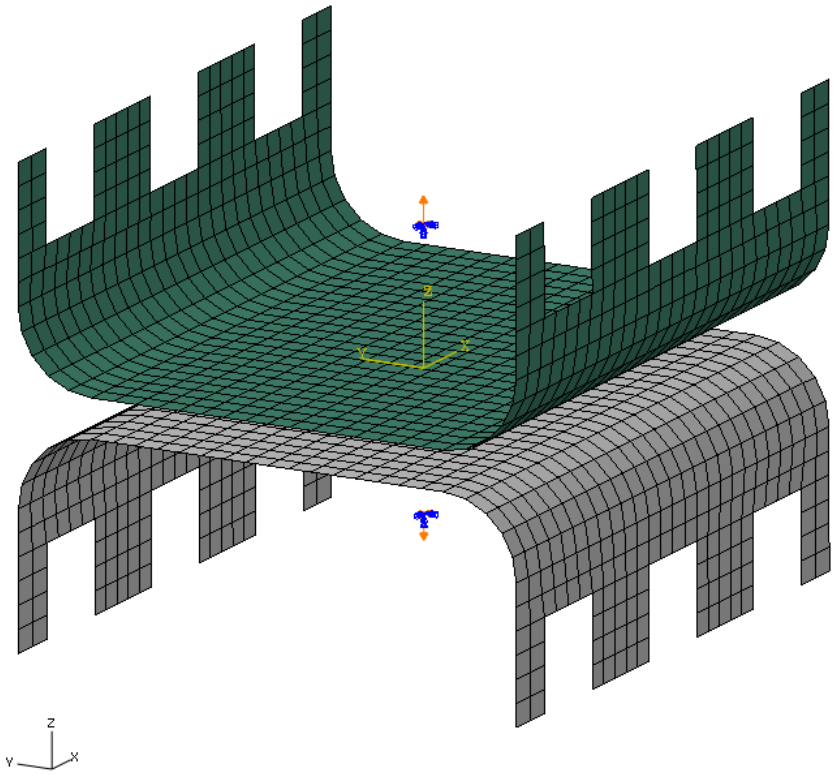


**Figure 4-11 Equal and opposite vertical displacements applied on the both top and bottom reference point**

In case of the peel test, the L-shape plates are used to create different types of spot-weld connection at the center and a peel displacement of 16 mm applied. To obtain a proper peel of the two plates, the both top and bottom vertical walls are connected rigidly to a central reference point. The Figure 4-12 shows the top and bottom reference points. The purpose of making the walls rigid to the reference point is to achieve a uniform behavior as per the boundary condition provided to the reference point. Both the top and bottom L-shape specimens have central reference points to which boundary conditions are applied.

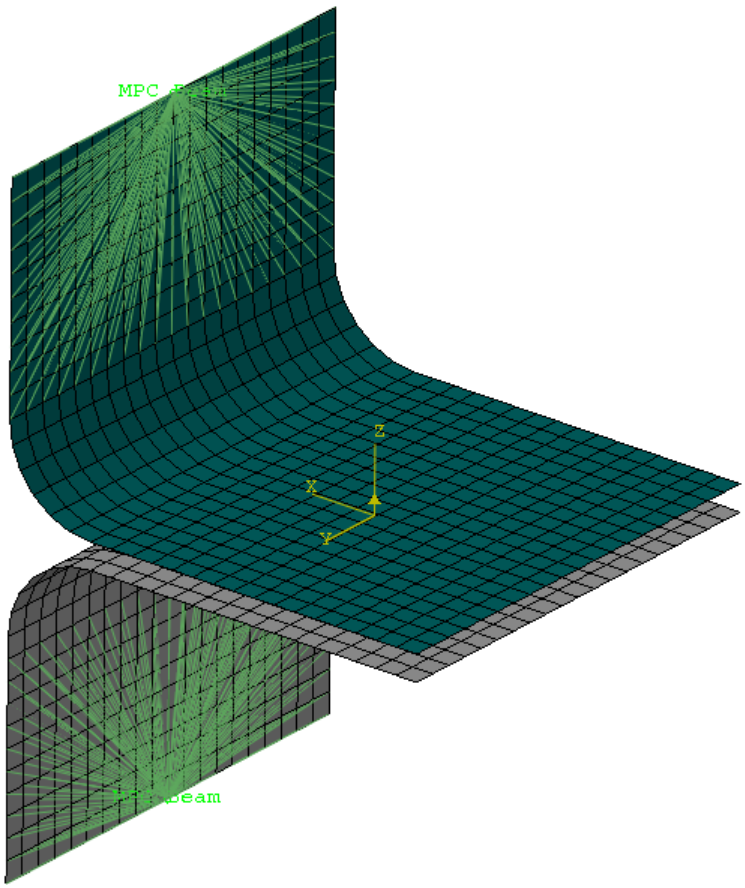


**Figure 4-12 Sidewalls of the plates rigidly connected to reference nodes.**

A displacement boundary condition is applied to both center reference nodes. The top and bottom reference points are allowed to translate in the z-direction alone with the other degree-of-freedom restricted. A displacement of 8mm is provided to both top and bottom rigid body reference point in opposite directions. Figure 4-12 shows the boundary conditions applied for both top and bottom plates of the peel test specimen. The edge nodes of the horizontal surfaces are fixed in all degree-of-freedom components as shown in Figure 4-13.

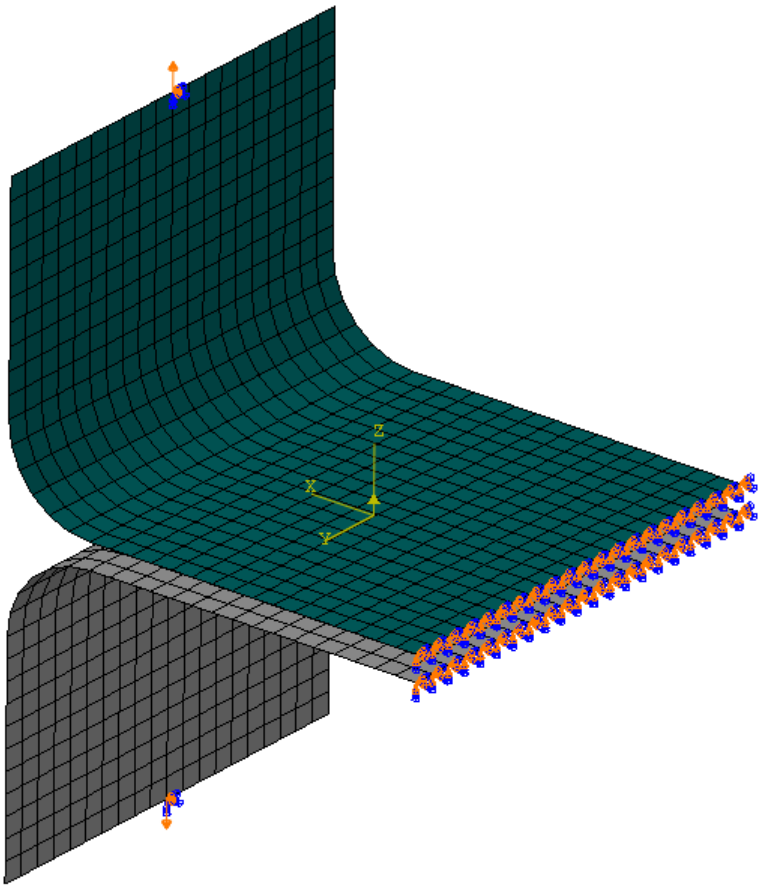


**Figure 4-13 Equal and opposite displacements applied on the both top and bottom reference points**

## 4.5 Dynamic Non Linear Analysis

The main goal of the investigation is to study how spot weld plays an important role in crash analysis. Since crash analyses are high-speed impact events, ABAQUS/Explicit is used to simulate the pull and peel test for different the different types of spot weld modeling techniques. Both the pull and peel test was conducted for a

duration 200 ms and the applied displacement  is applied has a smooth step over this time interval.

## 4.6 Results for Pull Test

In the previous sections the steps involved in creating different kinds of spot weld connection for the Pull test in ABAQUS v6.8 was discussed. The spot weld options that are Mesh Independent allows monitoring the output of the spot weld in the form on forces and moments in the local co-ordinate of the spot weld. In case of rigid spot-welds created using none-to-node BEAM MPC and rigid body connectors, only the internal energy of the test specimen is measured. Figure 4-14 shows a front view of the pull coupon for the comparision of deformation between the rigid spot weld created using Mesh Independent spot weld and spot welds created using rigid body connection and Beam MPC.  Deformation result that the rigidized spot weld with MPC is more stiff when compared to the “rigid” spot weld created using the Mesh independent spot weld. This difference occurs because in ABAQUS when a Mesh Independent spot weld is used to create the “rigid” spot weld between surfaces,  the software internally calculates and applies a  high value of elasticity to the spot weld to relax the perfectly rigid condition. When elastic data is not available for the spot weld, then it is better to use the rigid spot weld option available in mesh independent fasteners which can be used to monitor the spot weld local forces and moments. As shown in Figure 4-14, the bottom plates deforms more when compared to upper plates because of the difference between the plate

thickness. Since the lower plate has lesser thickness it deforms more compared to top plate.

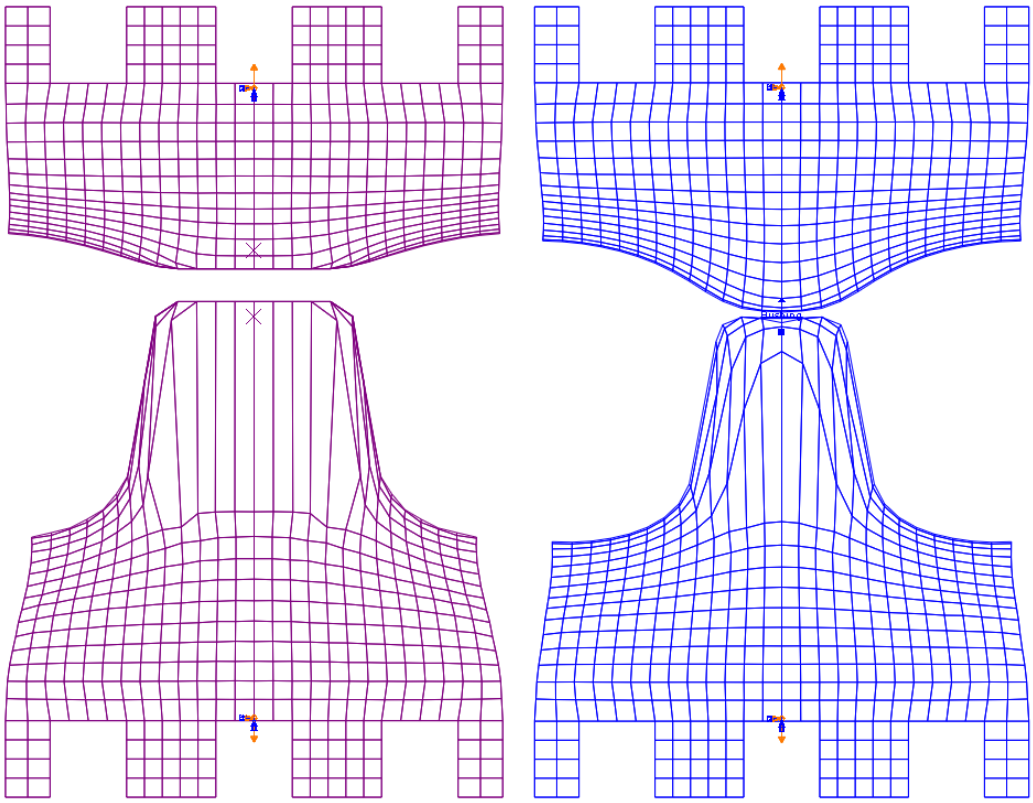

**Figure 4-14 Comparison of displacement between rigid body spot weld shown on left and "rigid" mesh independent spot weld shown on right.**

To compare the different kinds of spot-weld deformations, the font view of the pull coupon deformed images are superimposed to obtain a more clear understanding of the deformations. Figure 4-15 shows a superimposed image of a rigid mesh independent spot weld and an elastic, mesh independent spot weld. The normal stiffness value Kn

depends on the thickness values of the connected plates. The values used in this work are taken from curves found in [9]. The local variation in the deformation of the bottom and top plates does not exist in elastic mesh independent spot weld. In case of rigid spot-weld the connection between the two plates where highly rigid. The stiffness property along the pull direction of the spot weld allows it to deform in a more realistic manner.

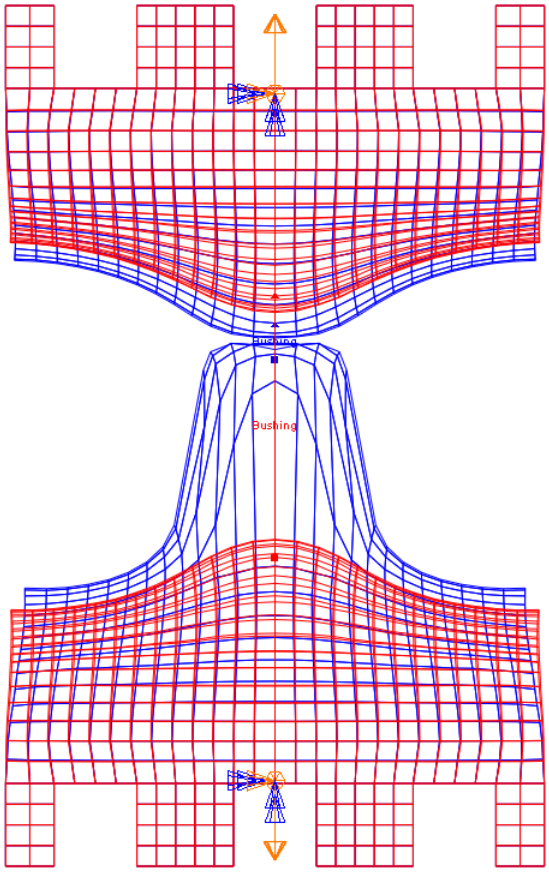


**Figure 4-15 Comparison of displacement between rigid mesh independent spot weld shown in Red, and elastic mesh independent spot weld shown in Blue.**

The elastic spot weld does not show any vigorous deformation at the spot weld location. For elastic mesh independent spot weld, both the top and bottom cups have a

semi spherical shape created at the center. When the deformation between the rigid and elastic spot weld is compared the elastic spot weld deformation is more realistic compared to the rigid spot weld.

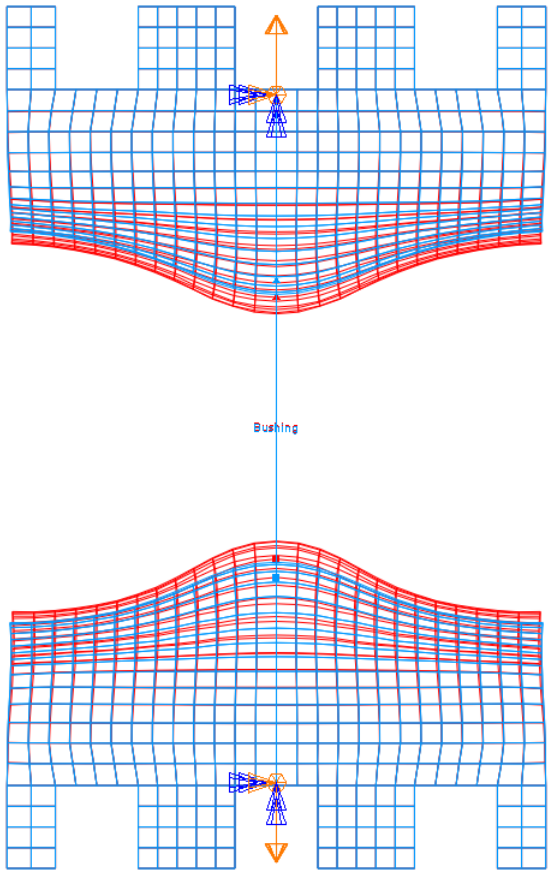


**Figure 4-16 Comparison of displacement between elastic mesh independent spot weld shown in Red, and elastic with failure mesh independent spot weld shown in Light Blue.**

The Figure 4-16 shows a superimposed deformation of elastic and failure mesh independent spot weld. The values used in the failure criteria in Equation (1) depend on the thickness and material properties of the sheets and are taken from Ref. [9]. The top and bottoms cups of failure spot weld expanded further because it has failed after reaching the failure force due to pulling. However, the elastic spot weld has kept the two plates intact with each other so it offers more resistance to expanding.

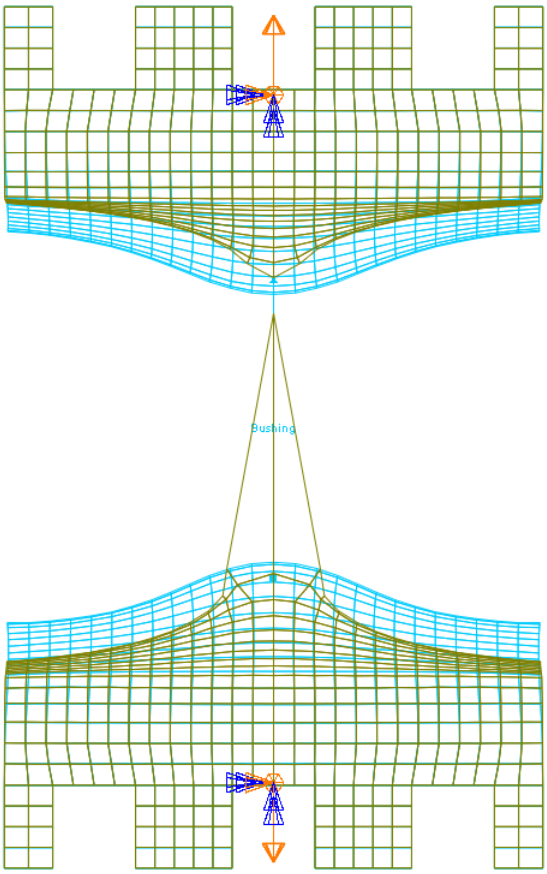


**Figure 4-17 Comparison of displacement between single node-to-node rigid spot weld shown in Green, and elastic with failure mesh independent spot weld shown in Aqua.**

Figure 4-17 is a superimposition of single rigid node-to-node connection and elastic spot-weld connection with failure criterion. In case of the single rigid node to node connection the bottom plate is deformed forming a local kink on the both plates. The single rigid node to node connection has created more local deformation where the mesh independent spot weld deformation is more distributed around the spot weld radius. The kink shows that the rigid node-to-node spot weld poorly represents the local deformation.

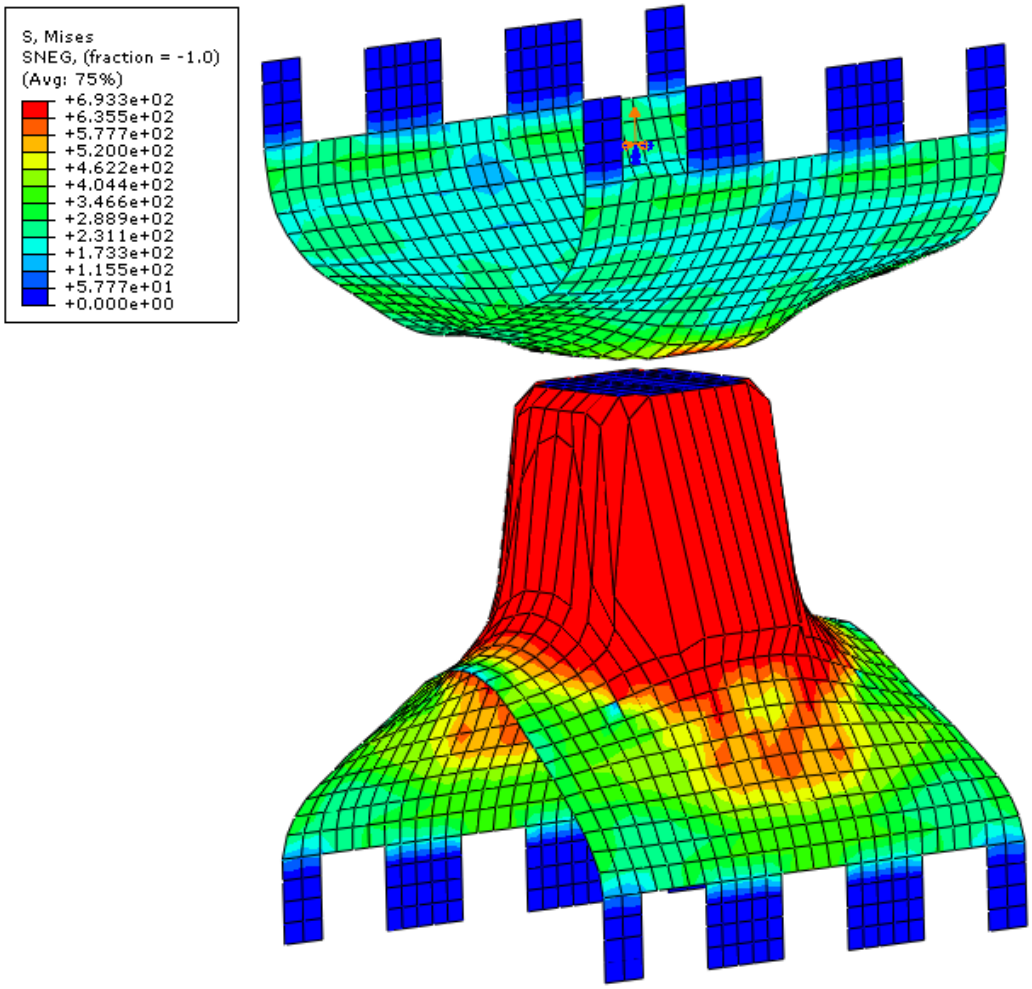


**Figure 4-18 Contours of Von-Mises Stress for rigid body spot weld**

The next step is to compare the location of high stress in the model. High stress gradients can occur near spot weld connections and thus should be calculated accurately so failure strength of the component can be evaluated correctly and because improper connections in the model can misguide the location of high stress acting areas. Figure 4-18 shows the Von Mises stress distribution for a rigid spot weld created using rigid body and Beam MPC. Since the set of nodes in the top and bottom are connected as a rigid body to a reference node, the spot weld connection behaves like a solid cylinder without any deformation. This creates a very high stress surrounding the rigid patch. As mentioned earlier the bottom plate has higher stress acting on it when compared to top plate, this is because the thickness of bottom plate is smaller than the top plate. Hence, the bottom plate offers low resistance to the pull load. In case of a rigid body connection, the high stresses observed at the area surrounding the rigid body spot-weld.

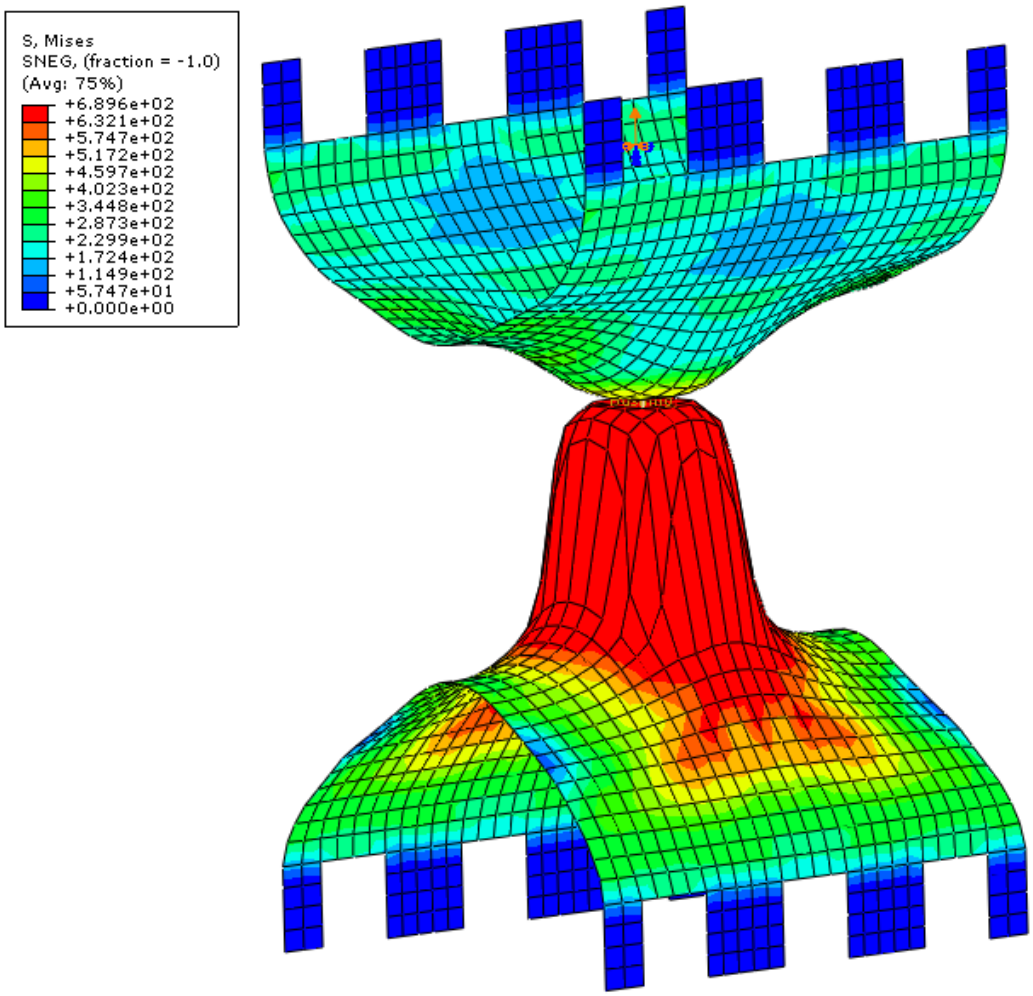


**Figure 4-19 Contours of Von-Mises Stress for rigid mesh independent spot-weld created using a connector element**

Figure 4-19 shows the Von Mises stress distribution for a rigid spot weld created using the Mesh independent spot weld option in ABAQUS. In case of mesh independent rigid connection, the elements involved in the spot weld deformed and high stress acts on the elements involved in the spot weld location. However, the deformation and stress distribution is almost the same between the both rigid body and rigid mesh independent

spot weld. The rigid spot weld connection created using mesh independent spot weld can use either a connector element or Beam MPC.

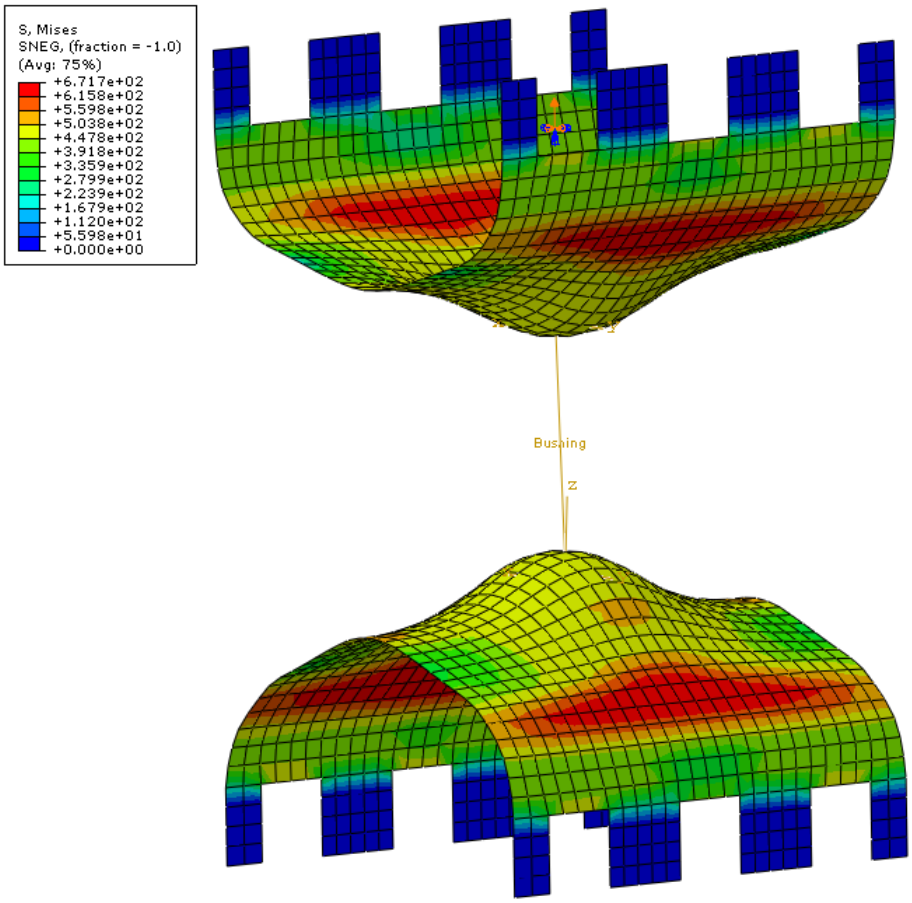


**Figure 4-20 Contours of Von-Mises Stress for elastic mesh independent spot-weld created using a connector element**

Figure 4-20 shows the Von Mises stress distribution for an elastic spot weld created using Mesh independent spot weld option in ABAQUS. The stiffness property along the pull direction of the spot weld allows the connection between the cups to deform. When compared to rigid spot weld, the high stress locations and deformation

pattern is entirely different. In case of elastic spot weld high stress is created in the edges where fillet is provided. Mostly this is the place where high stresses are expected when a cup-to-cup model with a spot weld at the center is axially pulled.

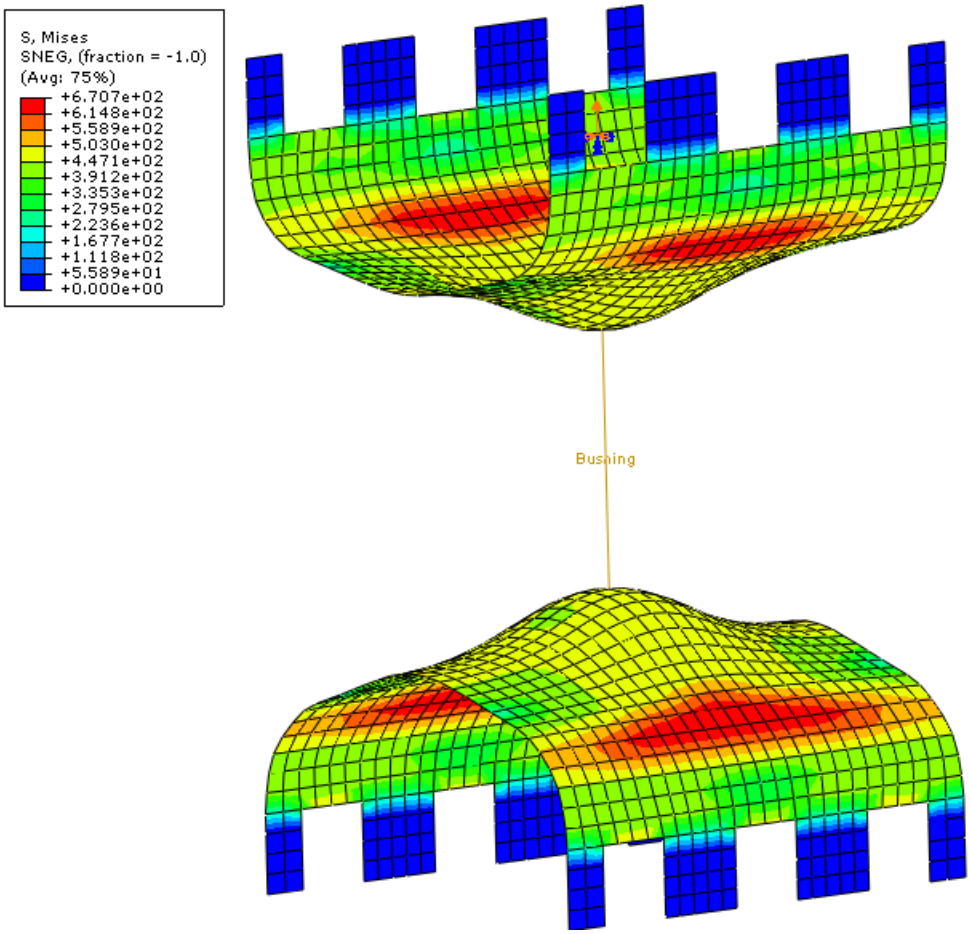


**Figure 4-21 Contours of Von-Mises Stress for elastic with failure mesh independent spot-weld created using a connector element**

Figure 4-21 shows the Von Mises stress distribution for an elastic, failure spot weld created using Mesh independent spot weld option in ABAQUS. The stiffness and the force at which failure occurs are provided along the pull- direction; the values are

taken from Ref. [9]. When compared to the elastic spot weld, maximum stress values are reduced. This can be explained by the spot weld has failed after reaching a particular force so it will not provide any resistance to the pull load after failure.

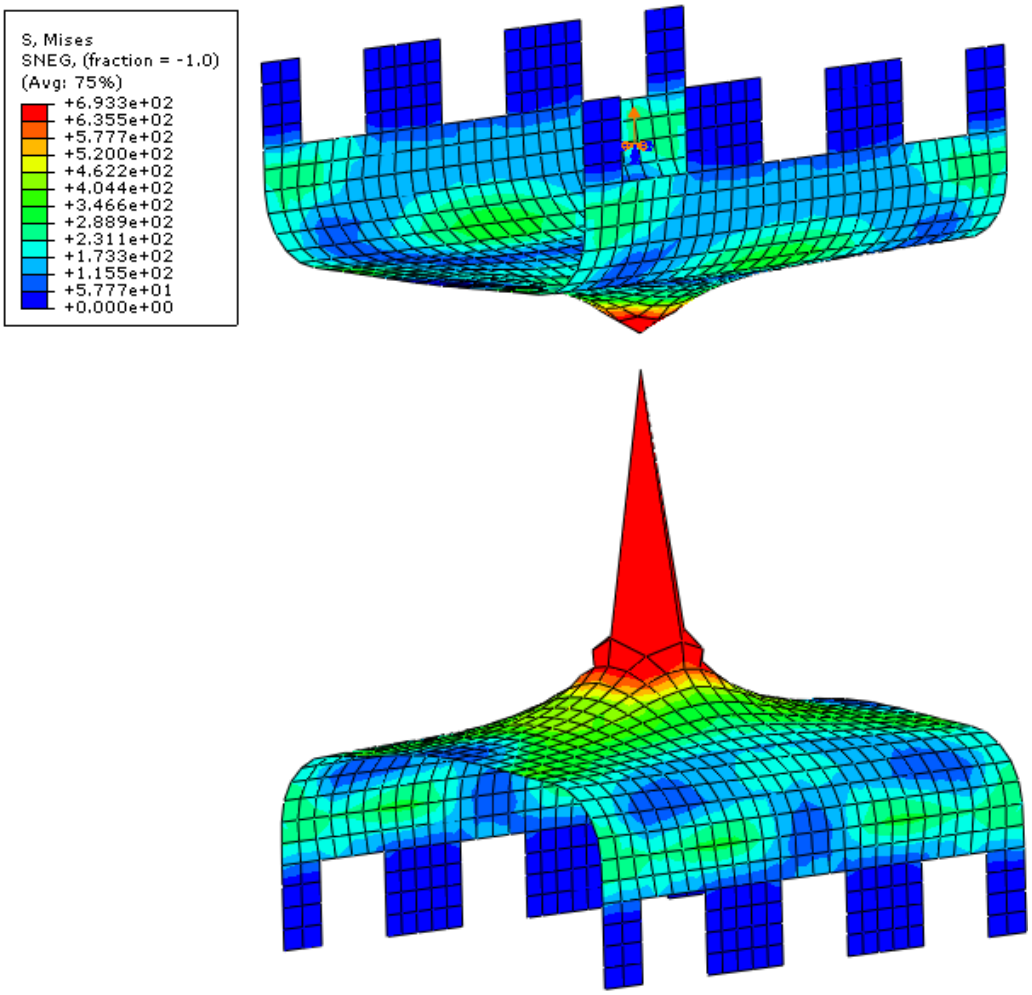


**Figure 4-22 Contours of Von-Mises Stress for single node-to node rigid spot weld connection**

Figure 4-22 shows the Von Mises stress distribution for a single node-to-node rigid connection spot weld. Since a single node in the top and bottom of the plates are connected, there is a local deformation kink created at the center of the both top and bottom plate. This kink shows that the rigid node-to-node spot weld model does a poor job representing local deformation and stresses.

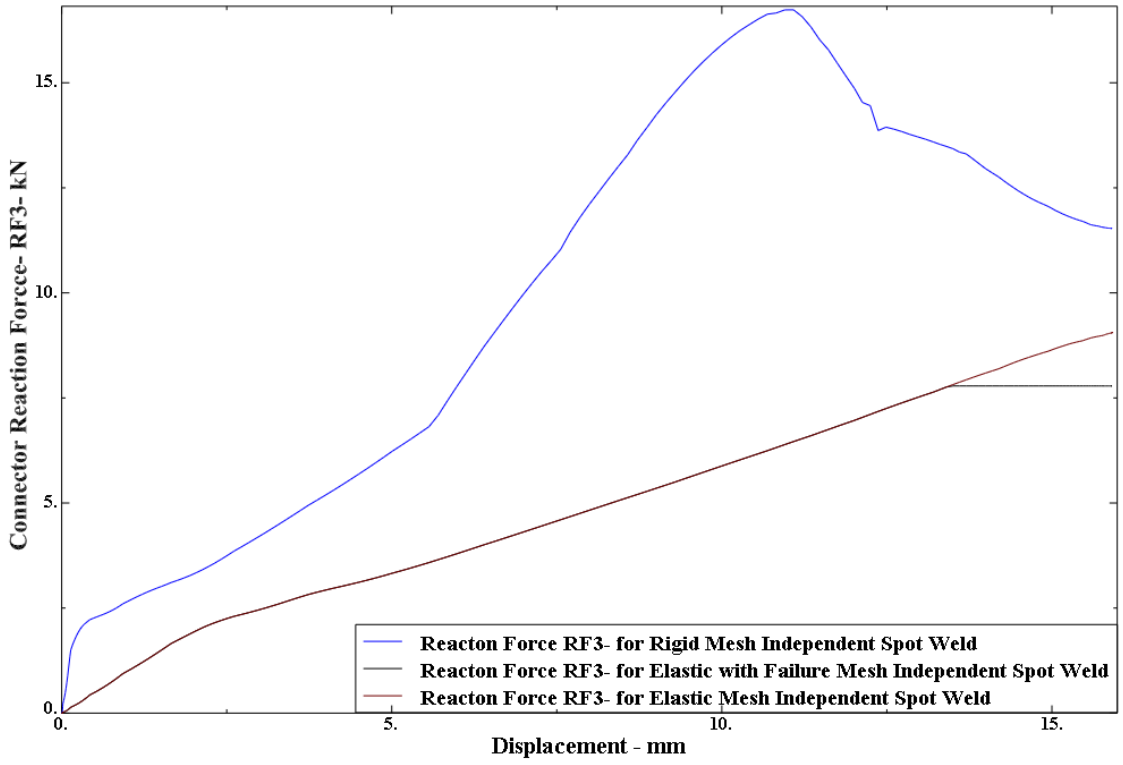


**Figure 4-23 Connector element reaction force along pulling direction for rigid, elastic and elastic with failure mesh independent spot weld**

Figure 4-23 shows the reaction force along z-direction for the rigid, elastic and failure spot-weld created in mesh independent spot weld option. Since the rigid spot weld has a very high resistance for deformation there has been very high force created at the

center of the spot weld. However, in case of elastic spot-weld where the connecting elements are allowed to deform the reaction force plot shows a much smaller force acting on it. The reaction force for the failure spot weld has followed the same path as the elastic spot weld but after reaching the prescribed failure force value (approx. 7.5 kN), it starts to not offer any resistance to the pull force. The use of the elastic spot weld model without failure, obtains a maximum force which is about 10% higher than the limiting force of 7.5 kN-mm observed in the failure model.

Figure 4-24 shows the internal energy absorption plot for single rigid node-to-node, rigid body and failure spot-weld connections. The internal energy includes elastic and plastic deformation strain energies. The rigid body spot weld shows a very high-energy absorption because it acts like a rigid cylinder connecting the two plates. The single node-to-node rigid connection and the failure spot weld mesh independent fastener show an initial path which is similar, but later there is a variation in values. When compared to rigid spot-weld, the single node-node rigid connection has yielded results closer to failure spot weld.

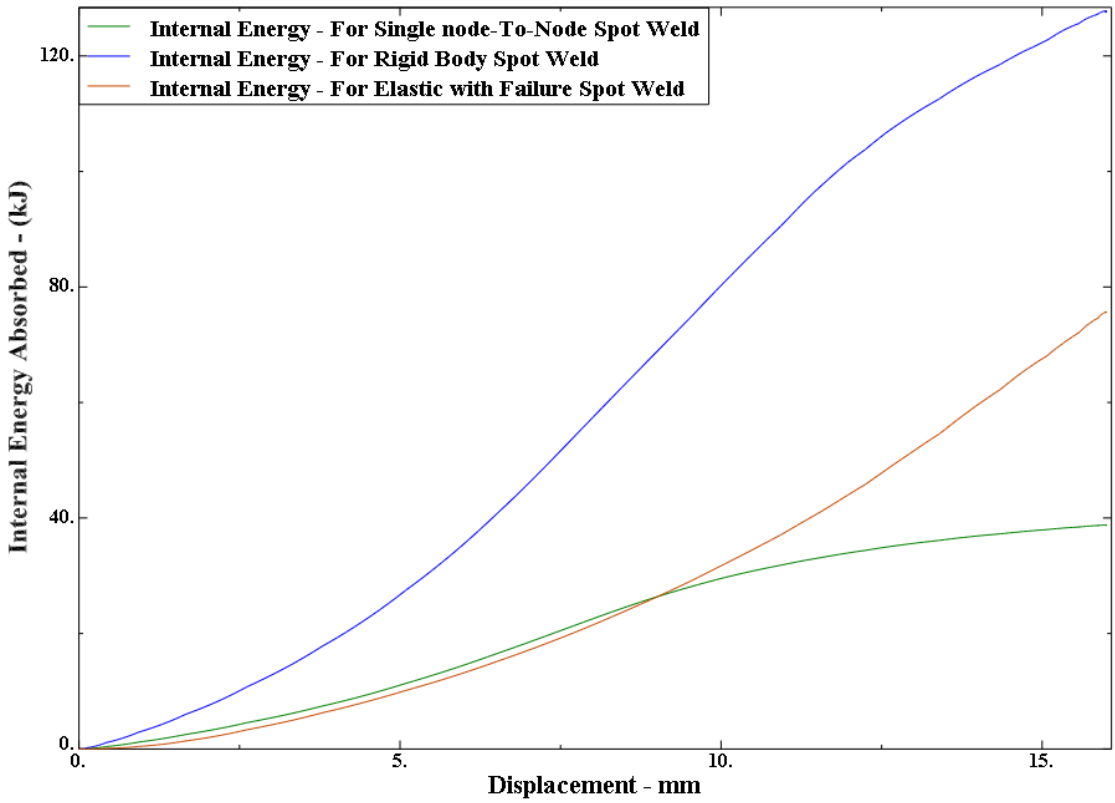


**Figure 4-24 Internal energy absorption for rigid body, single node-to-node and elastic with failure spot weld**

## 4.7 Results for Peel Test

To compare the different kinds of spot-weld deformations, the images are superimposed to obtain a clear understanding of deformation of spot weld connection. Figure 4-25 shows the side view of the peel coupon for the comparision of deformation between the rigid spot weld created using Mesh Independent spot and rigid body spot weld. The rigid body spot weld is more stiff when compared to rigid spot weld created using the Mesh independent spot weld. This difference is basically because in ABAQUS when a Mesh Independent spot weld is used to create the rigid spot weld between the

plates then the software internally calculates a high value of elasticity to the spot weld in order to relax the perfectly rigid condition.

In case of rigid spot weld created using rigid body connection and Beam MPC the element involved in the rigid body does not undergo deformation. In the case of rigid spot weld created using mesh independent spot weld component deformation is present and appears as expected for the peel test.

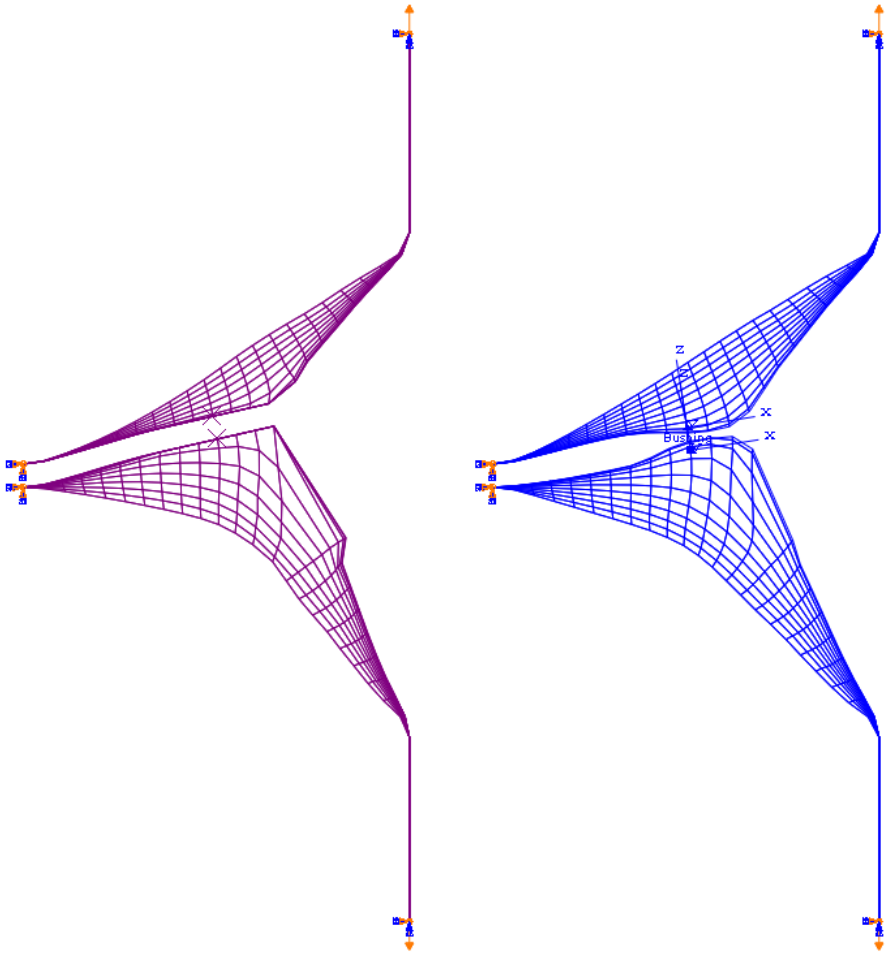

**Figure 4-25 Comparison of displacement between rigid body spot weld and rigid mesh independent spot weld for the peel test.**

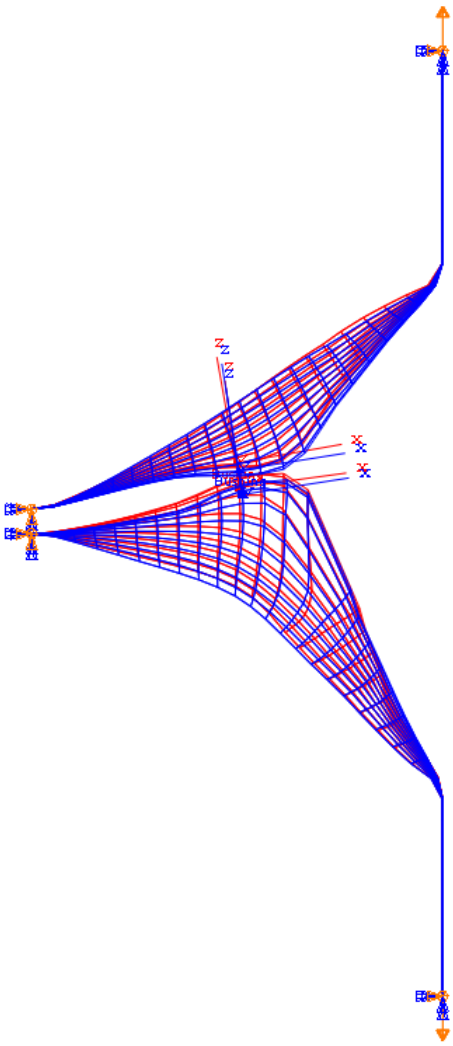

**Figure 4-26 Comparison of displacement between elastic mesh independent spot weld and elastic with failure mesh independent spot weld for peel test**

Figure 4-26 is a superposition of rigid spot weld and elastic spot-weld connection created by mesh independent spot weld. The deformation between the rigid and elastic spot weld is almost the same. In the case elastic spot weld, stiffness was provided but for rigid spot-weld, ABAQUS internally calculates a very high stiffness.

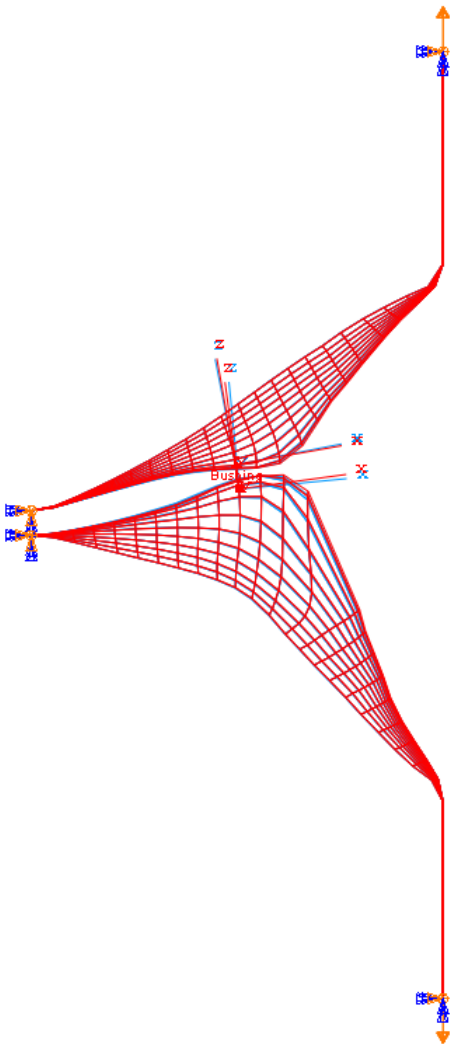

**Figure 4-27 Comparison of displacement between elastic mesh independent spot weld and elastic with failure mesh independent spot weld for peal test**

Figure 4-27 is a superposition of elastic spot weld and failure spot-weld connection created by mesh independent spot weld. In case of peel test, the deformation between the elastic and failure spot weld is almost the same. However, the failure spot weld expanded further because it has failed after reaching the failure force due to peeling. Figure 4-28 is a superposition of single rigid node-to-node connection and failure spot-

weld connection. In the case of the single rigid node to node connection, the bottom plate is deformed forming a kink on the both plates. The single rigid node-to-node connection has created more local deformation where the mesh independent spot weld deformation is distributed around the spot weld radius.

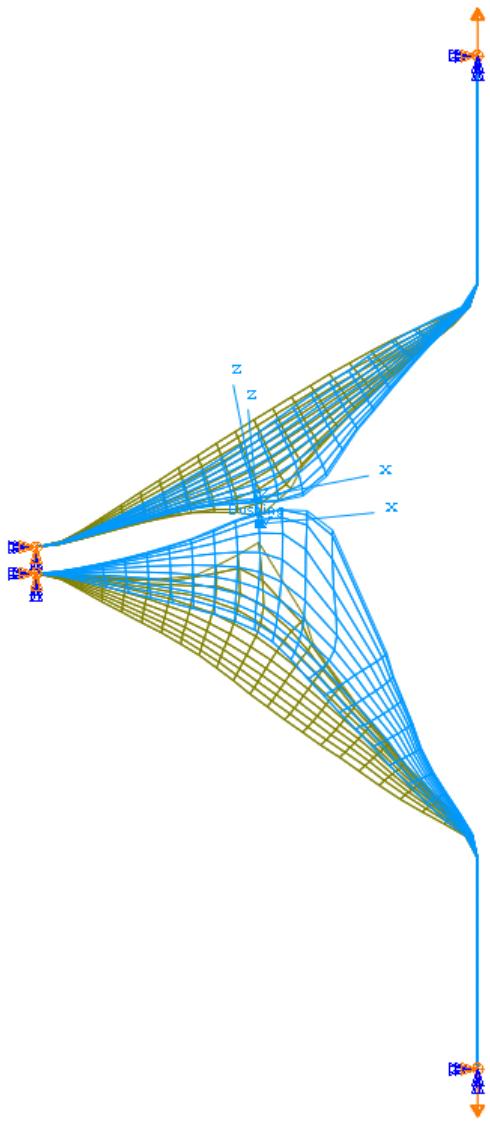


**Figure 4-28 Comparison of displacement between single node-to-node rigid spot weld and elastic with failure mesh independent spot weld for peel test**

In case of peel test, the reaction moment in the spot weld along the rotating direction of y-axis is compared between the mesh independent spot welds. Figure 4-29 shows the reaction moment along y-direction for the rigid, elastic and failure spot-weld created in mesh independent spot weld option. Since the rigid spot has a very high resistance for deformation there has been very high force created at the center of the spot weld. However, in case of elastic spot-weld the elements involve in spot weld connections are allowed to deform with the amount determined by the given stiffness value given. Therefore, the reaction moment plot shows a much smaller force acting on it compared to the rigid spot weld. The reaction force for the failure spot weld has followed the same path as the elastic spot weld but after reaching the prescribed failure moment value (approximately 10 kN-mm), it does not offer any further resistance to the pull force.

During the initial crush displacement up to about 0.4mm, the slope of the reaction moment curve vs. displacement curves is relatively steep and proportional, indicating a large linear stiffness for small deformation. As deformation progresses beyond 0.5mm, the curves flatten indicating a softening effect due to geometric nonlinearity. For deformations beyond 1.0mm a hardening effect is observed up to about 4.0 mm where material plastic strains are developed limiting the maximum force which can be achieved. The use of the elastic spot weld model without failure, obtains a maximum force which is about 10% higher than the limiting force of 10 kN-mm observed in the failure model.

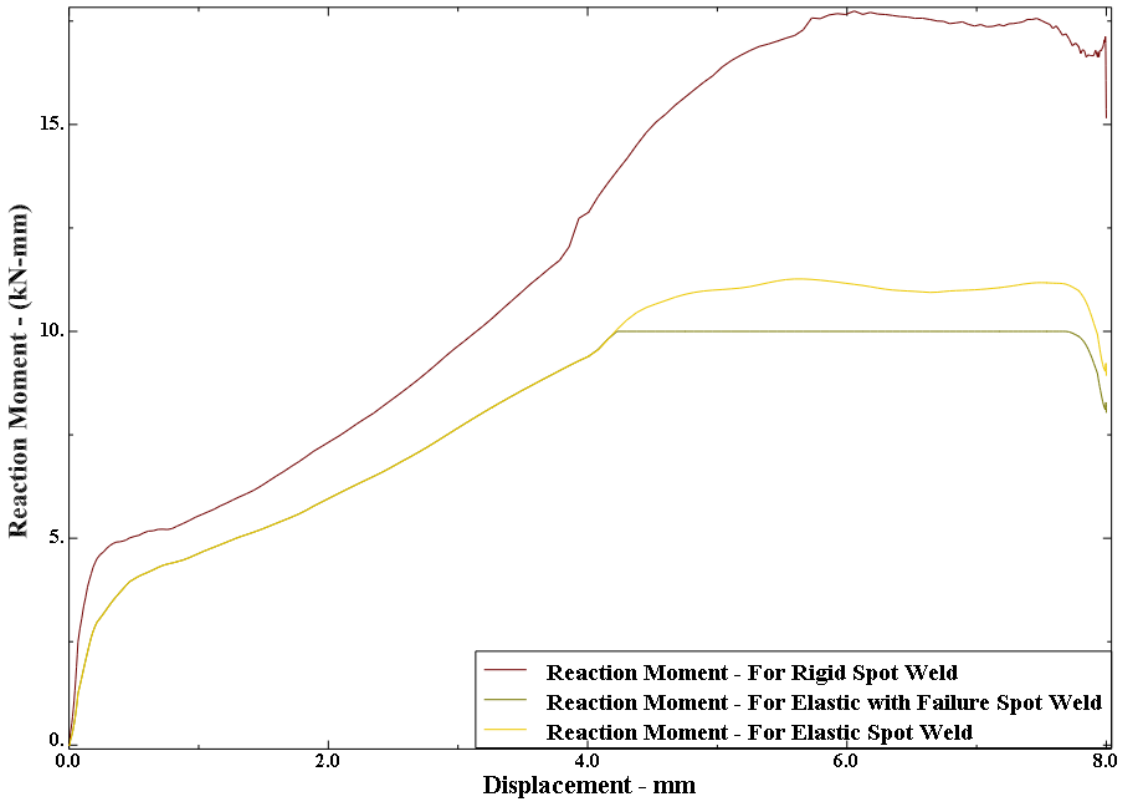


**Figure 4-29 Connector element reaction moment for rigid, elastic and elastic with failure mesh independent spot weld for peel test**

Figure 4-30 shows the internal energy absorption plot for single rigid node-to-node, rigid body and failure spot-weld connections. The rigid body spot weld shows a very high-energy absorption because it acts like a rigid cylinder connecting the two plates. However, the single node-to-node rigid connection and the failure spot weld of mesh independent fasteners has shown much smaller energy absorption. When compared to rigid spot-weld, the single node-node rigid connection has given results closer to failure spot weld.

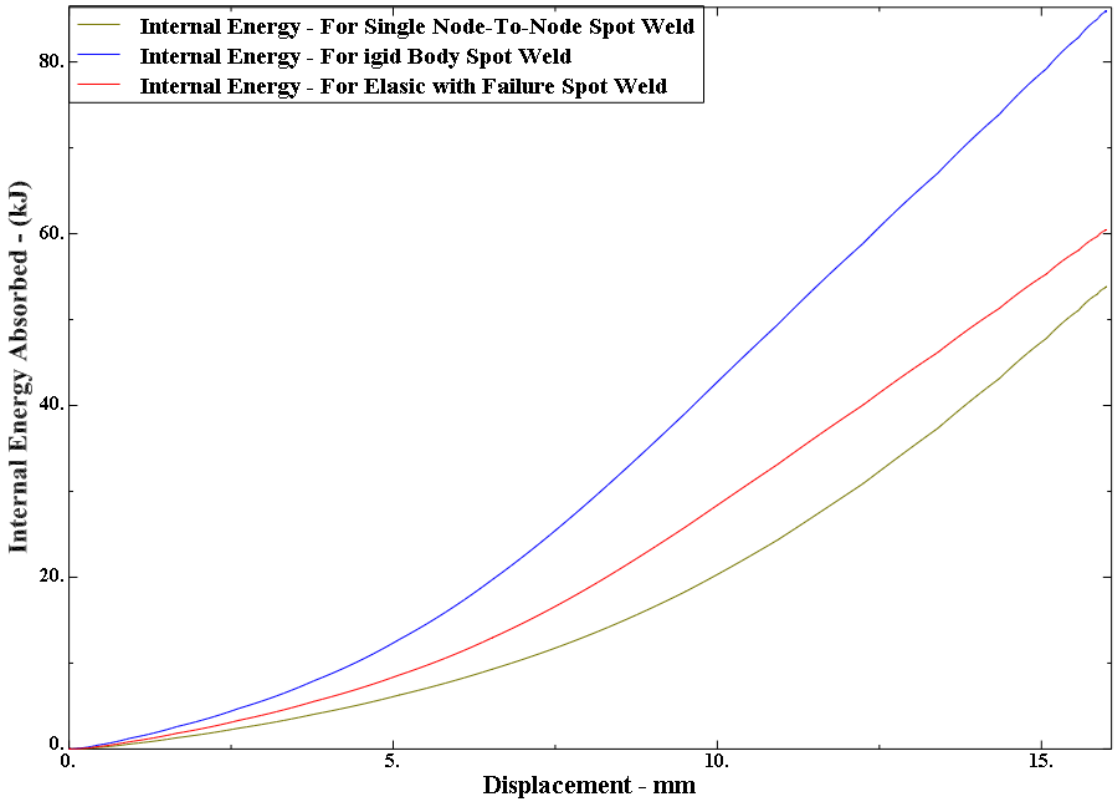


**Figure 4-30 Internal energy absorption for rigid body, single nod-to-node and elastic with failure spot weld for peel test**

# CHAPTER FIVE

# SPOT WELD ON A REAL STRUCTURE OF A VEHICLE

In the previous Chapter, the various types of spot-weld models were studied on a single spot weld for simple pull and peel tests with isolated load paths. Results from these tests showed large differences in the results can occur between each type of spot weld modeling technique. However, for full vehicle models, node-to-node spot welds are often used for simplicity. To understand more about the behavior of spot weld modeling behavior in a realistic automotive component, a front longitudinal rail constructed from two stamped thin sheet metal parts joined with spot welds at equal spacing along its length.

## 5.1 FEA Model From National Crash Analysis Center

Figure 5-1 shows an entire FEA model of a Dodge Neon obtained from the National Crash Analysis Center (NCAC). Since NCAC uses LS-DYNA for crash analysis, the FEA model is in LS-DYNA format. In this full vehicle model, all spot welds are modeled with simple node-to-node rigid connections. The next phase of study is to select one component from this FEA model and to compare how the energy absorption of the component varies when this node-to-node rigid connection is replaced with a mesh independent spot weld connection. Figure 5-2 shows the single node-to-node spot-weld connection in the entire FEA model of the Dodge Neon.

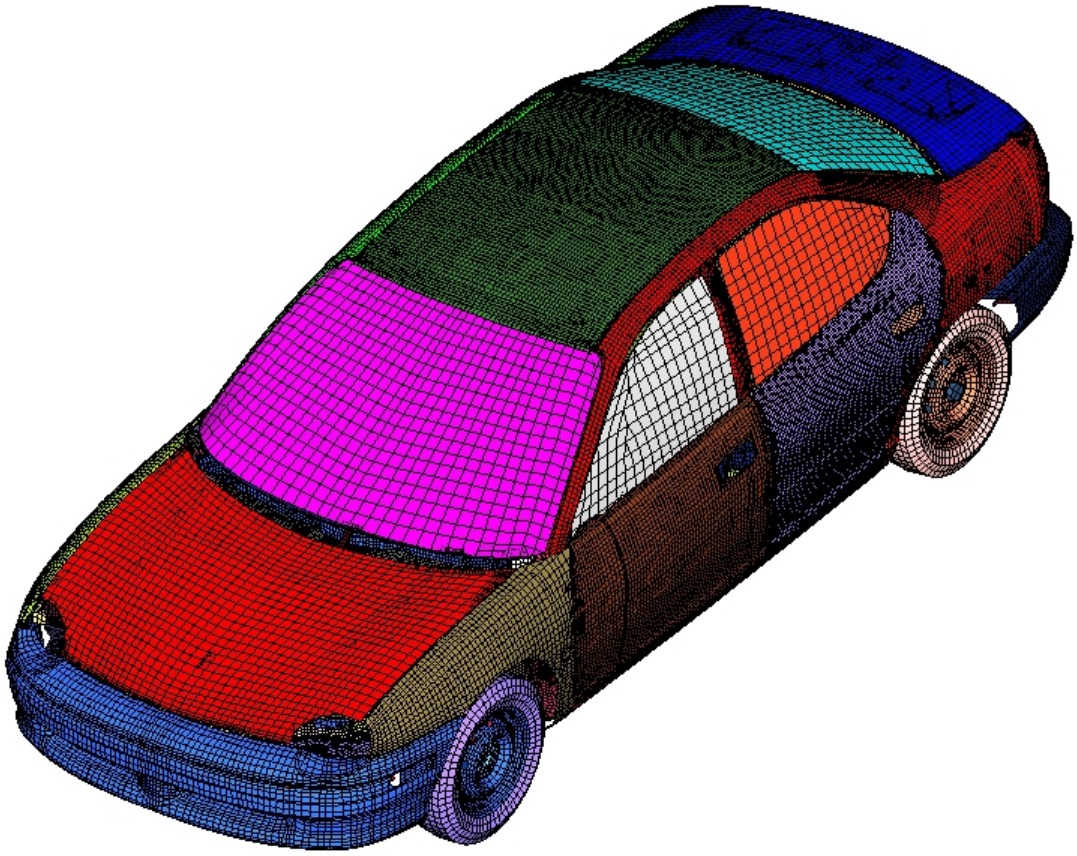

**Figure 5-1 Full vehicle FEA model created by National Crash Analysis Center**

**Figure 5-2 Single node-to-node rigid spot welds in the entire FEA model of Dodge Neon**

## 5.2 Components Involved in Frontal Crash

Since the FEA model created at NCAC is for frontal crash analysis, the component that plays an import role in the frontal crash energy absorption is selected for further study. Therefore, a study on how energy is distributed during frontal impact was done. Figure 5-3 shows some of the important structural components in a modern vehicle that plays an important role in frontal crash of a vehicle. The longitudinal beams are designed to crumple in a controlled manner and absorb kinetic energy during the collision. Lateral connections help stabilize and transfer loads between each side of the vehicle. This load transfer is important for collisions where only one longitudinal beam is loaded directly. Loads from the longitudinal beams are transferred into the passenger compartment through the firewall into the A-pillars, tunnel and sill. The structures forming the passenger compartment should not deform or protrude significantly,

maintaining and intact passenger capsule during the collision. Important components not seen in Figure 5-3 are the engine and wheels. Both of these components can contact the firewall with sufficient deformation of the front structure. These contacts usually introduce frontal compartment intrusion and the increased risk of occupant injury.

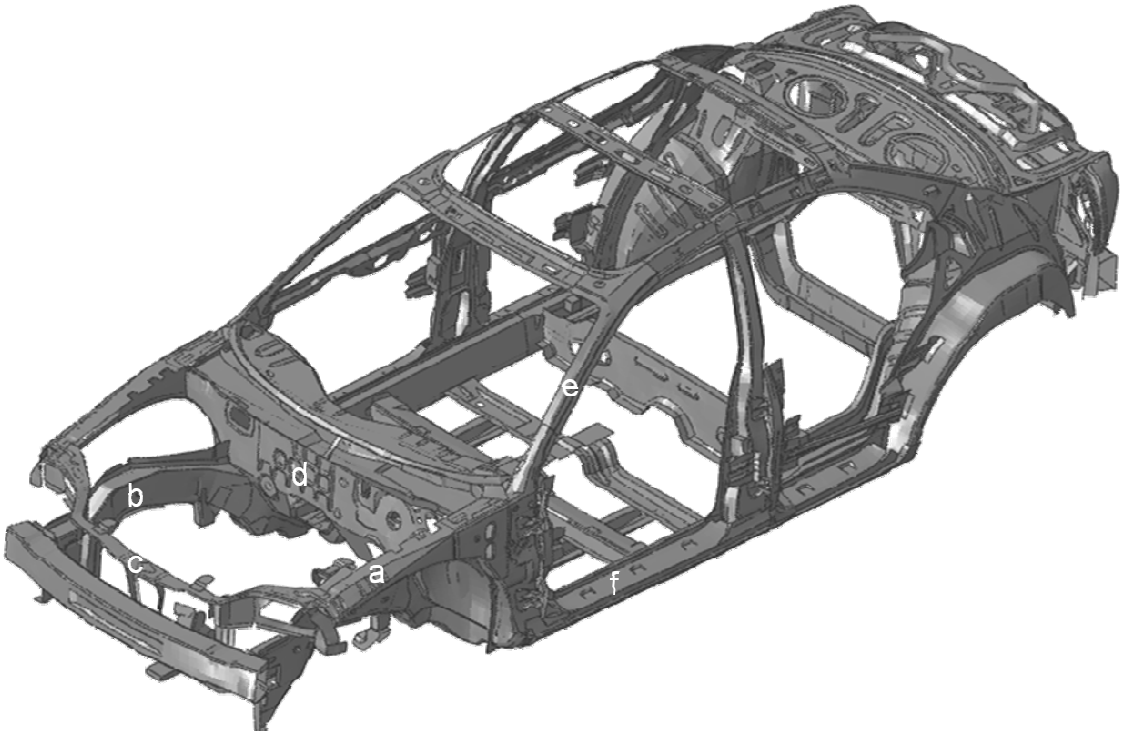


**Figure 5-3 Structural components in front crash protection: a – upper longitudinal, b – lower longitudinal, c – lateral connection, d – firewall, e – A-pillar, f - sill**

In frontal impact situations, the goal is to have the structures in Figure 5-3 interact with the corresponding structures on the collision partners. However, for other impact conditions (oblique, side and rear impacts) this is not possible. As seen in Figure 5-3, for side impact there are no corresponding structures in the side of the vehicle other than the

door. In path of energy absorption during frontal crash, lower longitudinal rail plays an important role in absorbing the kinetic energy of the system. Figure 5-4 shows the lower longitudinal rail assembled in the Dodge Neon, which plays an important role in energy absorption. A large amount of research and development for this kind of structure is done in industry to improve the energy absorption of the component so that the force transferred to the driver compartment during frontal crash is reduced.

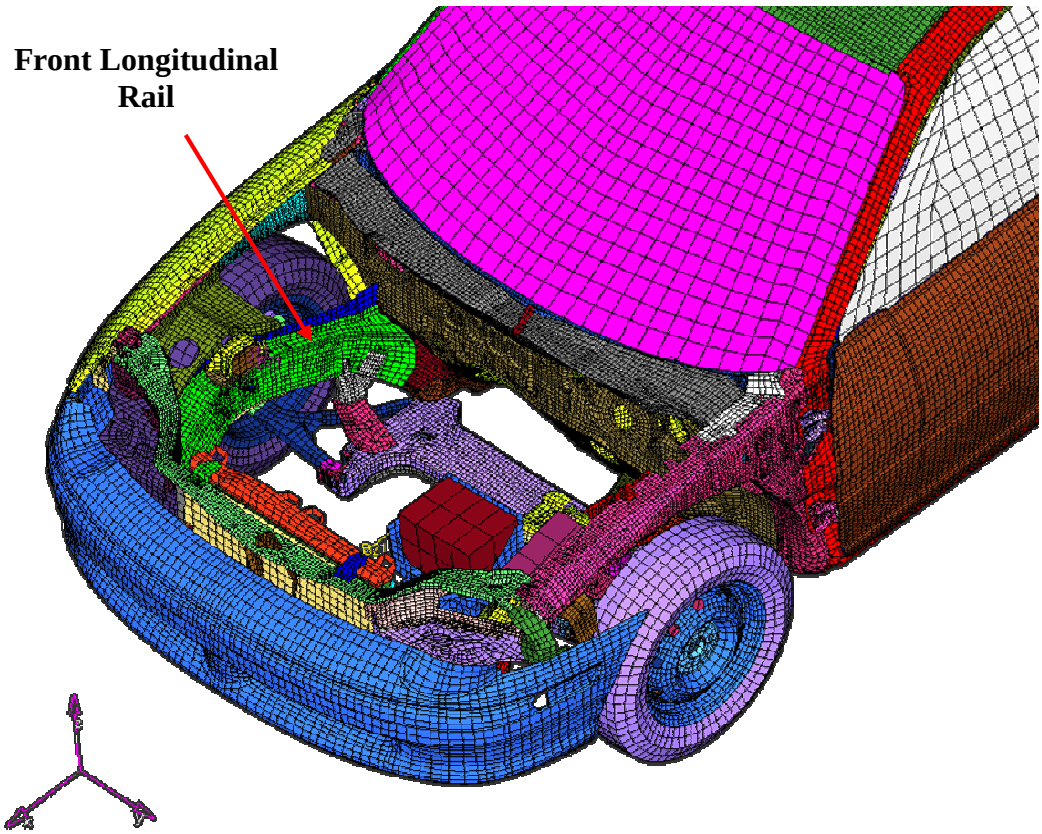


**Figure 5-4 Location of lower frontal longitudinal rail of Dodge Neon**

## 5.3 Reverse Engineering of a FEA Model of Frontal longitudinal rail

The frontal logitudinal rail is thin-wall structure which is manufactured by stamping process. It has two components, the open section which has hat cross section and the bottom plate which are joined together using spot weld. To study the energy absorption of the longitudinal rail alone it has to be seperated from the entire vehicle FEA model of the car. The entire FEA model is imported into the Hypermesh and the longitudianal rail is seperated from the entire FEA model. Figure 5-5 shows the FEA model longitudinal rail which is seperated from the entire FEA model.

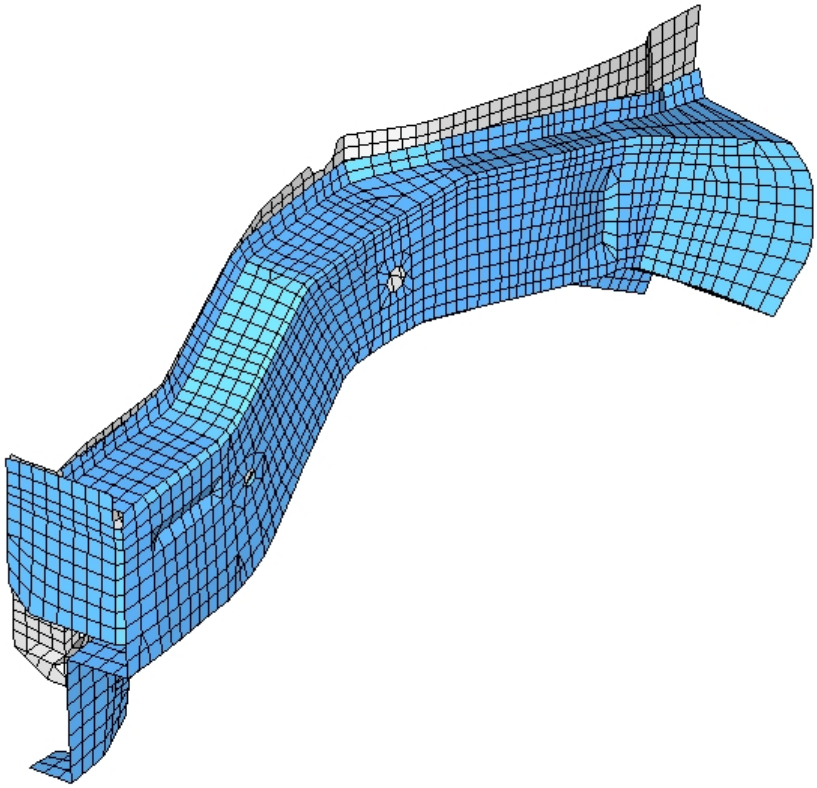

**Figure 5-5 FEA model of frontal longitudinal rail in HYPERMESH**

Figure 5-5 shows the longitudinal rail obtained from NCAC, it has a course mesh with element size between 7 mm to 20 mm. In order to perform a study of the component, a proper mesh on the component must be provided. The entire frontal longitudinal rail CAD model is recreated in CATIA V5 with the FEA mesh as the input. A surface extraction from the FEA mesh option in HYPERMESH is used to create the surface of the longitudinal rail. Figure 5-6 shows the surface of longitudinal rail extracted from the mesh. From Figure 5-6 it can be observed the extracted surface does not have a proper tangent continuity between the surfaces. So the surface data is saved in IGES format in Hypermesh and exported into CATIA v5 for further re-creation of the model.

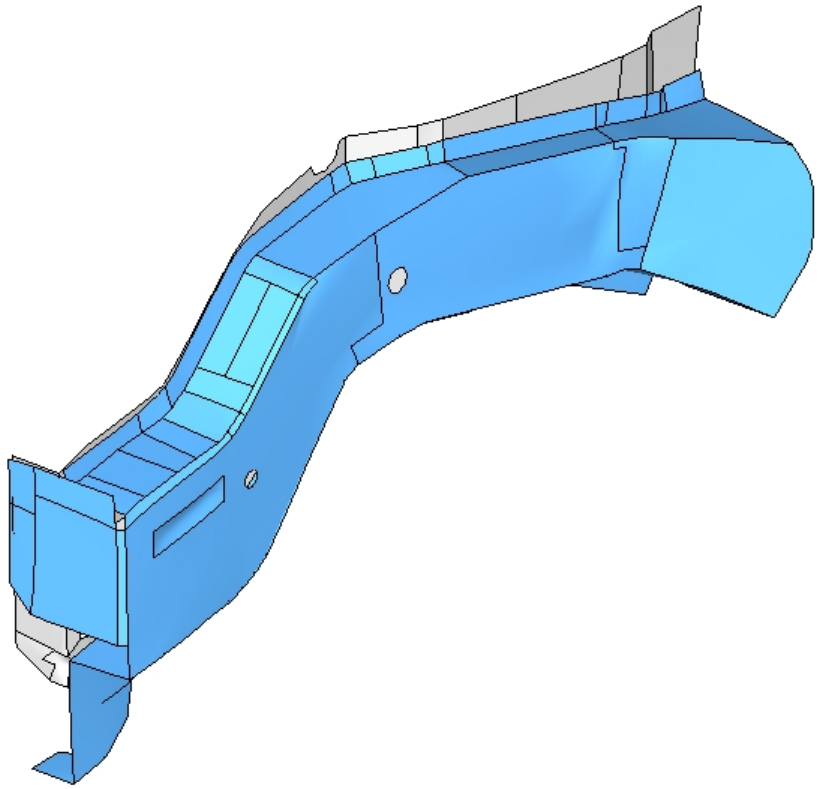

**Figure 5-6 Surface of longitudinal created from mesh in HYPERMESH**

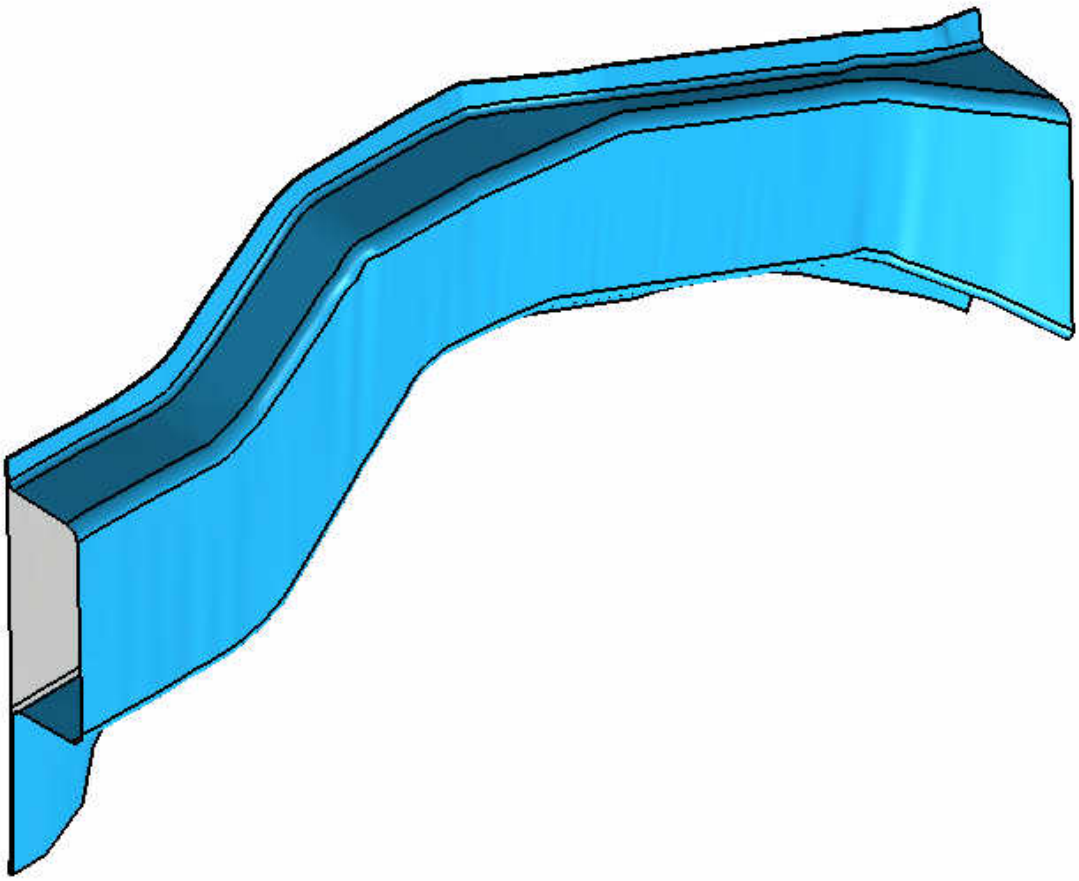

**Figure 5-7 CAD model of frontal longitudinal rail created in CATIA V5**

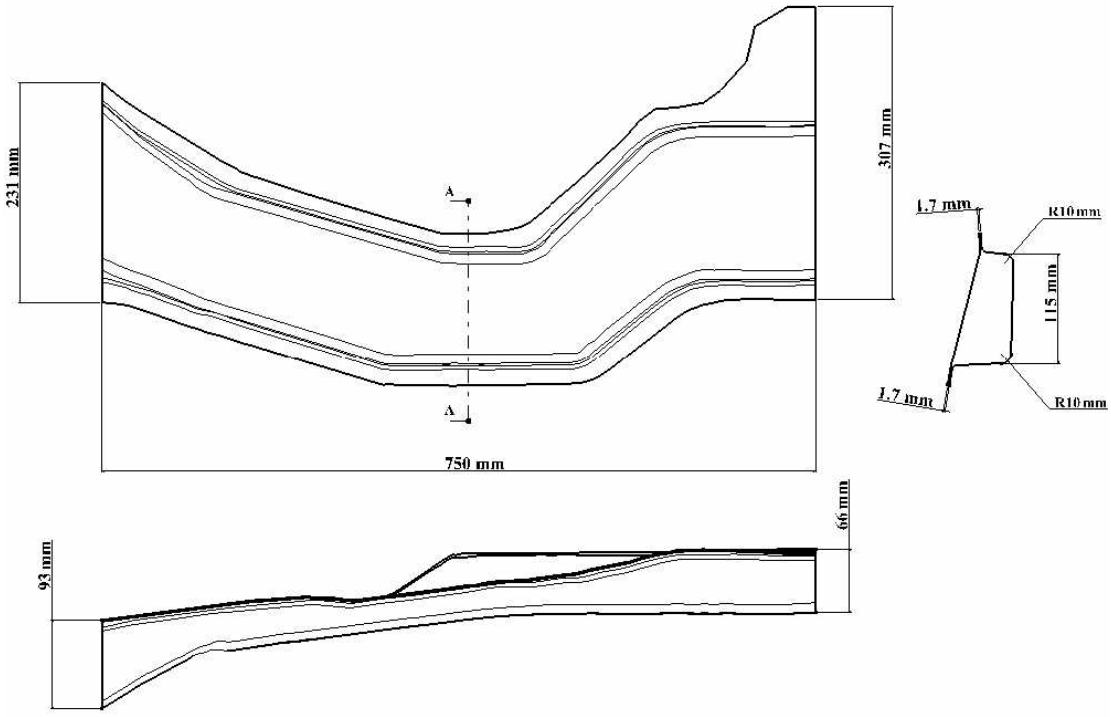


**Figure 5-8 2D drawing for frontal longitudinal rail created in CATIA V5**

Using the advanced surface creation option in CATIA V5, the surface of the longitudinal frontal rail is created. Figure 5-7 shows the CAD model of the frontal longitudinal rail. The overall dimension of the longitudinal rail is shown in Figure 5-8.

## 5.4 Test Procedure To Study Frontal longitudinal Rail

To conduct the impact testing of the longitudinal rail there are various types of test sep-ups like Drop hammer, pendulum or an inclined sled that are available. Figure 5-9 shows the drop hammer test step used to study the crushing energy absorbed of a thin-walled closed structures. It has a heavy mass lifted up to a specific height from the ground and that stores a potential energy in it. When the mass is allowed to free fall from that height, it gains more Kinetic energy from the loss of potential energy stored in it.

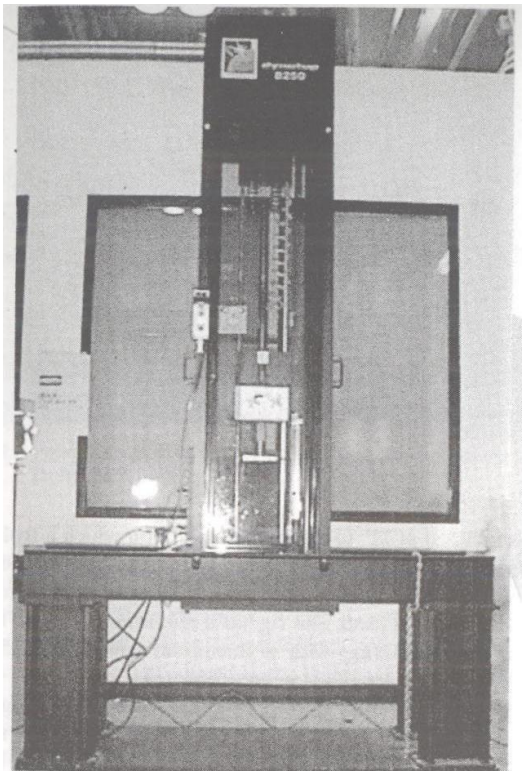

**Figure 5-9 Drop hammer test step up for crushing the thin walled structure [16]**

The test-step has a fixture in the bottom to hold the specimen during crushing with a free fall heavy weight. The maximum velocity achieved in the experiment is based on the total height of lift of the drop hammer. Other means such as compressed air or springs used at the top of the drop hammer can accelerate the heavy weight to a higher crushing velocity [16]. With the drop hammers shown in Figure 5-9, the mass can be lifted 1.5 m high and has mass of the impact object can be varied up to 44.89kg. When mass is gravity driven the crushing velocity is in the range 0.61-3.66m/s and it can be increases up to 3.66-13.41 m/s when the mass is dropped with pneumatically assisted system.

**Figure 5-10 sled test step up with ramp for crushing the thin walled structure [16]**

Figure 5-10 shows another method for conducting impact tests, a sled testing facility at Cranfield impact centre. At FORD, to study the energy absorption of the longitudinal rail, they have used the sled test rig [16]. In the sled test, a ramp with a mass at the top is used. The ramp has an inclination of 11 degrees to the horizontal, upon which a trolley floats on four air pads provides a frictionless motion and repeatable impact speeds. Figure 5-11 shows the sled test setup with the ramp with the mass at the top, which will slides down to crush the specimen placed at the lower end of ramp. Low impact speeds achieved by using gravity rolling of the mass on ramp, but for higher speeds elastic cord is used to increase the velocity. Pendulums can also create a same type of impact loads on thin structures. One such rig shown in Figure 5-11 and is available from Cranfield.

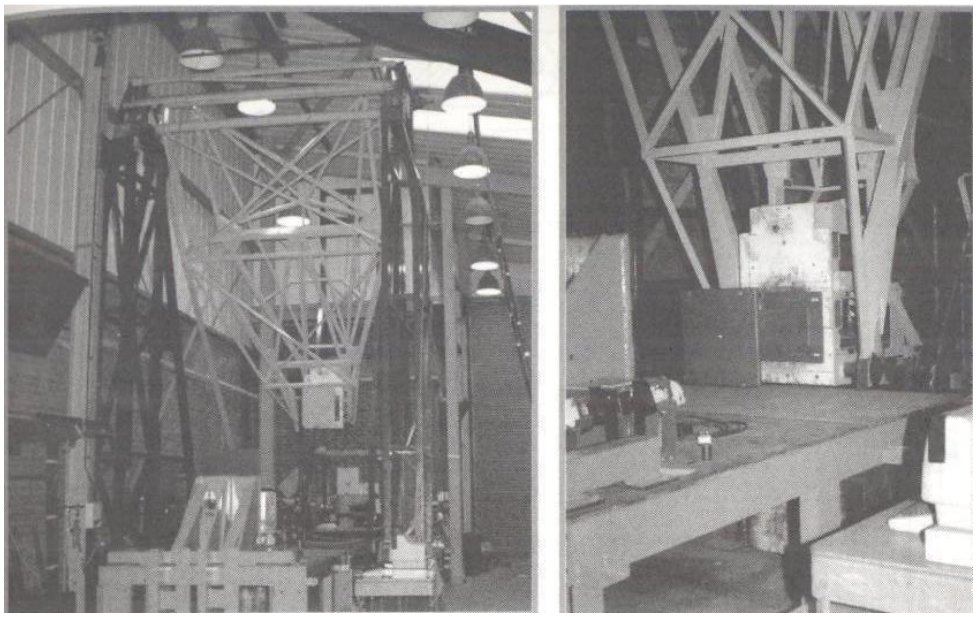

**Figure 5-11 Pendulum test step up with ramp for crushing the thin walled structure [16]**

Based on the above various experimental setups the study on longitudinal rail is done using a Commercial FEA package by placing a longitudinal rail between two rigid walls. One rigid end wall is fixed in all degrees-of-freedom, and the other rigid end wall is allowed to translate axially alone such that the longitudinal rail is crushed. Figure 5-12 shows the experimental setup, the front end of the longitudinal rail is fixed to a rigid wall and the rear rigid wall is allowed to translate in x-direction so that the component is crushed.

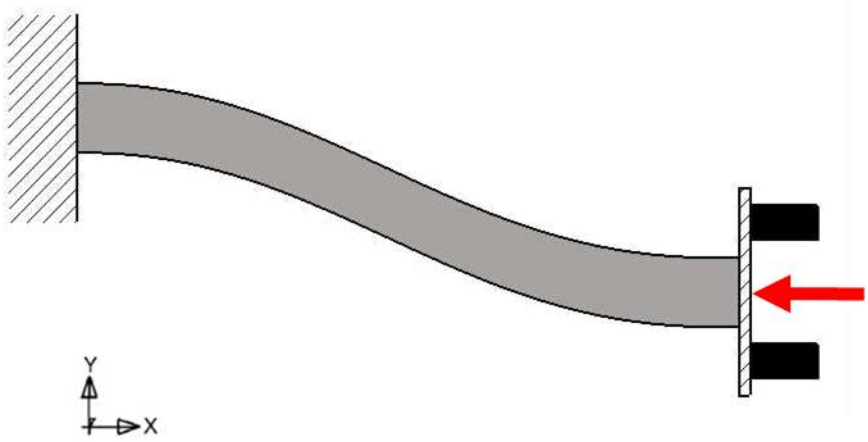


**Figure 5-12 Experimental set up to crush the frontal longitudinal rail**

## 5.5 Finite Element Model of Frontal longitudinal Rail

The CAD model described in Section 5-3 is imported into HYPERMESH in the IGES format. The CAD model is meshed with 4-node doubly curved thin or thick shell, reduced integration, hourglass control, finite member strain element (S4RS) and 3-node triangular shell, reduced integration, hourglass control, finite member strain element (S3RS), with shell size of 4.5 mm. A total of 21,361 nodes and 20,838 elements are present in the finite element mesh of the geometric model: Triangular elements are better able to fit in narrow corners in the model. Figure 5-13 shows the Mesh created in HYPERMESH for the frontal longitudinal rail.

**Figure 5-13 Mesh on frontal longitudinal rail created using HYPERMESH**

A simple node-to-node rigid connection, rigid Mesh Independent spot weld, and elastic mesh independent spot weld is created on the sides flanges at an equal distance of 50 mm along the length with the spot weld diameter of 6mm. Figure 5-14 shows the experimental setup in ABAQUS V6.8. It has two rigid walls in the front and rear of the longitudinal rail. The mesh element size is bigger in the both front and rear wall because both are made rigid. RP-1 is the reference point on the front wall and RP-2 is the reference point on the rear wall. The front and rear walls made rigid to their respective reference point. A displacement boundary condition of 300 mm is applied to the rear end wall to crush the frontal longitudinal rail in ABAQUS/EXPLICIT for a time of 200 ms.

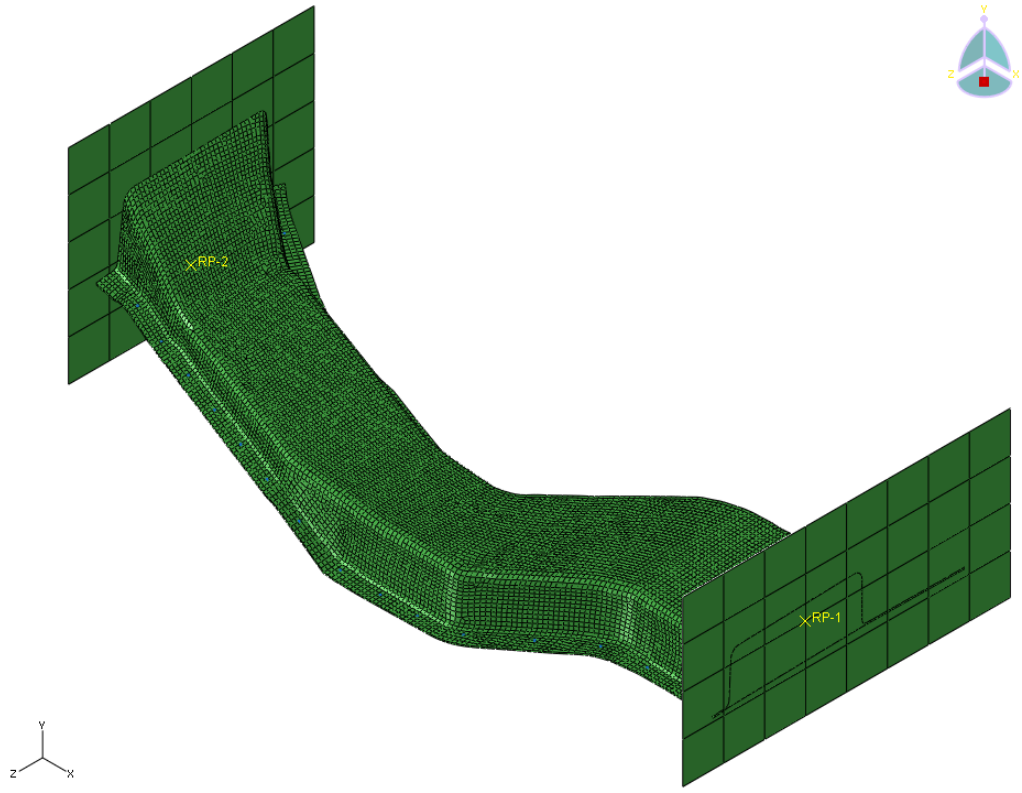


**Figure 5-14 FEA model of the frontal longitudinal rail created in ABAQUS**

In the experiment done on longitudinal rail by FORD [15], seam welding has been provided between the rear end of the longitudinal rail and the plate. This is to secure the longitudinal rail between the two rigid walls so that while crushing it will not slip down. To replicate the same welding effect, the ends of the longitudinal rail are tied to the rigid plate using Multi-point constraints. Figure 5-16 shows the MPC constraint at the front end of the longitudinal rail. The rigid body option can be used instead of MPC but in ABAQUS the reference point involved in Rigid body cannot be used has reference point to another rigid body. Therefore, the end nodes of the longitudinal rail are tied to the reference point of the walls by using MPC. For the front-end rigid wall all the degree of freedom where set to zero, where as for the rear end rigid wall, an axial displacement of 300 mm is provided in a smooth step over 200ms.

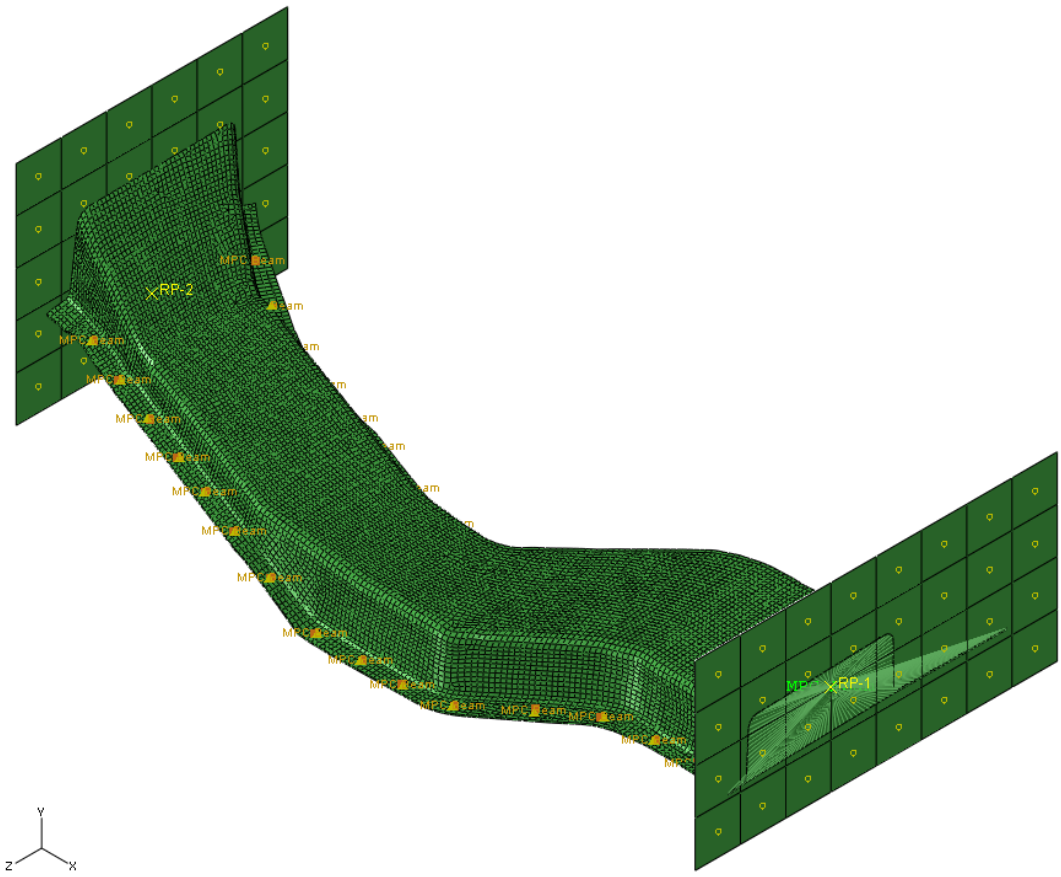


**Figure 5-15 Single node-to-node rigid connection on both side flanges**

Figure 5-15 shows the model setup for node-node rigid connection spot weld created between on the both side flanges at a distance of 50 mm and the multipoint constraint used to create the node-to-node rigid connection. The mild steel material properties for the both top open section and the bottom plate was provided, has discussed in Chapter 2. The component is crushed to compare the variation in the energy absorption of the frontal rail with node-to-node rigid connection, mesh independent rigid spot weld and mesh independent elastic spot weld connection. Figure 5-17 shows the spot welds evenly spaced at a distance of 50 mm between the top open section tube and bottom

plate. Figure 5-16 shows the spot of 6 mm diameter provided on the both the side flanges. A separate reference node for each spot weld is provided on the top surface of the flanges. Based on the radius of the spot weld a distributed coupling is created between the top open section and plate flanges. In the next chapter, different shapes of frontal longitudinal rail that will increase energy absorption and increase crush force efficiency are examined. The frontal longitudinal rail with rigid mesh independent spot weld is considered the base component for all comparisons.

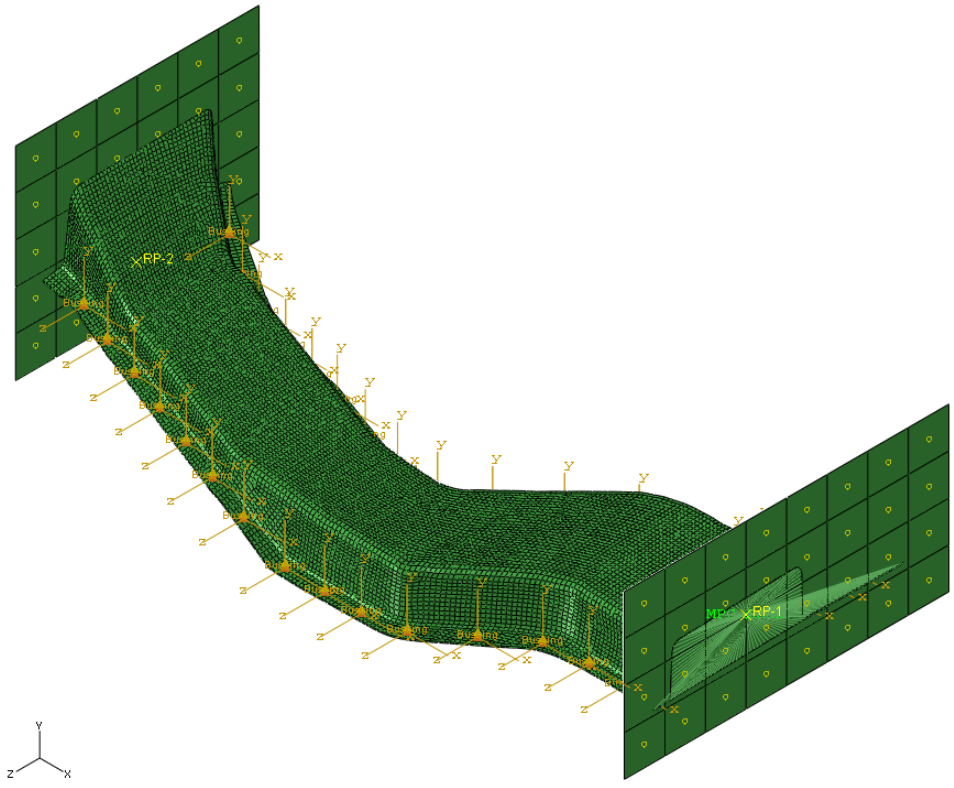


**Figure 5-16 Rigid mesh independent spot weld on both side flanges**

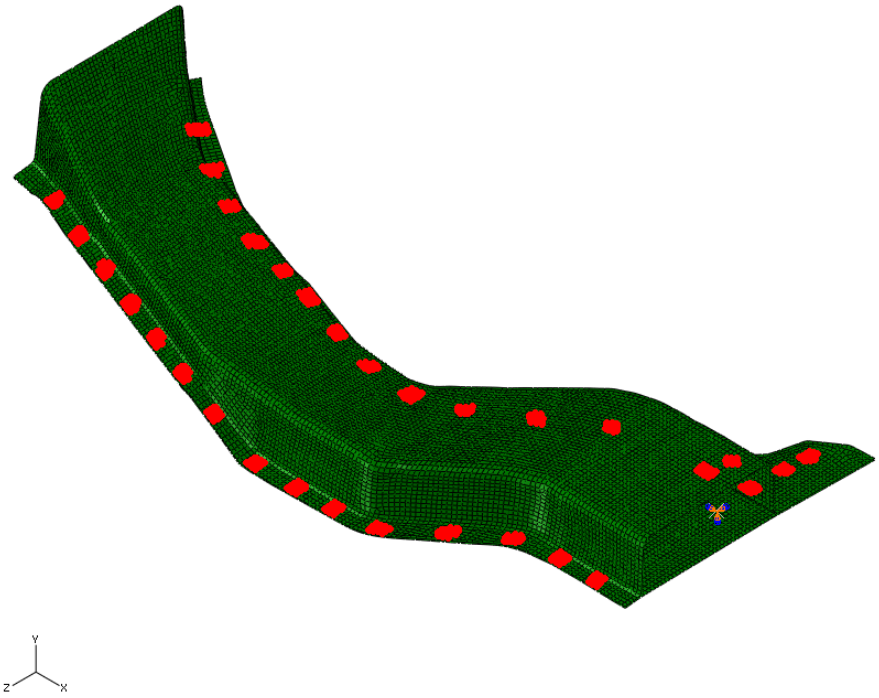

**Figure 5-17 Nodes involved in mesh independent spot weld for a spot weld diameter of 6mm on both side flanges**

## 5.6 Comparison of Results for Spot Weld on Real Structure

Comparisons between the internal energy absorbed for the single node-to-node rigid spot-weld, and rigid and elastic mesh independent spot-weld models on the frontal longitudinal rail impact simulation are shown in Figure 5-18. The rigid mesh independent spot weld showed a higher energy absorption compared to the single node-to-node rigid spot weld and elastic spot-weld. A possible explanation is that in rigid spot weld more nodes between the two plates involved in the spot weld connection. When compared to a single node-to-node rigid connection, the rigid mesh independent spot-weld has a cluster

of nodes connected rigid. Therefore, there was stiffer connection between the plates, which leads for higher-energy absorption for the rigid mesh independent spot-weld.

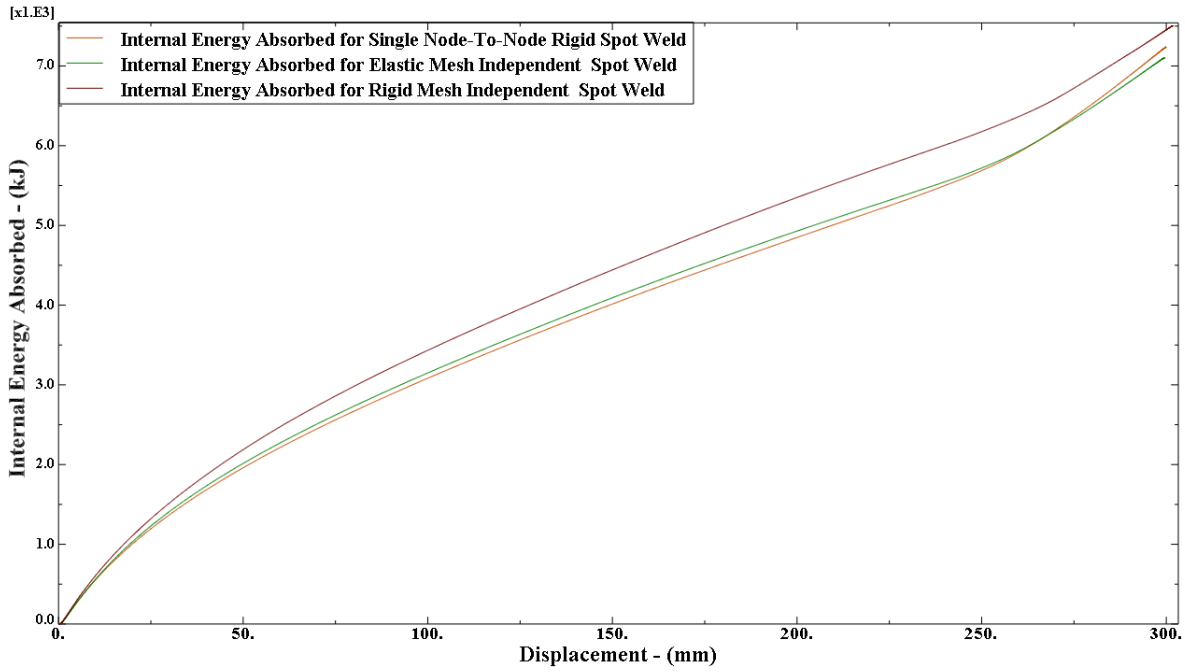


**Figure 5-18 Comparison of internal energy absorption of single node-to-node, rigid and elastic mesh independent spot weld**

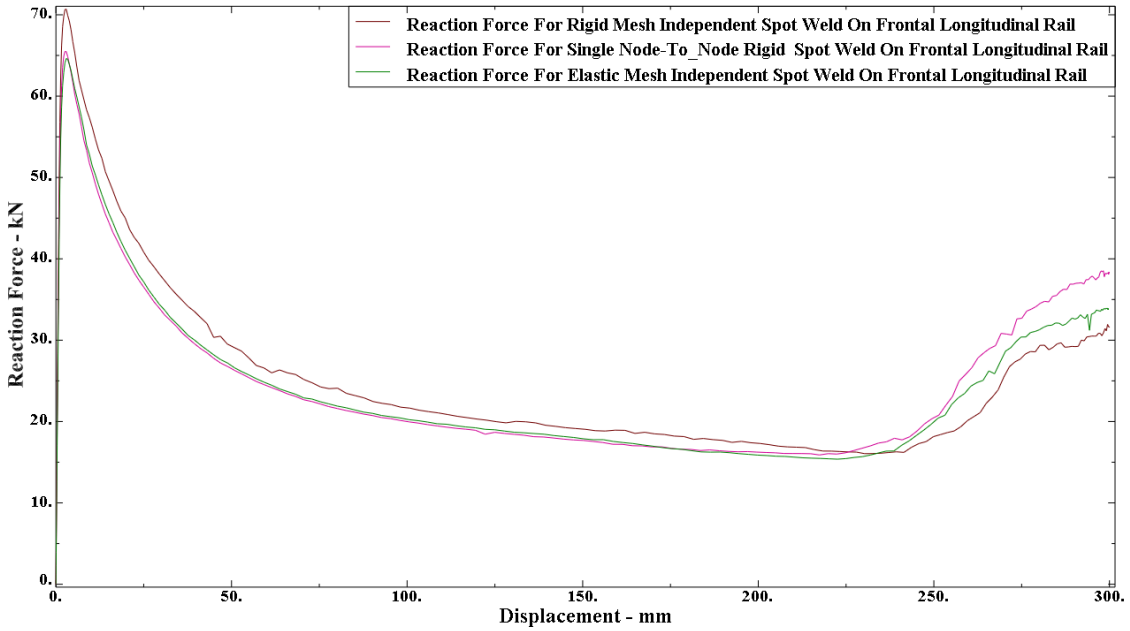


**Figure 5-19 Comparison of Reaction Force of single node-to-node, rigid and elastic mesh independent spot weld**

The elastic spot weld showed energy absorption with a similar profile of the single node-to-node rigid spot weld connections. The node-node rigid spot weld gave a 2% higher value compared to elastic spot weld at the maximum energy, which occurred at the end of the impact simulation with 300 mm displacement. In addition, at the end of the simulation event the rigid mesh independent spot weld showed 4% higher energy absorption compared to elastic mesh independent spot weld.

Figure 5-19 shows the reaction force during the impact simulation. The rigid mesh independent spot weld showed a 7.5% increase in peak force compared to the rigid node-to-node and elastic mesh-independent spot-weld models. The crush force efficiency defined as the mean force averaged over the impact event, divided by the peak

force, is lower for the rigid mesh independent spot weld. High crush force efficiency for the component would reduce the acceleration that observed by the occupants during a collision. Table 5-1 summarizes the specific internal energy defined as the internal energy divided by the component mass, the peak reaction force, and the crushing force efficiency. The rigid mesh independent spot weld has the highest specific internal energy absorbed, the highest peak force, and the lowest crushing force efficiency. The elastic mesh independent spot weld predicted the lowest energy absorption and peak force.

| **Frontal Rail** | **Specific Internal Energy (Joules/kg)** | **Peak Force ( N)** | **Crushing Force Efficiency (%)** |
|---|---|---|---|
| Single Node-To-Node Rigid Spot Weld | 1407.4 | 65476 | 45.0 |
| Rigid Mesh Independent Spot Weld | 1449.3 | 70692 | 41.2 |
| Elastic Mesh Independent Spot Weld | 1381.9 | 64523 | 43.9 |

**Table 5-1: Spot weld study result summary**

# CHAPTER SIX

## SHAPE STUDY ON FRONTAL LONGITUDINAL RAIL

The vehicle body is the frame structure on to which all the components in the vehicle are mounted. The frontal area of the structure plays an important role absorbing the impact energy especially in a frontal collision. The frontal frame structure is designed to absorb enough impact energy during the frontal collision so that the impact force transferred to the drive compartment enclosing the passenger can be reduced. This means that the front-end structure of a vehicle is the most important factor in the characteristics of frontal collision. Therefore, we need to consider the characteristics of energy absorption and the collapse by plastic deformation on frontal structures [5].

The main goal for this shape study on the longitudinal is to increase in the energy absorption and crush force efficiency of the existing longitudinal rail without a great amount of increase in the weight of the component. The shape of the bottom plate was not altered but the existing top open hat section was changed with section like semi-circle, semi-hexagon, curved top, double hat, M-shape, steps on top and sinusoidal wave entire length. The CAD model of different longitudinal rail created using the advanced surface module of the CATIA V5.

## 6.1 Base Frontal longitudinal frontal Rail

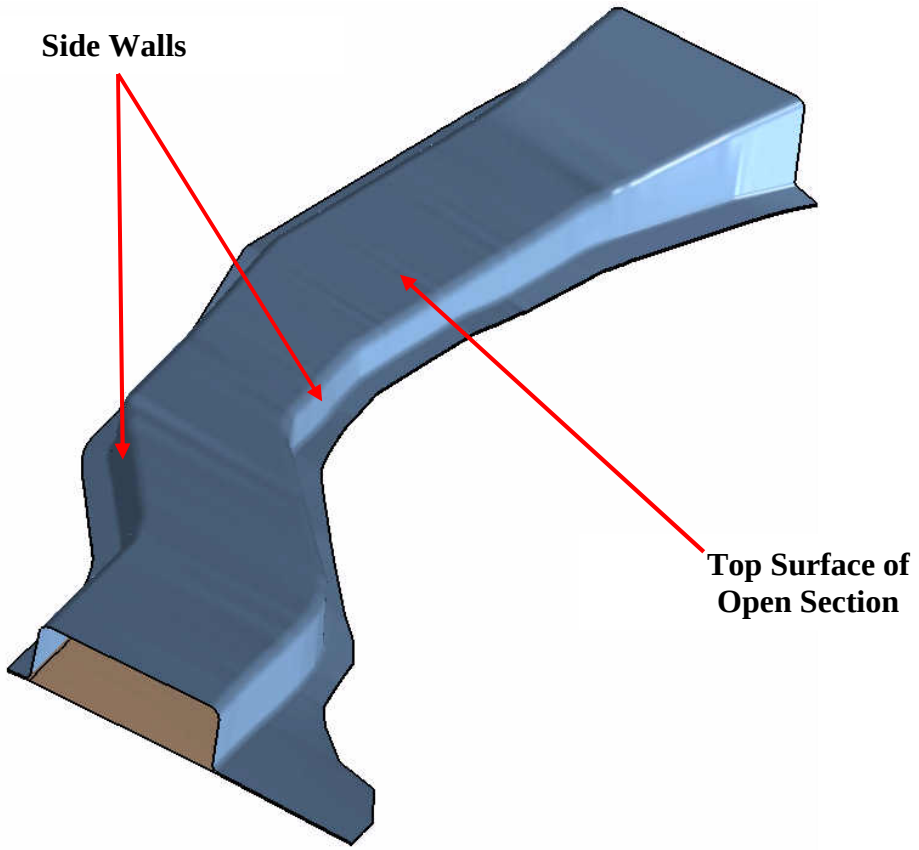


**Figure 6-1 Base shape of the Frontal longitudinal rail**

The model of the frontal longitudinal rail described in Chapter 5, considered as the base part for the shape study. The CAD model and finite element meshes for the different shapes, created in the same way as for the base part model described in Sections 5.3 and 5.4. For this study, rigid Mesh Independent spot-welds created on the both sides of the flange at an equal distance of 50 mm with the spot-weld diameter of 6mm. In order to manufacture the different shapes considered in a stamping process, the existing

bending and forming punches in the die set would need to be changed. Figure 6-2 shows the stress distribution and deformed geometry of the base shaped longitudinal rail after crushing a distance of 300 mm between two rigid walls. The energy absorption of the different shaped frontal longitudinal rail compared with the base component. Another important output monitored is the reaction force at the fixed wall. The reaction force at the fixed end wall indicates the force transferred to the driver compartment during the frontal impact. So while trying to optimize the energy absorption of the frontal rail the reaction force monitored to obtain a better understanding about dynamic crushing force. The specific energy absorption used to compare the energy absorption efficiency of the frontal longitudinal rail based on the weight. The specific energy absorption is the ratio of total energy absorbed to the weight of the component. Crushing force efficiency measures the ratio of the average crushing force over the peak crushing force. The crush force efficiency calculated, by simply dividing the mean crushing force to the peak force experienced during deformation [16, 17]. This measure is important for occupant protection, since the occupants experience all forces present during the impact. Maximizing crush force efficiency leads to greater occupant protection with the least amount of peak force being transmitted to the passenger compartment [17]. The goal of the shape optimization is to increase both the specific energy absorption and crushing force efficiency compared to the baseline frontal longitudinal rail.

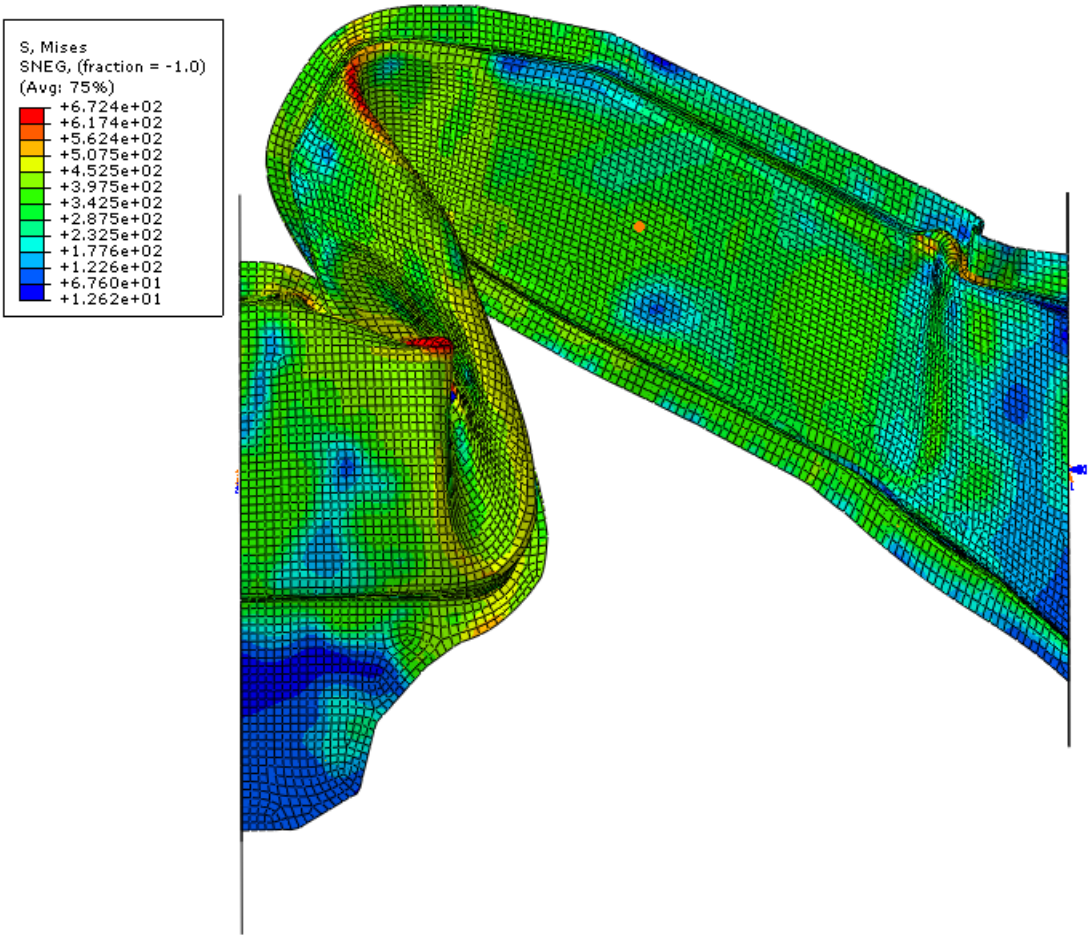


**Figure 6-2 Contours of Von-Mises Stress for crushing the base frontal rail**

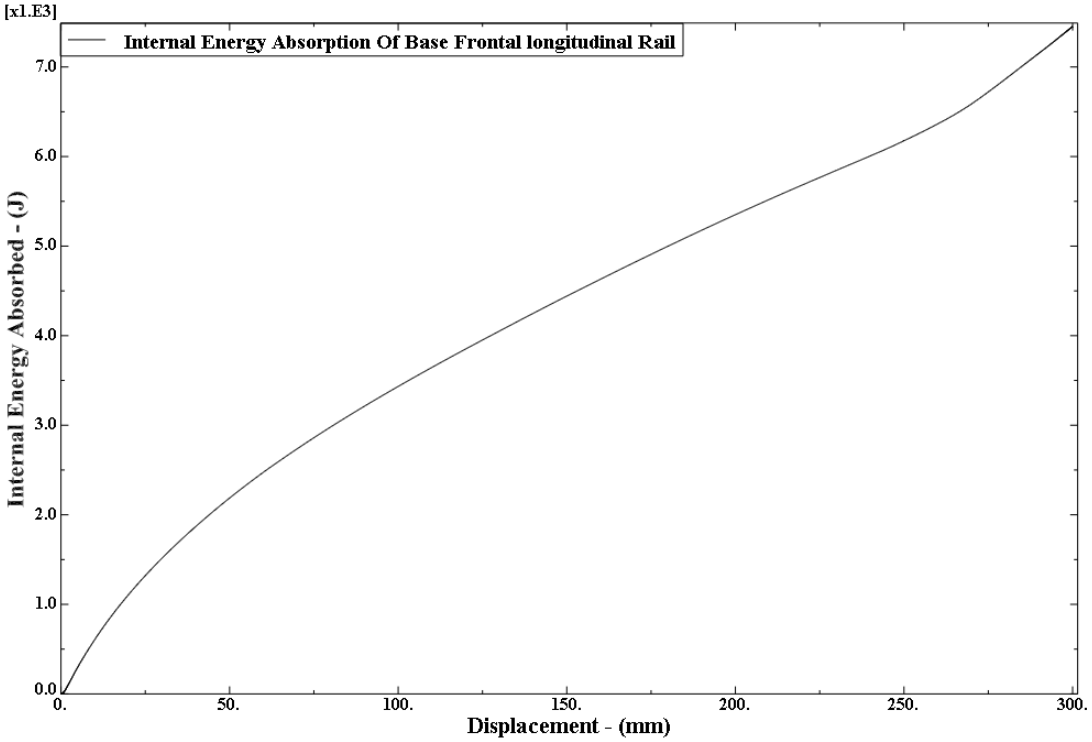


**Figure 6-3 Internal energy absorbed by the base frontal longitudinal rail**

Figure 6-3 shows the energy absorption vs. displacement curve of the base frontal longitudinal rail. The base frontal longitudinal has a mass of 5.2 kg. The shape changes in the component should increase the weight of the frontal longitudinal rail. Figure 6-4 shows the plot between reaction forces vs. displacement at the fixed rigid wall. We observe a peak force of 70.69 kN reached during the initial crushing of the longitudinal rail. The specific energy absorption for the base longitudinal rail is 1449.32 J/kg and the crush force efficiency is 41.23 %. The weights of the different shapes of longitudinal rail where kept within ± 5 % of base longitudinal rail. Because drastic increase in the

weight of the component leads to increase in the energy transferred to the driver compartment during the frontal impact.

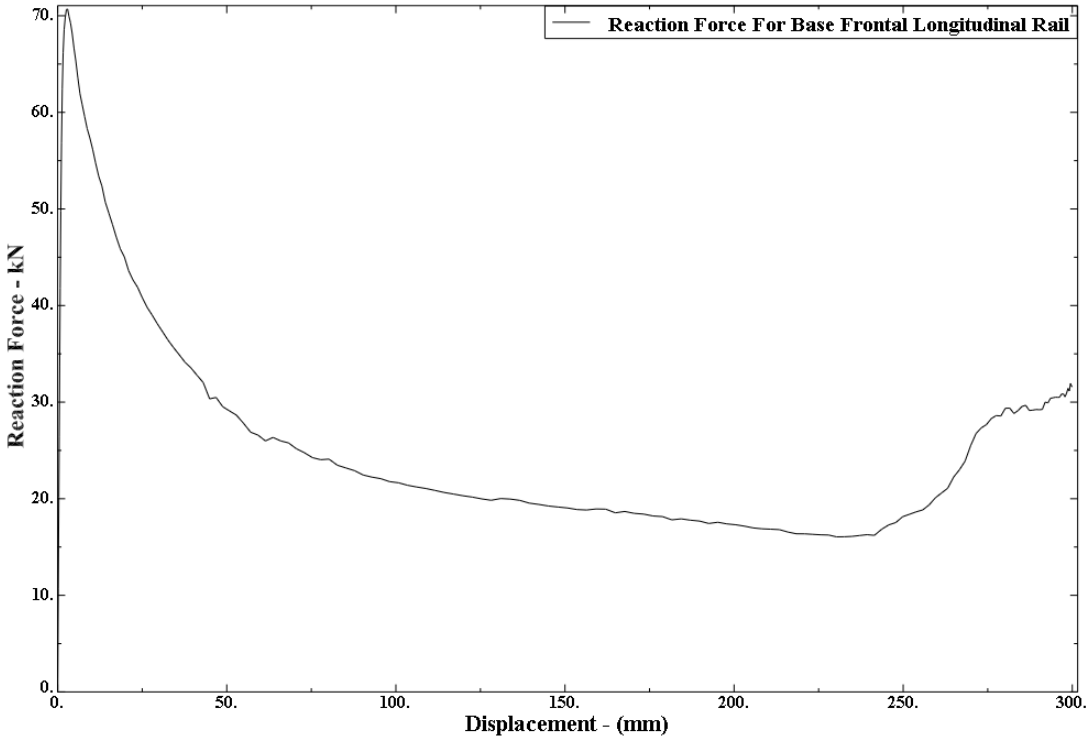


**Figure 6-4 Reaction force measured at the fixed rigid wall**

## 6.2 Semi Hexagonal Shape of Frontal Longitudinal Rail

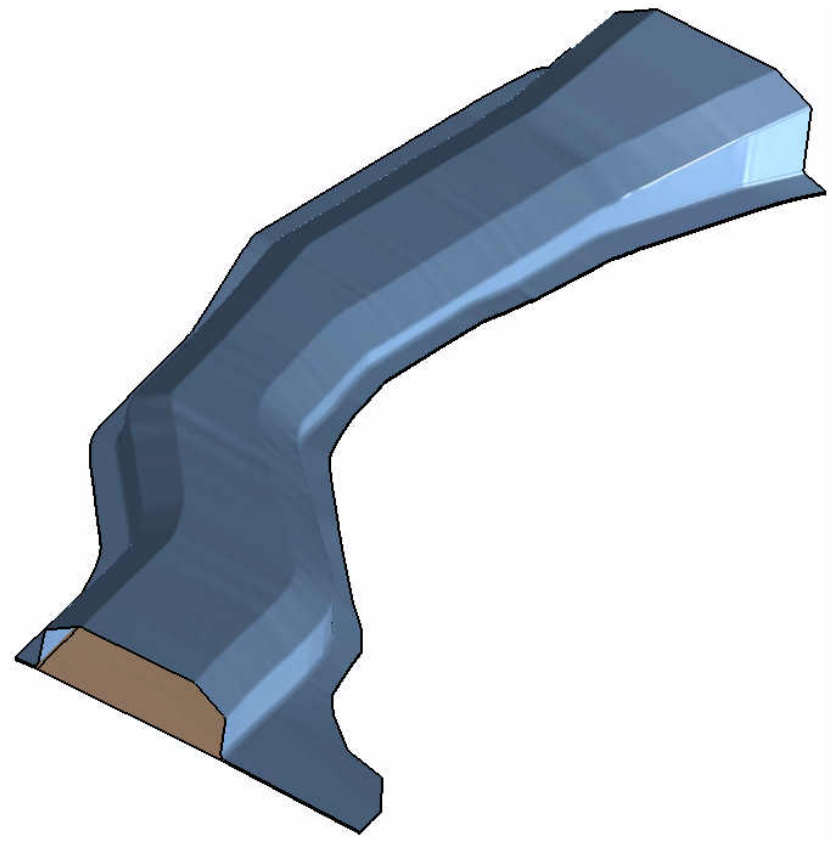

**Figure 6-5 Semi hexagonal shape of the Frontal longitudinal rail**

Figure 6-5 shows the shape change for longitudinal frontal rail with semi hexagonal cross section. The bottom plate shape is unaltered but the shape of the open hat section of the longitudinal frontal rail is changed. Instead of an open hat section, a semi hexagonal cross-section lofted along the entire length with the sidewalls unaltered. A fillet of radius 5 mm is provided at the sharp edges of the new semi hexagonal frontal longitudinal rail. The top surface of the open semi hexagonal shape longitudinal rail is similar to the top surface of base longitudinal rail. The only difference is the edges

connecting the top surface and side surface are given chamfer to create a semi hexagonal shape. The weight of the semi hexagonal shape longitudinal frontal rail is lower when compared to the base component. A rigid mesh independent spot weld of diameter 6mm is created on both the sides of the flange at an equal spacing of 50 mm. To manufacture the stamped hemi hexagonal shape frontal longitudinal rail there would be only a few design changes with one more workstation added to the existing progressive die.

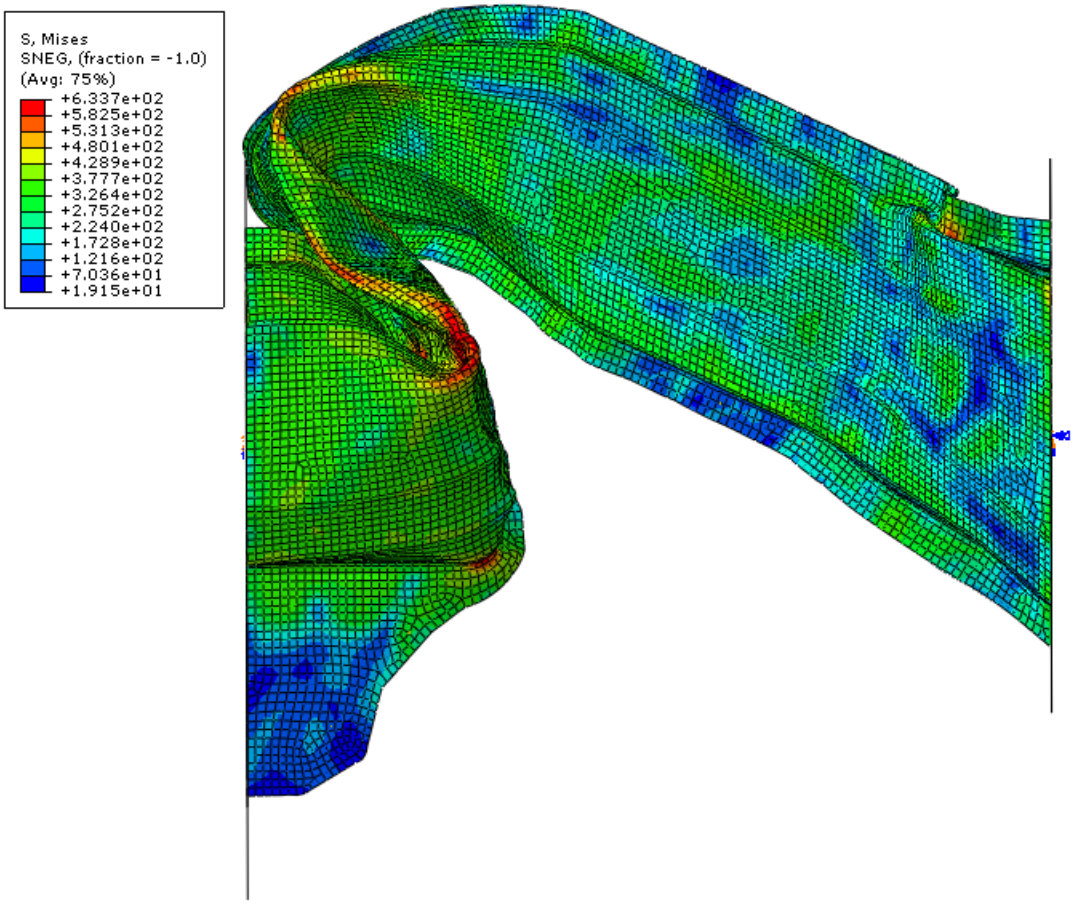


**Figure 6-6 Contours of Von-Mises Stress for crushing the semi hexagonal shape frontal longitudinal rail**

Figure 6-6 shows the Von-mises stress distribution and the mode of deformation for the semi hexagonal shape frontal longitudinal rail. The base and the hexagonal shaped longitudinal rail crushed to a distance of 300 mm for a time of 200 ms but the mode of deformation between two shapes are different. The hexagonal frontal longitudinal rail showed lesser resistance to the crush load when compared with the base rail, because when the deformation between the two component are compared the intrusion on top area of semi hexagonal shape longitudinal rail is more when compared to the base longitudinal rail.

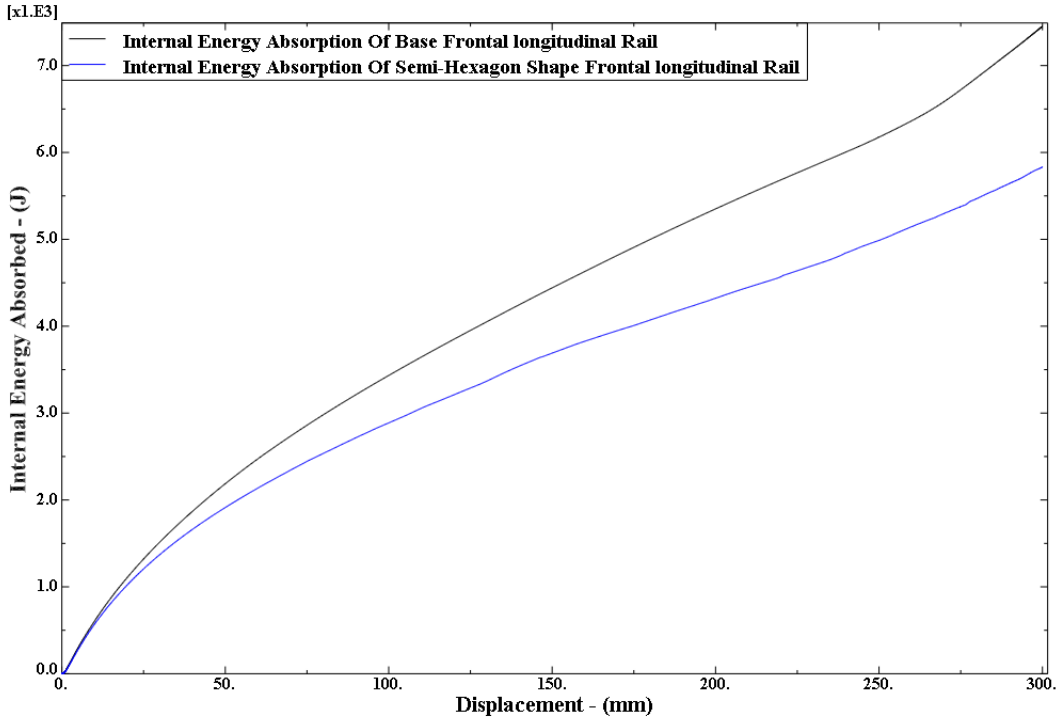


**Figure 6-7 Comparison internal energy absorbed by the base and semi hexagonal shaped frontal longitudinal rail**

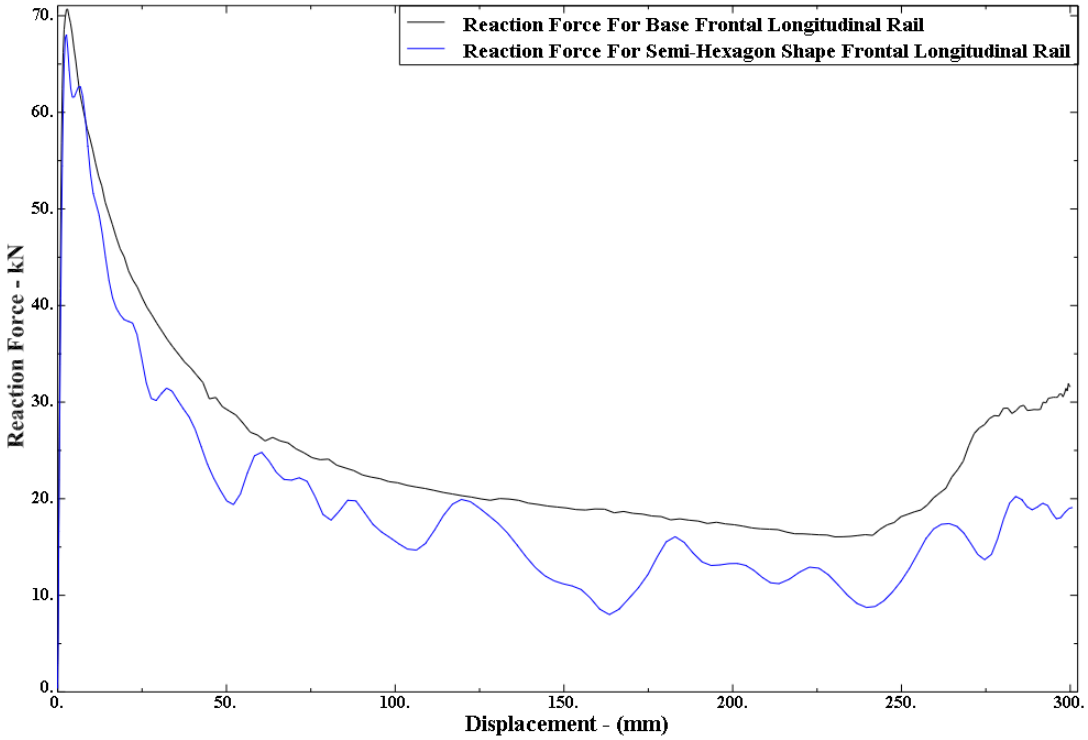


**Figure 6-8 Reaction force for semi hexagonal longitudinal rail at the fixed rigid wall**

Figure 6-7 shows the comparison for internal energy absorption of both base and hexagon frontal longitudinal rail. The base frontal longitudinal rail reached a peak value of 7.45 kJ Energy absorption while the hexagonal shape reached a value of 5.83 kJ is about 21 % lesser energy absorption compared to the base frontal longitudinal rail. The weight of the semi hexagonal shape is 4.9 kg, which is lesser than the base frontal longitudinal rail. Figure 6-8 shows the comparison of reaction force between the base and semi hexagonal frontal longitudinal rail. A peak force of 68.0 kN is reached during the initial crushing of the longitudinal rail. The specific energy absorption for base longitudinal rail is 1188.1 J/kg and the crush force efficiency is 34.74 %. Even though the

weight of the component is lesser compared to the base longitudinal rail, the energy absorption and crush force efficiency is very less.

### 6.3 Semi Circular Shape of Frontal Longitudinal Rail

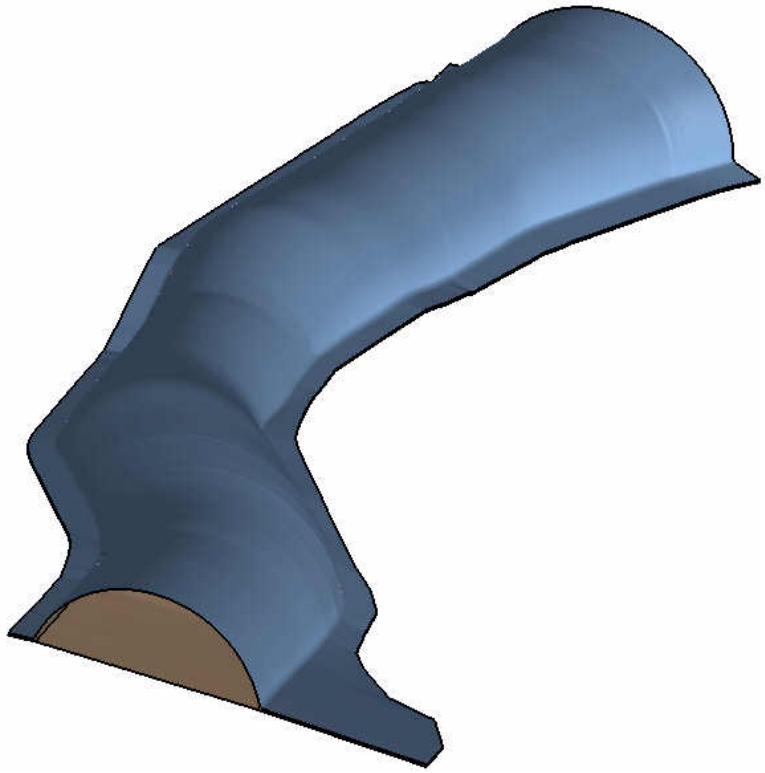

**Figure 6-9 Semi circle shape of the Frontal longitudinal rail**

Figure 6-9 shows the shape change for longitudinal frontal rail for a semi circular hat section. The bottom plate shape is unaltered but the shape of the open hat section of the longitudinal frontal rail is changed. Instead of an open hat section, a semi circle cross-section is lofted along the entire length. For this semi-circle shape sidewall are removed from the base component. A fillet of radius 5 mm is provided at the sharp edges of the

new semi circular frontal longitudinal rail. A rigid mesh independent spot weld of diameter 6mm is created on both the sides of the flange at an equal spacing of 50 mm. The base and the semi circle shaped longitudinal rail are crushed to a distance of 300 mm for a time of 200 ms. Figure 6-10 shows the von misses stress distribution and mode of deformation of the semi circular shaped frontal longitudinal rail. In case of semi-circular shape even at the rear end showed some low bending mode collapse. This collapse mode not observed in of a base frontal longitudinal rail.

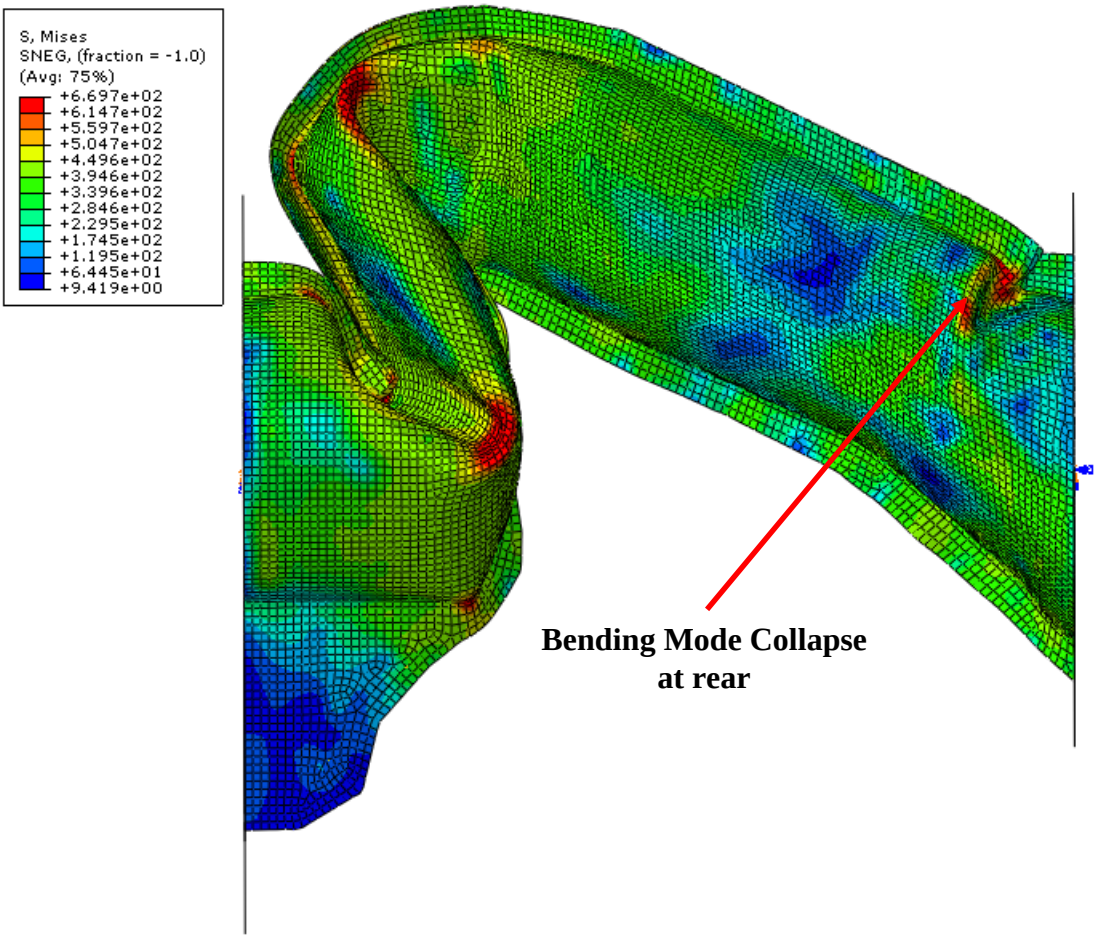


**Figure 6-10 Contours of Von-Mises Stress for crushing the semi circle shape frontal longitudinal rail**

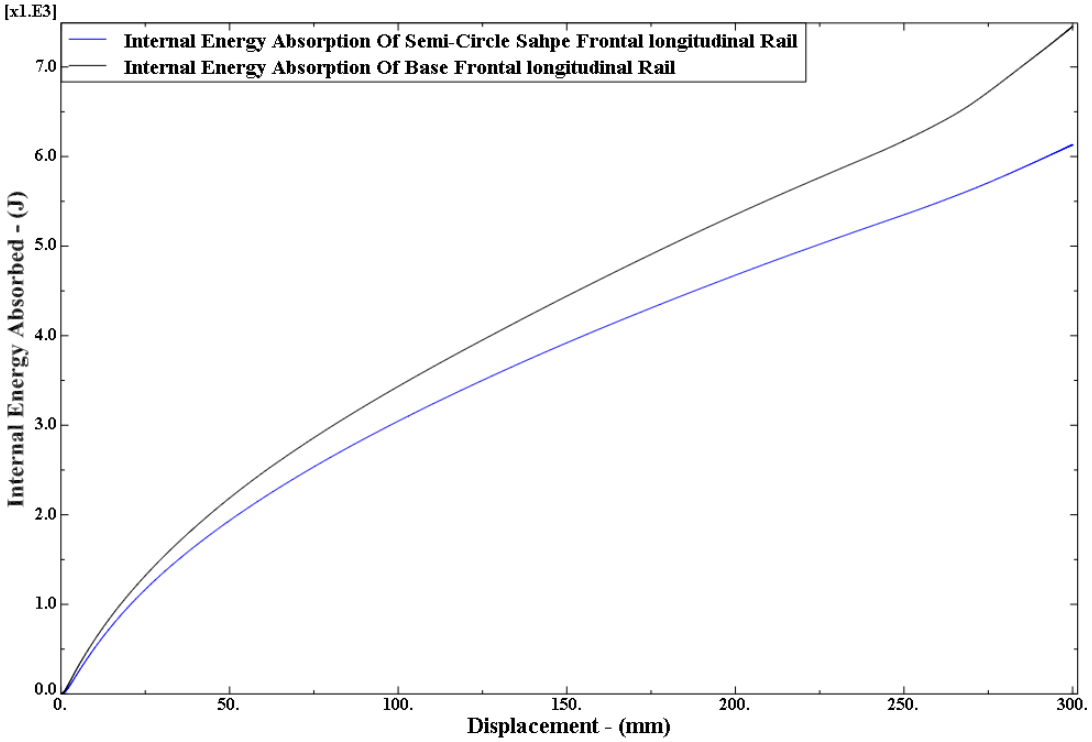


**Figure 6-11 Comparison internal energy absorbed by the base and semi circular frontal longitudinal rail**

Figure 6-11 shows the comparison for internal energy absorption of both base and semi circle frontal longitudinal rail. The base frontal longitudinal rail reached a maximum value of 7449.5 Joule Energy absorption while the semi circle shape reached a value of 6129.1 Joules is about 17 % lesser energy absorption compared to the base frontal longitudinal rail. The weight of the semi circle shape is 4.9 kg, which is lesser than the base frontal longitudinal rail. The weight of the semi circle and semi hexagonal longitudinal rail is same, but the energy absorption of semi circle frontal longitudinal rail is higher when compared to semi hexagon frontal longitudinal rail.

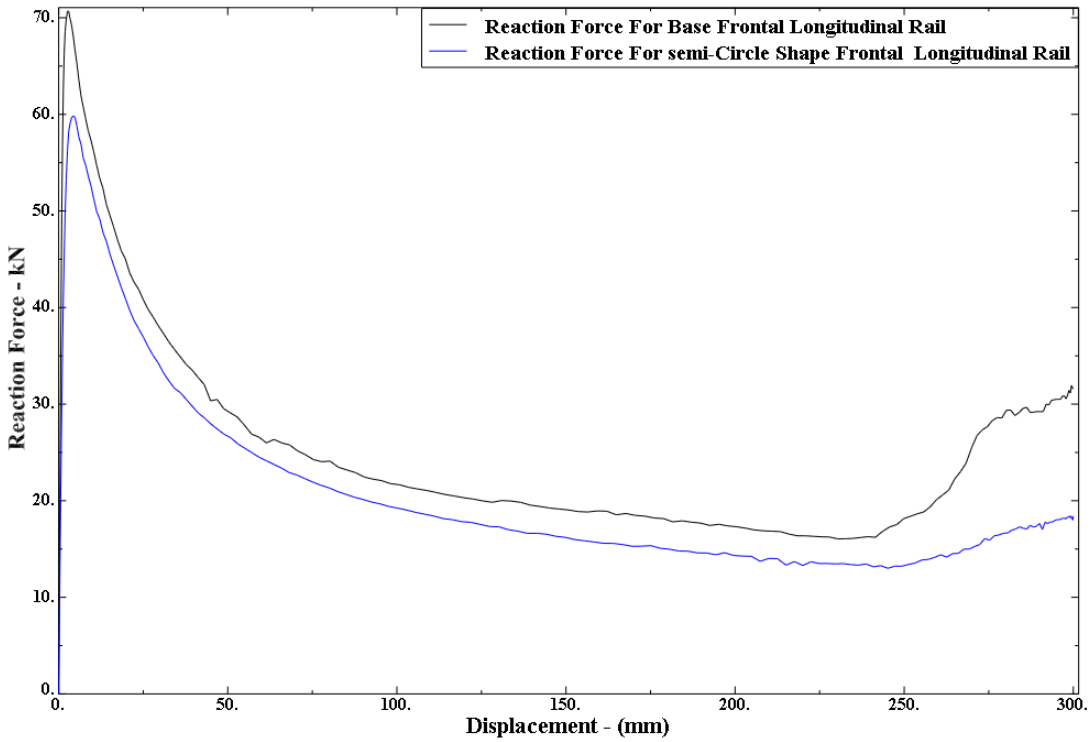


**Figure 6-12 Reaction force for semi circle longitudinal rail at the fixed rigid wall**

Figure 6-12 shows the dynamic mean crushing force vs. displacement plot for the semi circle frontal longitudinal rail. A peak force of 59714.1 N is reached during the initial crushing of the longitudinal rail. The specific energy absorption for semi circle shaped frontal longitudinal rail is 1245.741 J/Kg and the crush force efficiency is 38.24 %. The weight of the component is lesser compared to the base longitudinal rail. However, the energy absorption and crushing force efficiency is very less for semi circle longitudinal frontal rail. To manufacture semi circular shape frontal longitudinal rail there will be need to change the forming die. The profile of the die would be altered

completely into a semi circular shape. When compared to the semi hexagonal shape longitudinal rail this has showed 7% higher energy absorption.

## 6.4 Curved Top Shape of Frontal Longitudinal Rail

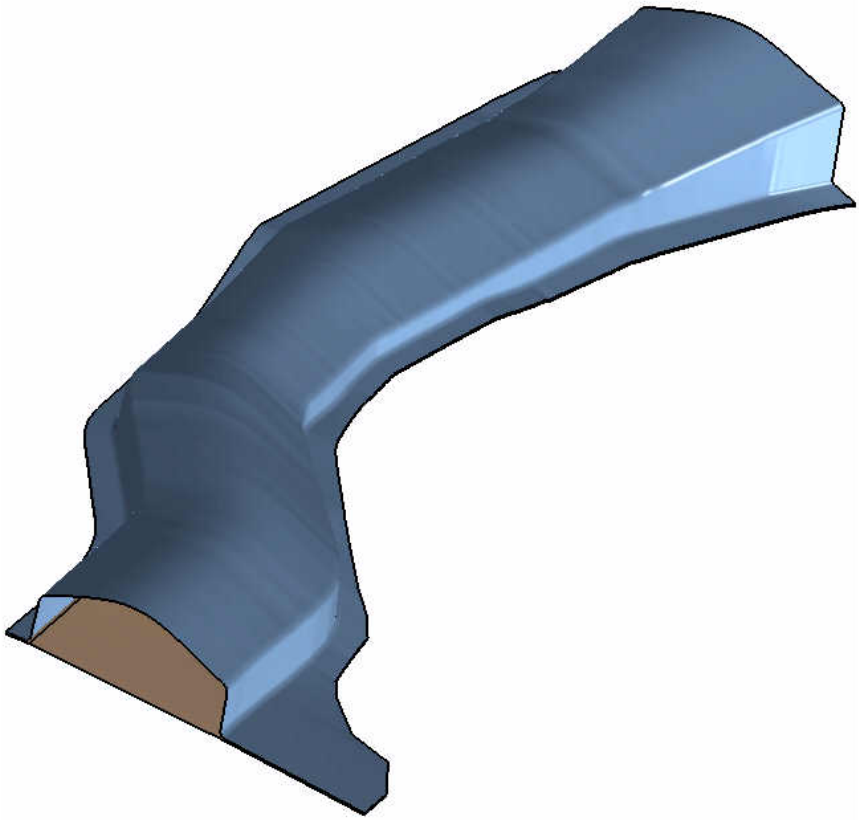

**Figure 6-13 Curved shape of the Frontal longitudinal rail**

Figure 6-13 shows curved shape change on the longitudinal frontal rail. Bottom plate shape is unaltered while the open hat section of the longitudinal frontal rail is changes into curved shape keeping the side surfaces as guide. Instead of open hat section, a curve shape cross-section lofted along the entire length. A fillet of radius 5 mm

provided at the sharp edges of the new curved frontal longitudinal rail. In creating the CAD model of the curved shape longitudinal frontal rail, the top surface of the open hat section in Figure 6-1 is constrained has the limiting surface for creating the top curve of the curved shape frontal longitudinal rail. A rigid mesh independent spot weld of diameter 6mm created on both the sides of the flange at an equal spacing of 50 mm. The curve shaped longitudinal rail crushed to a distance of 300 mm for a time of 200 ms. Figure 6-14 shows the von misses stress distribution of the curve shape rail.

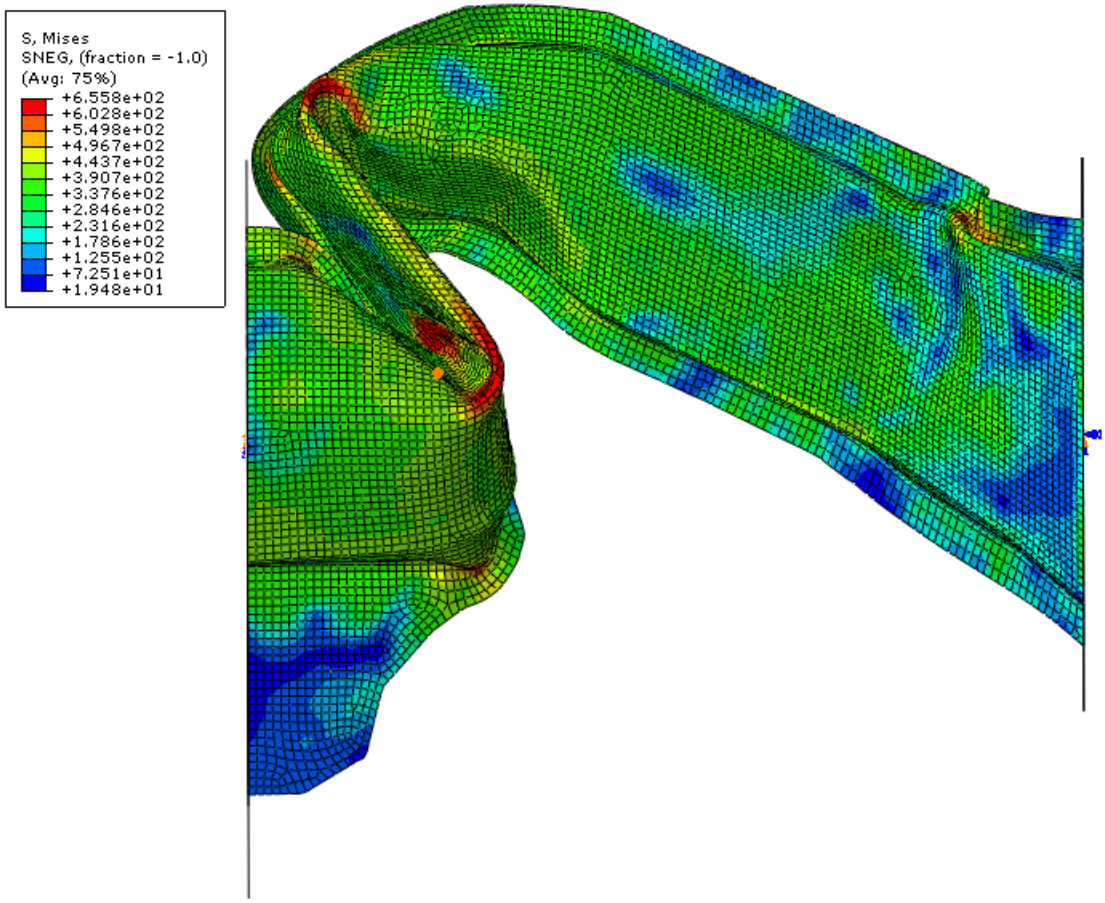


**Figure 6-14 Contours of Von-Mises Stress for crushing the curved shape frontal longitudinal rail**

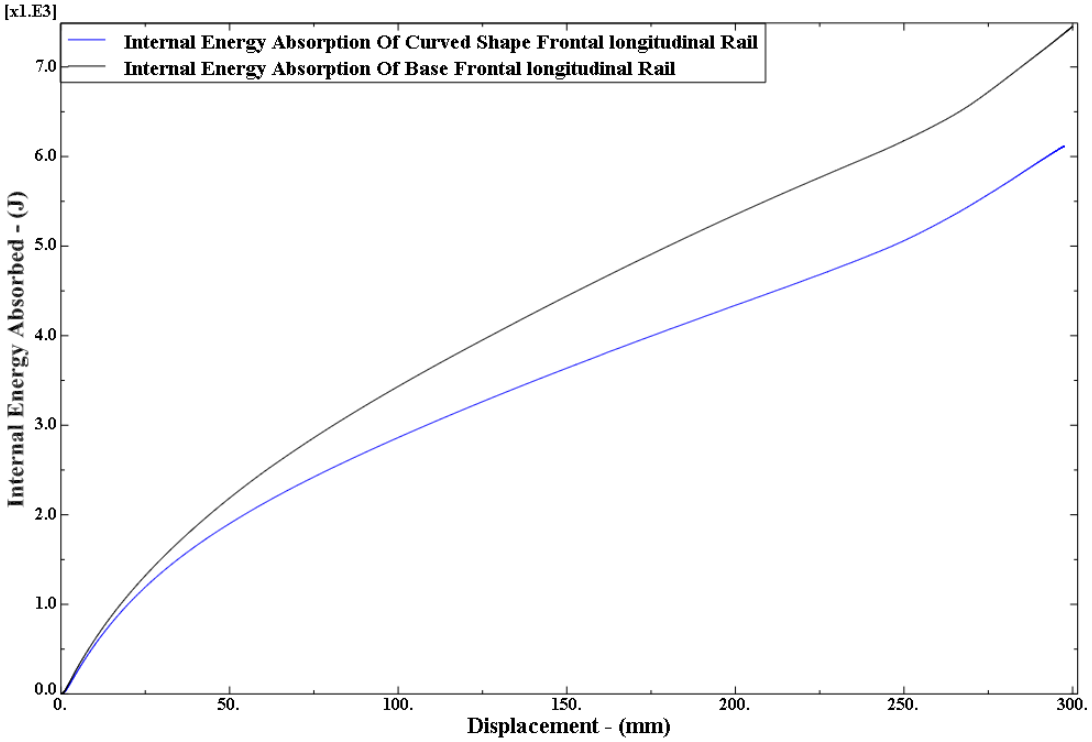


**Figure 6-15 Comparison internal energy absorbed by the base and semi hexagonal shaped frontal longitudinal rail**

The Figure 6-15 shows the comparison for internal energy absorption of both base and curved shape frontal longitudinal rail. The base frontal longitudinal rail reached a peak value of 7449.5 Joule Energy absorption while the curved shape reached a value of 6114.49 Joules is about 17 % lesser energy absorption compared to the base frontal longitudinal rail. The weight of the curved shape frontal longitudinal rail is 5.0 Kg, which is lesser than the base frontal longitudinal rail. The Figure 6-16 shows the dynamic mean crushing force vs. displacement plot for the semi circle frontal longitudinal rail. A peak force of 65664 N reached during the initial crushing of the longitudinal rail. The specific

energy absorption for curved shape frontal longitudinal rail is 1222.89 J/Kg and the crush force efficiency is 36.97 %. Even though the weight of the component is lesser compared to the base longitudinal rail the energy absorption and crush force efficiency is very less for curved shape longitudinal frontal rail.

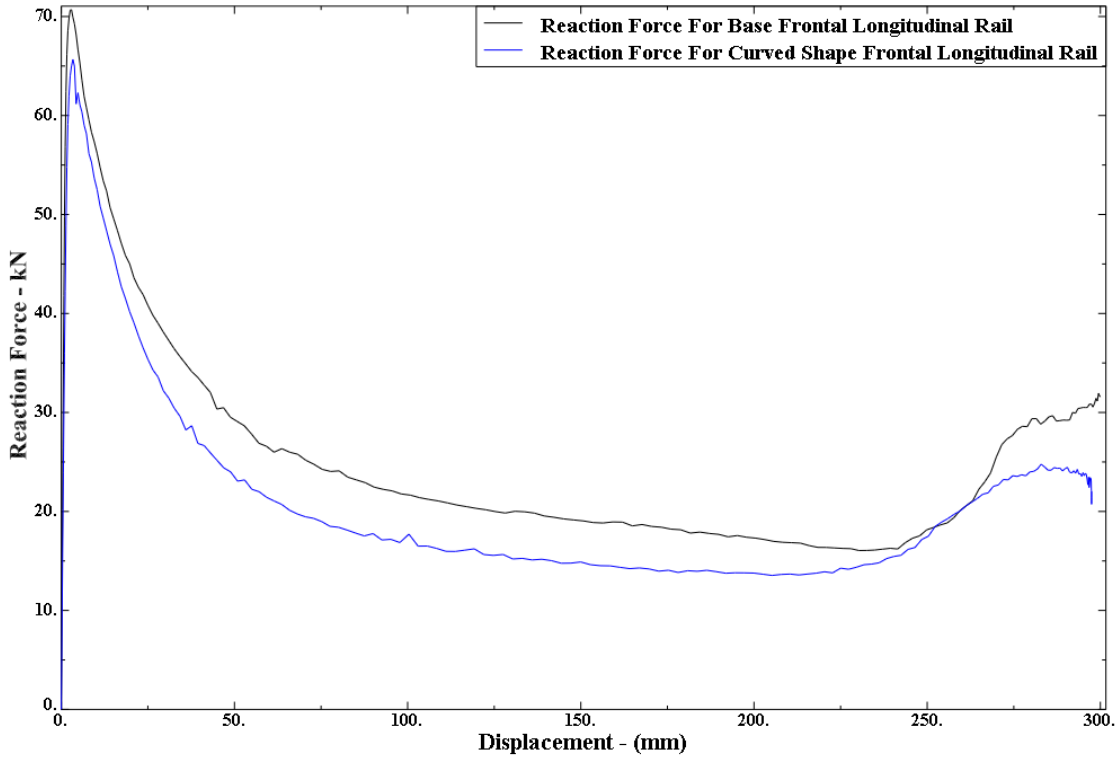


**Figure 6-16 Reaction force for curved shape longitudinal rail at the fixed rigid wall**

## 6.5 M-Shape of Frontal Longitudinal Rail

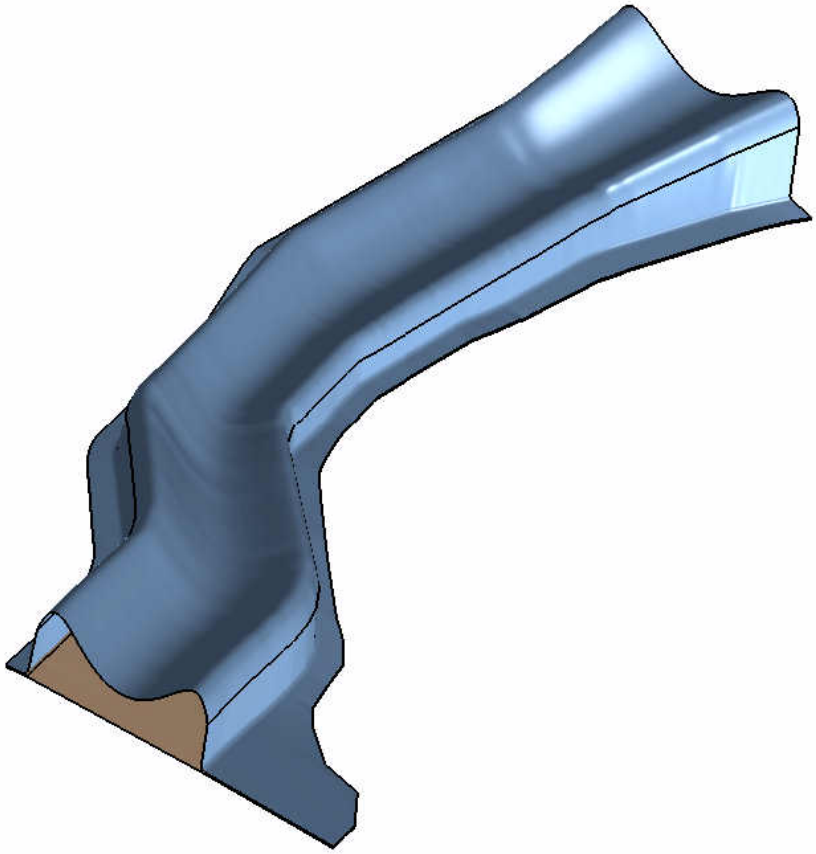

**Figure 6-17 M-shape of the Frontal longitudinal rail**

Figure 6-17 shows the M-shape section for the longitudinal frontal rail. The bottom plate shape is unaltered, while the open hat section of the longitudinal frontal rail is changes into M-shape keeping the side surfaces as is. A profile of M-shape is created with a circle with large radius and two circles with tangency to the middle circle. By trimming, the circle with the side surface of the base longitudinal frontal rail and loft the M-shape cross section along the length. A fillet of radius 5 mm is provided at the sharp

edges of the new M-shaped frontal longitudinal rail. The weight of the M-shape is 5.8 kg, which is higher than the base frontal longitudinal rail.

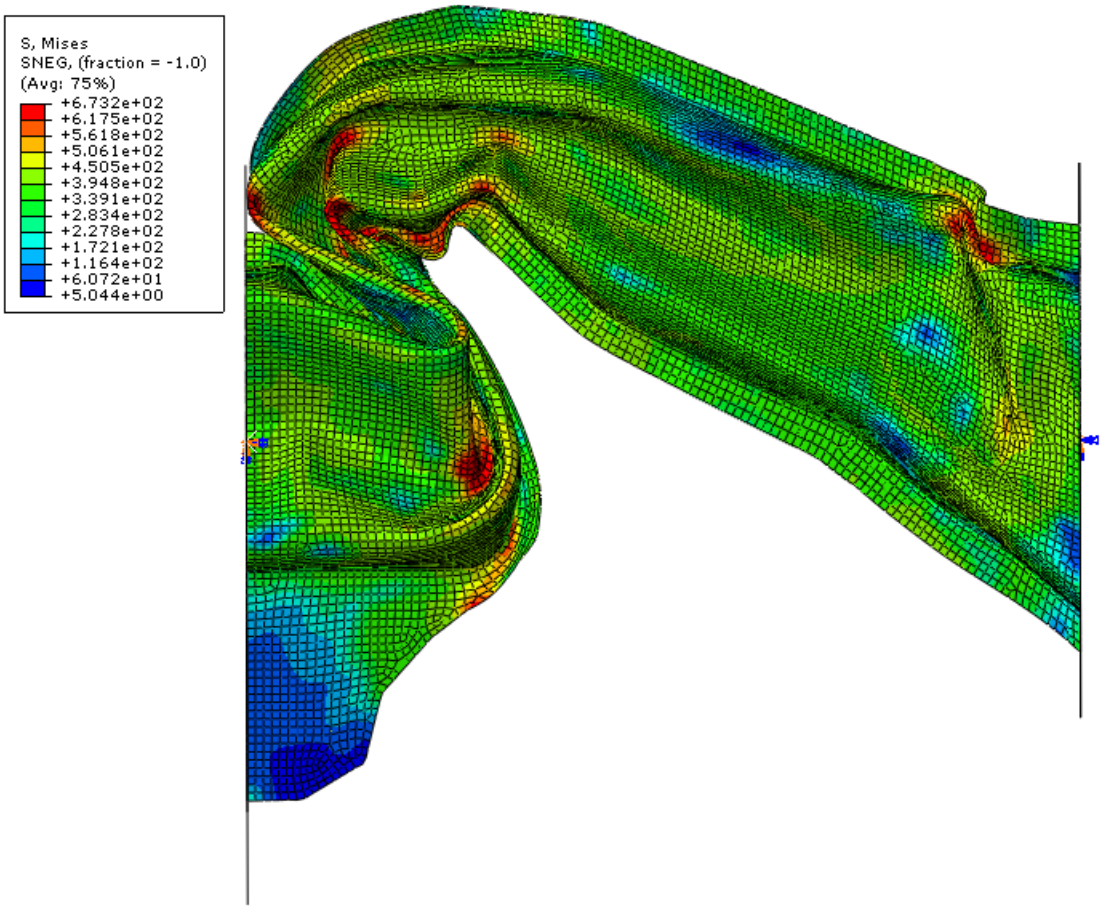


**Figure 6-18 Contours of Von-Mises Stress for crushing the M-shape frontal longitudinal rail**

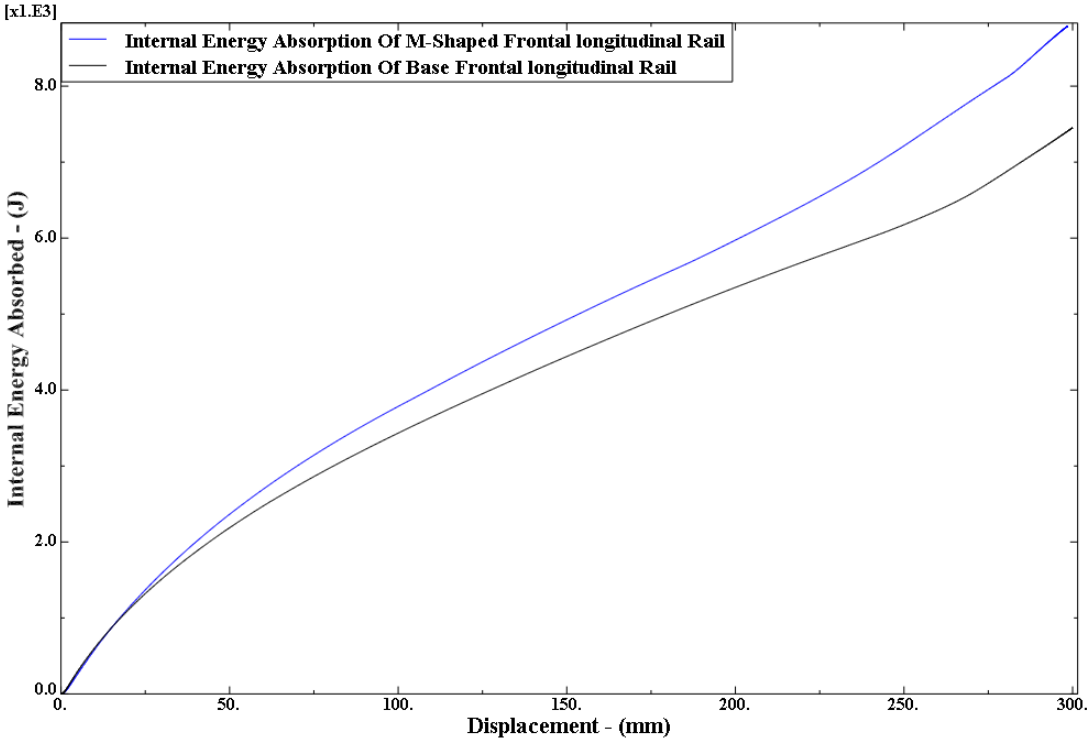


**Figure 6-19 Comparison internal energy absorbed by the base and M-shaped frontal longitudinal rail**

A rigid mesh independent spot weld of diameter 6mm is created on both the sides of the flange at an equal spacing of 50 mm. The M-shaped longitudinal rail crushed to a distance of 300 mm for a time of 200 ms. Figure 6-18 shows the Von-Mises stress distribution and mode of deformation of the M-shape frontal longitudinal rail. From the deformed configuration, it is clear that more regions of the rail have crumpled during the impact simulation. Figure 6-19 shows the comparison for internal energy absorption of the base and M-shape frontal longitudinal rail components. The base frontal longitudinal rail reached a maximum value of 7449.5 Joule Energy absorption while the M-shape

reached a value of 8785.15 Joules; about 17 % higher energy absorption compared to the base frontal longitudinal rail. Figure 6-20 shows the dynamic mean crushing force vs. displacement plot for the M-shaped frontal longitudinal rail. A peak force of 66257.4 N is reached during the initial crushing of the longitudinal rail. The specific energy absorption for the base longitudinal rail is 1514.68 J/Kg and the crush force efficiency is 50.3 %. The M-shape longitudinal rail showed an increase of 9 % in crush efficiency. The main problem with this shape is manufacturability; there should be a lot of design in bending punches to obtain the final stamped M-shape; also, the non-flat top surface makes mounting components more difficult.

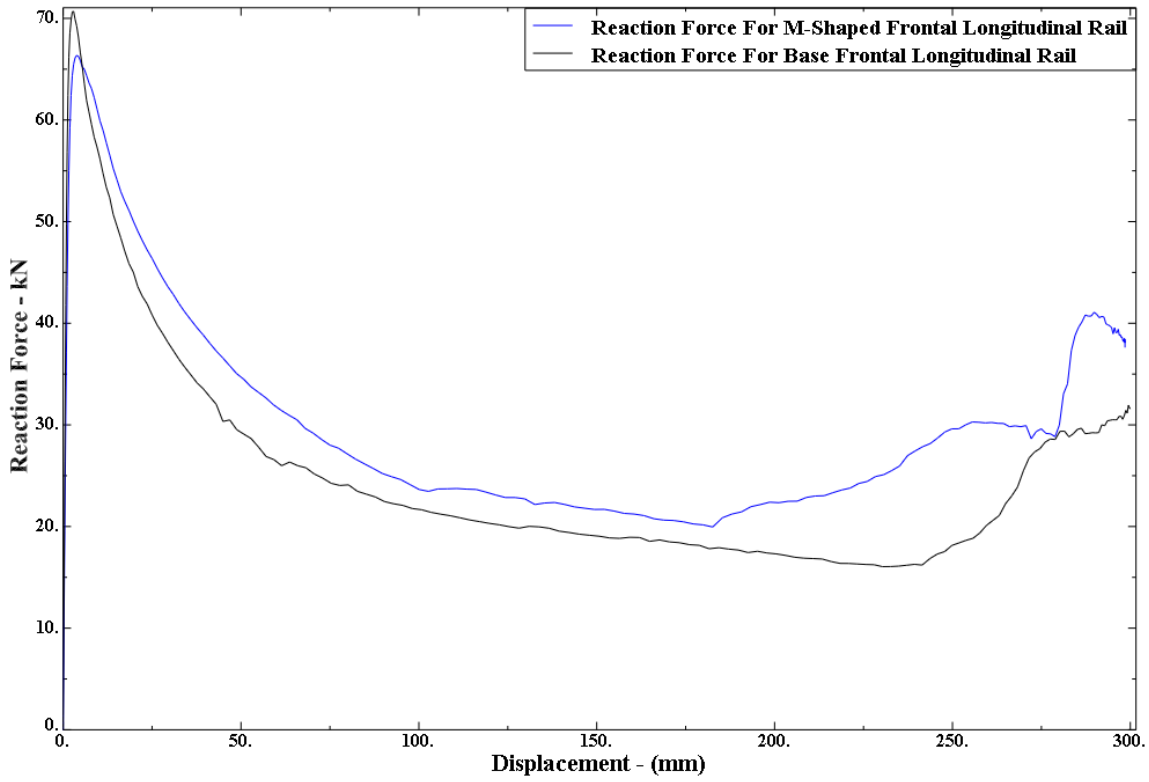


**Figure 6-20 Reaction force measured measure for M-shaped longitudinal rail at the fixed rigid wall**

## 6.6 Double Hat Shape of Frontal Longitudinal Rail

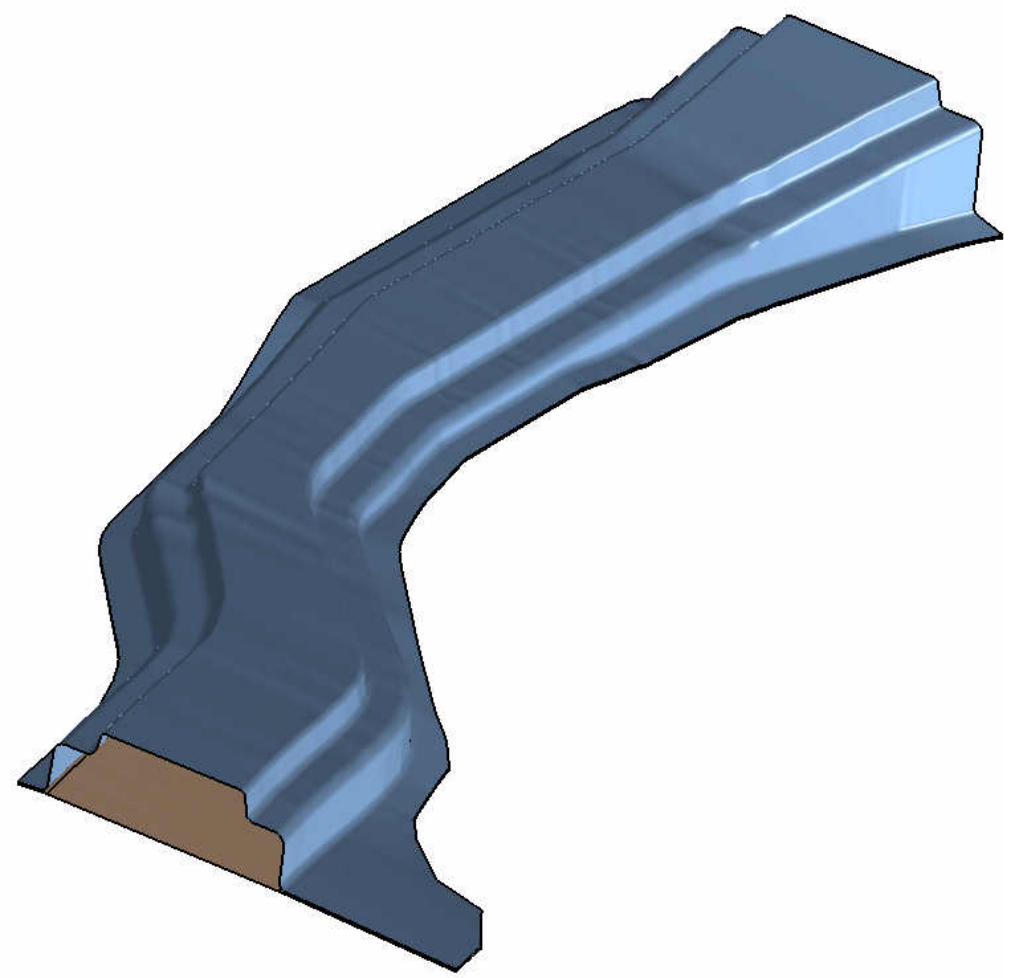

**Figure 6-21 Double hat shaped of the Frontal longitudinal rail**

Figure 6-21 shows Double-Hat shape change on the longitudinal frontal rail. The bottom plate is kept unchanged, while the open hat section of the longitudinal frontal rail is changes into double hat shape keeping the side surfaces as is. A fillet of radius 5 mm is provided at the sharp edges of the new Double-Hat shape frontal longitudinal rail. The

creation of double hat shape frontal longitudinal rail involved in creating a cross section with one step in sides and having the top surface of the base frontal longitudinal rail has the limiting line in creating the top surface of double hat cross section. Once the cross section is created it is lofted along the length of the longitudinal rail with the side surface has guide. The weight of the Double hat shape is 5.03 kg, which is lesser than the base frontal longitudinal rail.

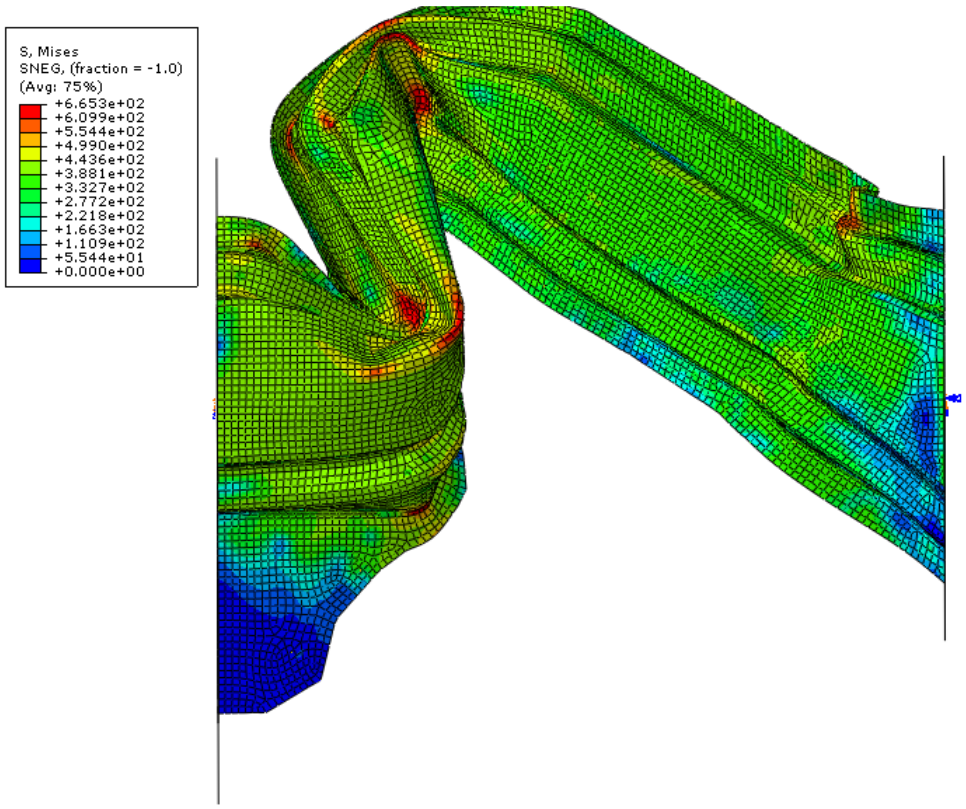


**Figure 6-22 Contours of Von-Mises Stress for crushing the double-hat shaped frontal longitudinal rail**

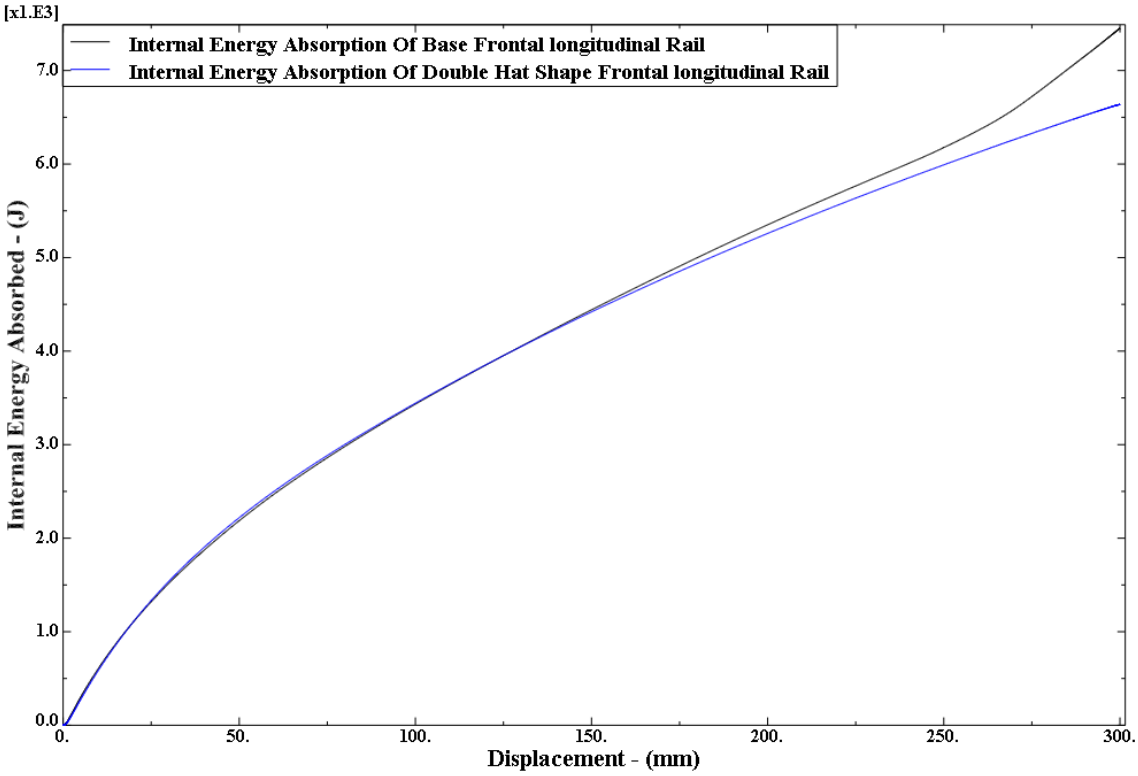


**Figure 6-23 Comparison internal energy absorbed by the base and double hat shaped frontal longitudinal rail**

A rigid mesh independent spot weld of diameter 6mm is created on both the sides of the flange at an equal spacing of 50 mm. The double hat shape longitudinal rail crushed to a distance of 300 mm for a time of 200 ms. Figure 6-22 shows the Von-Mises stress distribution and mode of deformation of the double hat frontal longitudinal rail. Figure 6-23 shows the comparison for internal energy absorption of the base and double hat shape frontal longitudinal rails. The base frontal longitudinal rail reached a maximum value of 7449.5 Joule Energy absorption while the double hat shape reached a value of 6636.49 Joules is about 13 % lesser energy absorption compared to the base frontal

longitudinal rail. The interesting observation on the internal energy absorption curves between both base and double hat shape frontal longitudinal rail is both followed a same path until the displacement reached 150mm, after that the energy absorption of double hat reduced. Figure 6-24 shows the dynamic mean crushing force vs. displacement plot for the M-shaped frontal longitudinal rail. A peak force of 68910.5 N is reached during the initial crushing of the longitudinal rail. The specific energy absorption for the base longitudinal rail is 1327.29 J/Kg and the crush force efficiency is 35.56 %. The double hat shape frontal longitudinal rail showed a decrease of 6 % in crush efficiency.

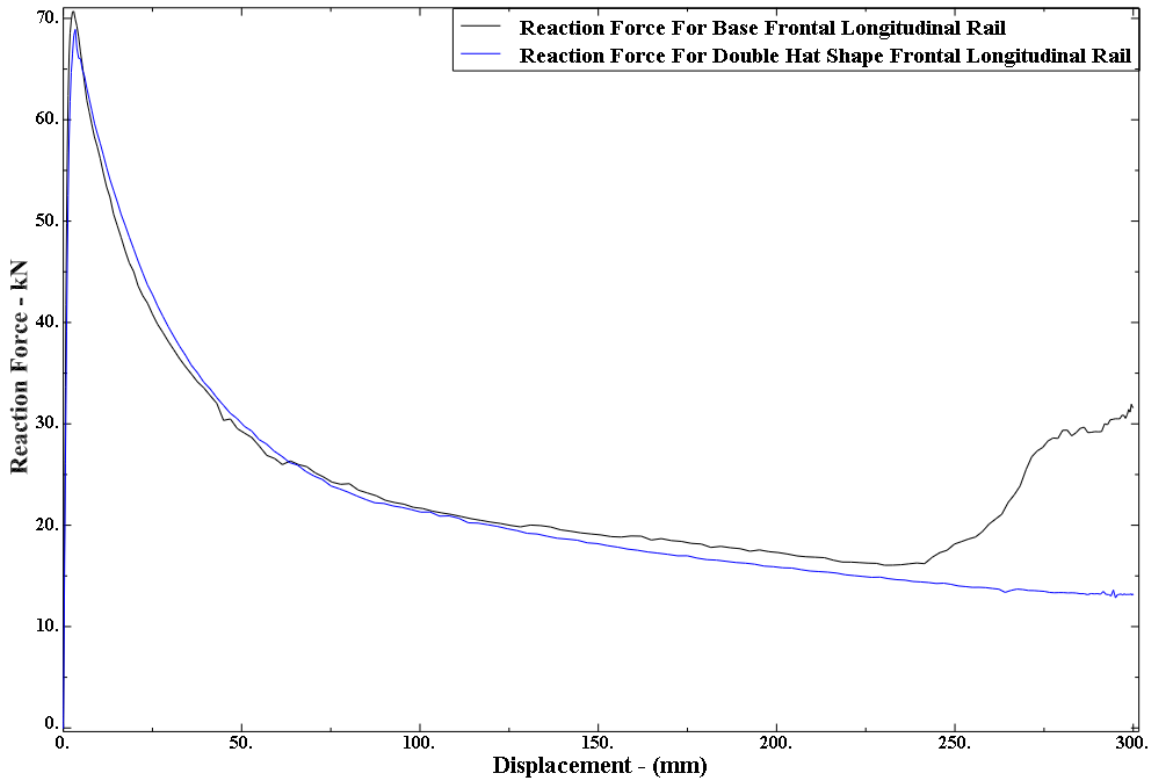


**Figure 6-24 Reaction force for double hat shaped longitudinal rail at the fixed end**

## 6.7 Top Stepped of Frontal Longitudinal Rail

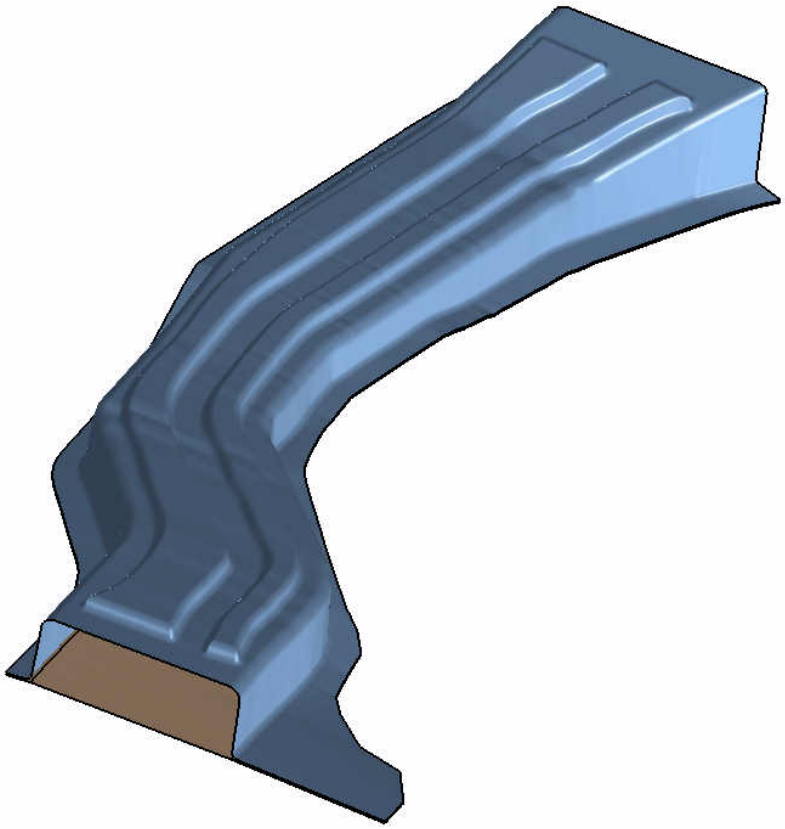

**Figure 6-25 Double hat shape of the Frontal longitudinal rail**

Figure 6-25 shows top stepped frontal longitudinal frontal rail. The bottom plate is kept unchanged, while the top surface of the open hat section of the longitudinal frontal rail is changes with two steps. These kinds of longitudinal stepped bead are also used in B-pillars of passenger cars. A fillet of radius 5 mm is provided at the sharp edges of the new top stepped shape frontal longitudinal rail. The top surface of the base frontal longitudinal rail is used to create the top steps, the top surface is offset to a distance of

8mm and then the shape of steps are drawn over the offset surface. Then the offset surface is trimmed with the sketch drawn and the edges extruded until the top surface. A rigid mesh independent spot weld of diameter 6mm is created on both the sides of the flange at an equal spacing of 50 mm. The double hat shape longitudinal rail crushed to a distance of 300 mm for a time of 200 ms. Figure 6-26 shows the von misses stress distribution and mode of deformation of the double hat frontal longitudinal rail.

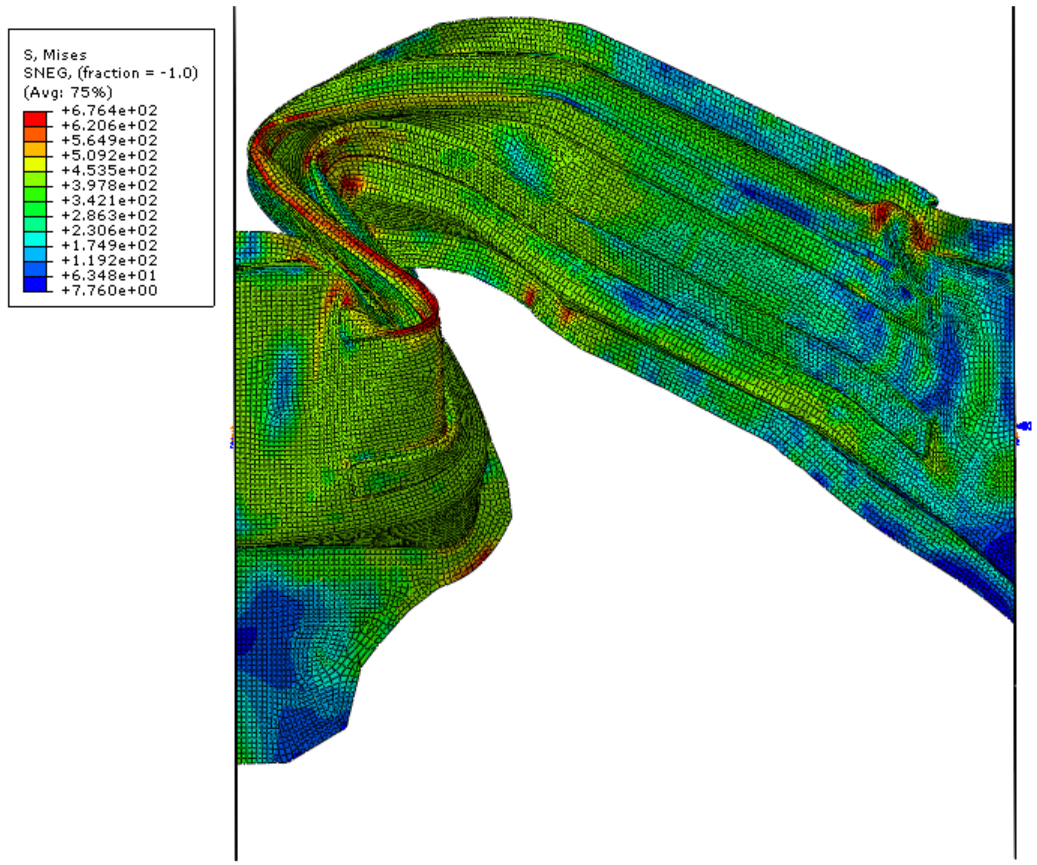


**Figure 6-26 Contours of Von-Mises Stress for crushing the top stepped shaped frontal longitudinal rail**

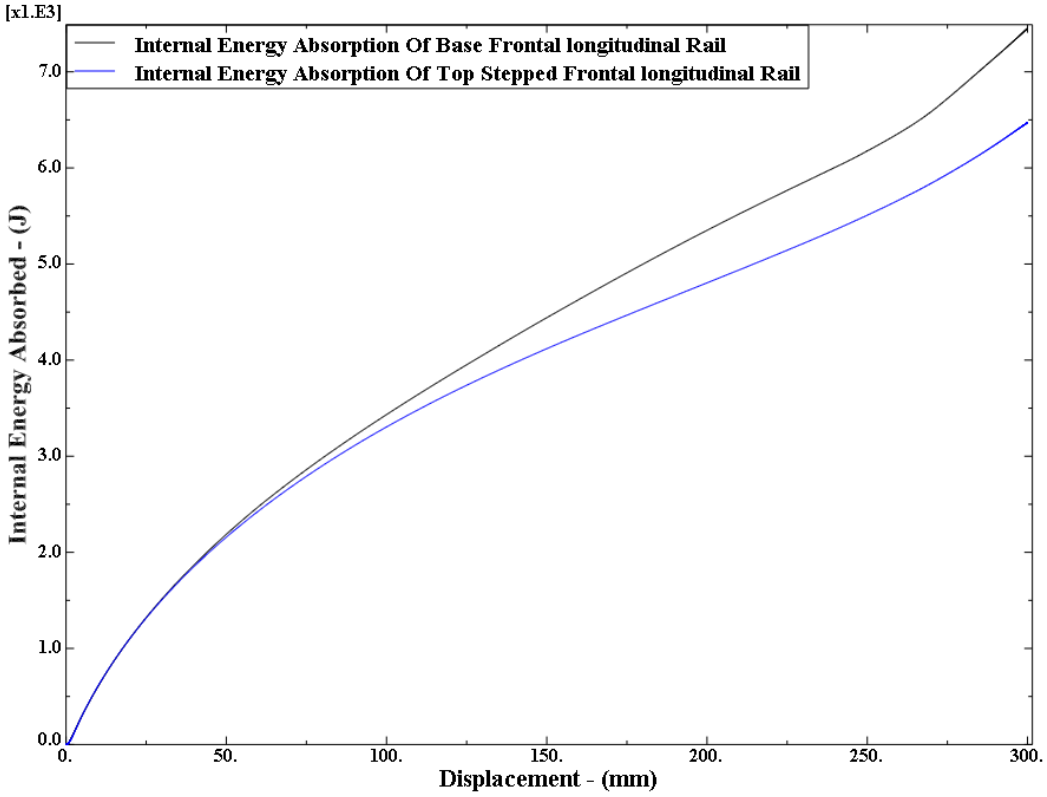


**Figure 6-27 Comparison internal energy absorbed by the base and top stepped shaped frontal longitudinal rail**

Figure 6-27 shows the comparison for internal energy absorption of both base and top stepped shape frontal longitudinal rail. The base frontal longitudinal rail reached a peak value of 7449.5 Joule Energy absorption while the top stepped shape reached a value of 6463.74 Joules is about 13% lesser energy absorption compared to the base frontal longitudinal rail.

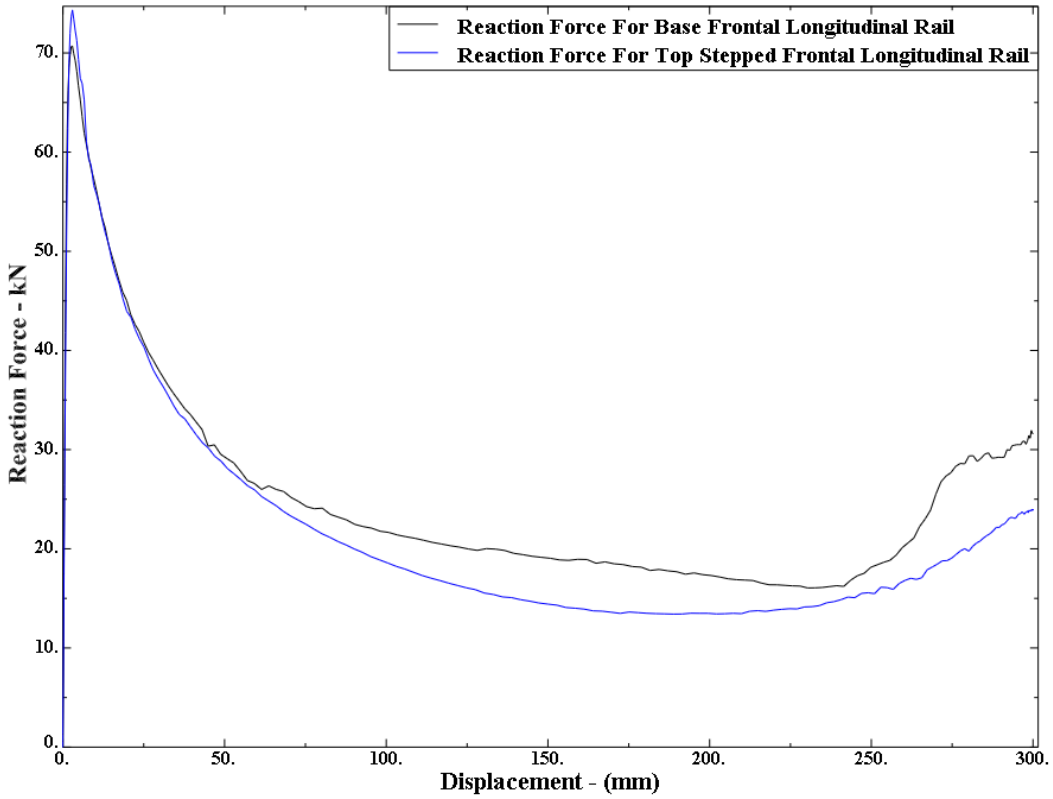


**Figure 6-28 Reaction force measured measure for top stepped shaped longitudinal rail at the fixed rigid wall**

Figure 6-28 shows the dynamic mean crushing force vs. displacement plot for the top stepped shape frontal longitudinal rail. A peak force of 7433.21 N is reached during the initial crushing of the longitudinal rail. The specific energy absorption for the base longitudinal rail is 1219.57 J/Kg and the crush force efficiency is 34.49 %. The top stepped shape longitudinal rail showed a decrease of 7 % in crush efficiency.

## 6.8 Full Wave Shape of Frontal Longitudinal Rail

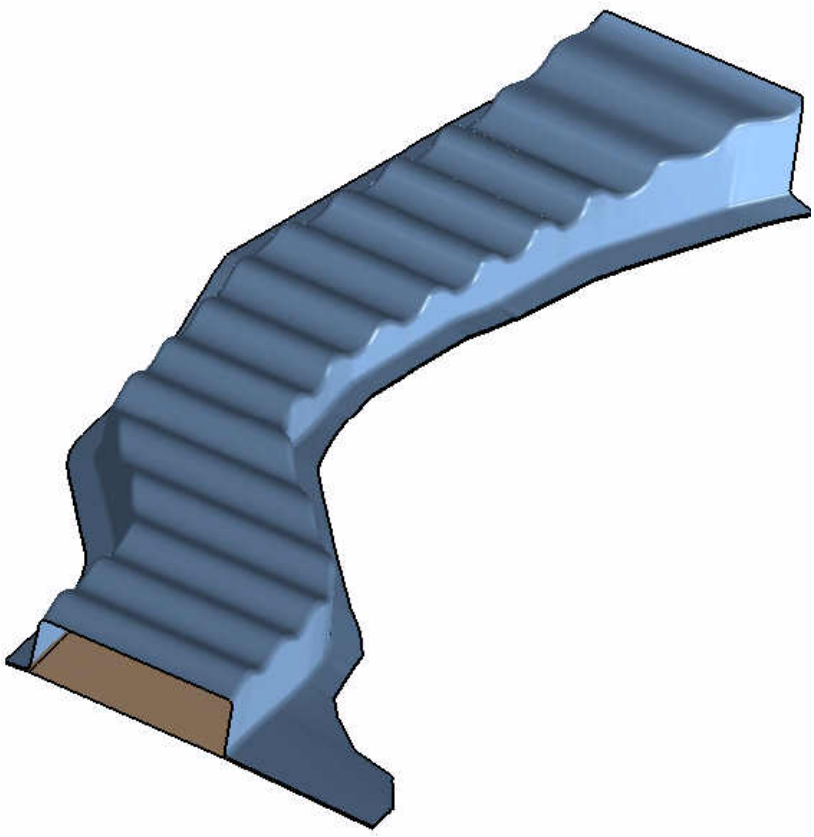

**Figure 6-29 Full wave shape of the Frontal longitudinal rail**

Figure 6-29 shows full wave shaped frontal longitudinal frontal rail. The bottom plate is kept unchanged, while the top surface of the open hat section of the longitudinal frontal rail is changed into a wave from with 15 sinusoidal waves with length of 50 mm. A fillet of radius 5 mm provided at the sharp edges of the new top stepped shape frontal longitudinal rail. There have been recent studies reported indicating that there will be increase in energy absorption with an open I-cross section and the center web having a

sinusoidal wave format [17]. Here instead of an open I-section, a sinusoidal wave has been created on the top surface of the base frontal longitudinal rail

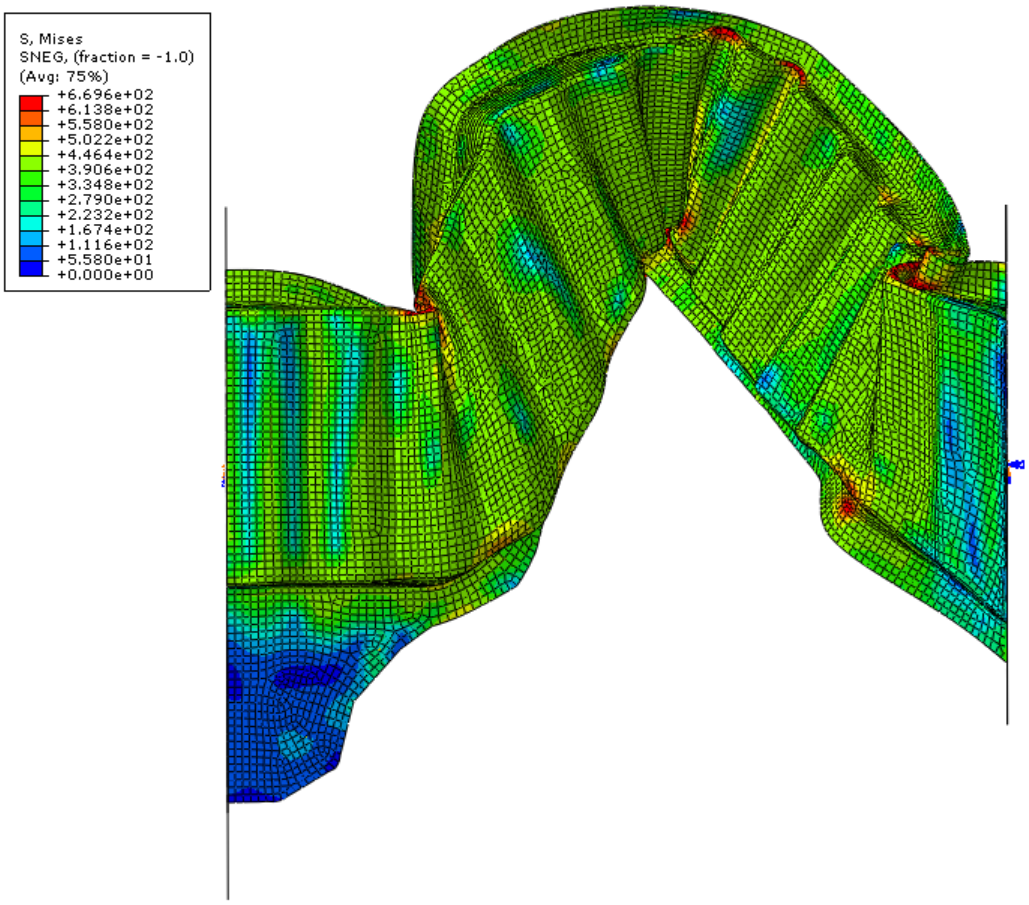


**Figure 6-30 Contours of Von-Mises Stress for crushing the full wave shaped frontal longitudinal rail**

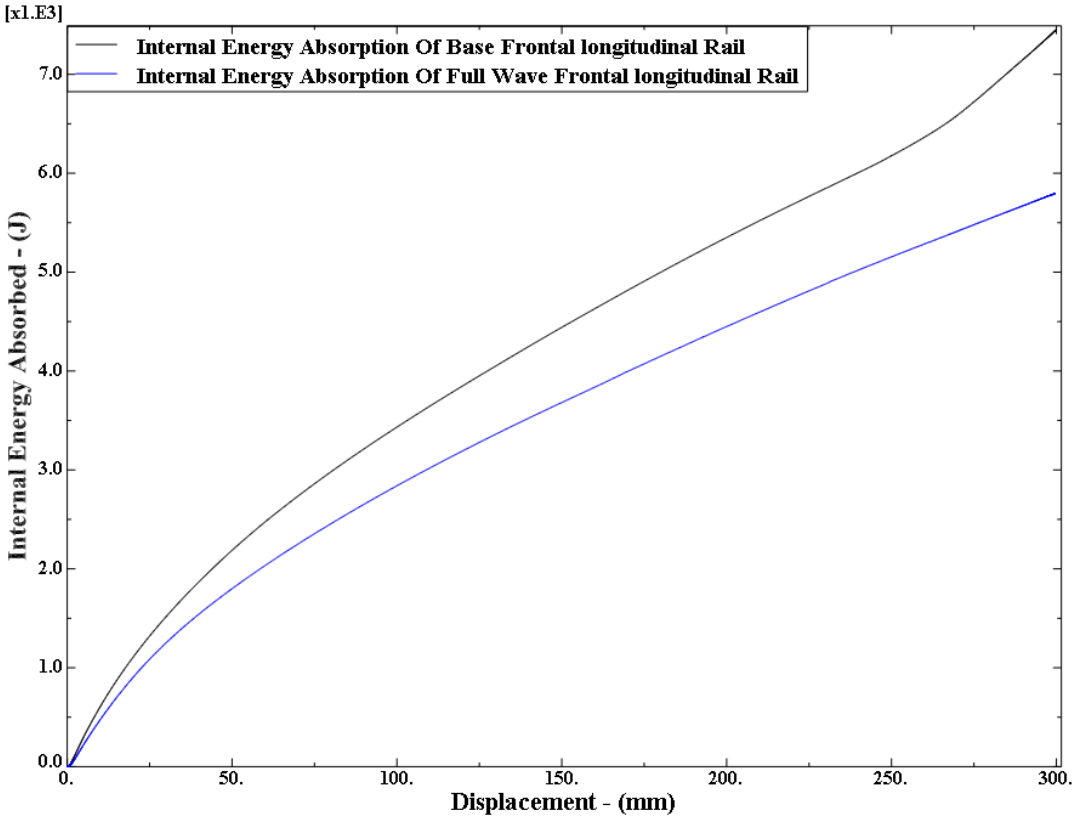


**Figure 6-31 Comparison internal energy absorbed by the base and full wave shaped frontal longitudinal rail**

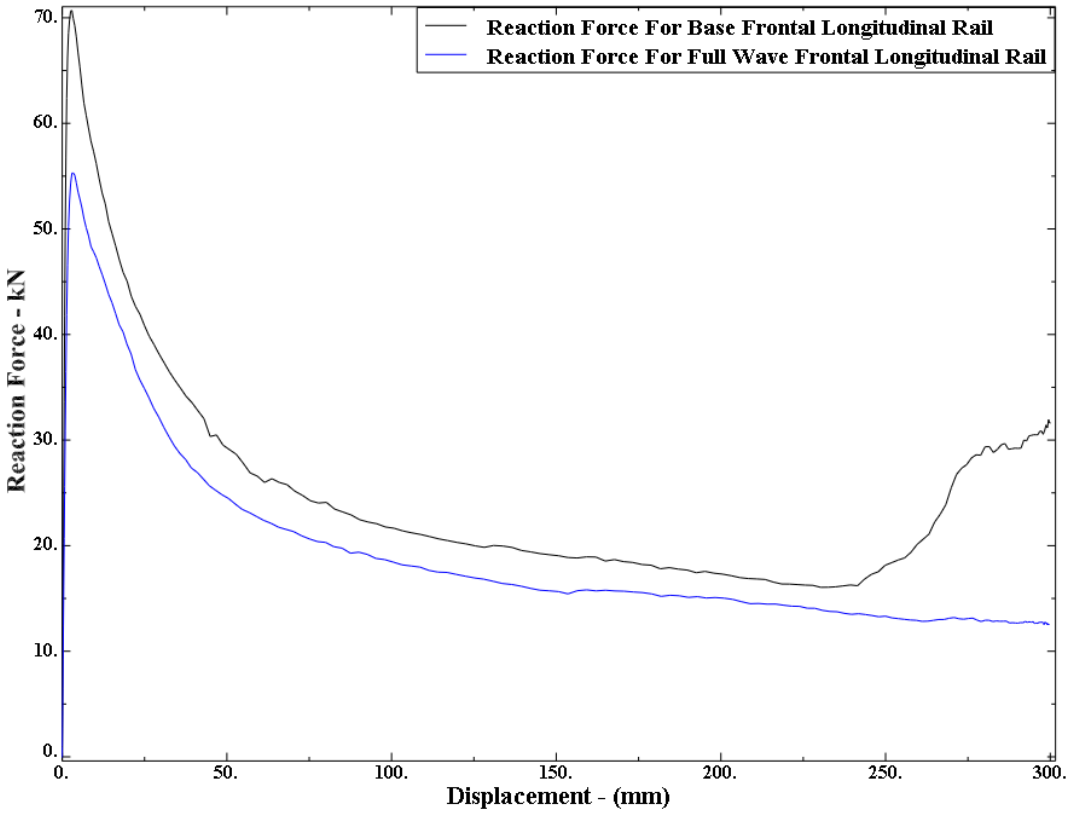


**Figure 6-32 Reaction force for full wave shaped longitudinal rail at the fixed end**

A rigid mesh independent spot weld of diameter 6mm is created on both the sides of the flange at an equal spacing of 50 mm. The full wave shape longitudinal rail crushed to a distance of 300 mm for a time of 200 ms. Figure 6-30 shows the Von-Mises stress distribution and mode of deformation of the full wave shaped frontal longitudinal rail. Figure 6-31 shows the comparison for internal energy absorption of both base and full wave shape frontal longitudinal rail. The base frontal longitudinal rail reached a maximum value of 7449.5 Joule Energy absorption while the double hat shape reached a value of 5788.13 Joules resulting in about 22 % lesser energy absorption compared to the

base frontal longitudinal rail. An important observation for this shape are the mode of deformation shown in Figure 6-30; the component crush occurred more globally in longitudinal movement compared to local axial crush in the initial bend region of the base rail. The wave shape also caused the rail to twist as it deformed. This deformation behavior did not occur for the other shapes. The wave shape structure showed a high resistance to the crushing over the entire length of the component indicating a stiff component which does not absorb much energy and has low crush force efficiency.

Figure 6-32 shows the dynamic mean crushing force vs. displacement plot for the full wave-shaped frontal longitudinal rail. A peak force of 55287 N is reached during the initial crushing of the longitudinal rail. The specific energy absorption for full wave longitudinal rail is 1087.994 J/Kg and the crush force efficiency is 37.24 %. The full-length sinusoidal wave longitudinal rail showed a decrease of 7 % in crush efficiency.

## 6.9 Partial Frontal Wave Shape of Frontal Longitudinal Rail

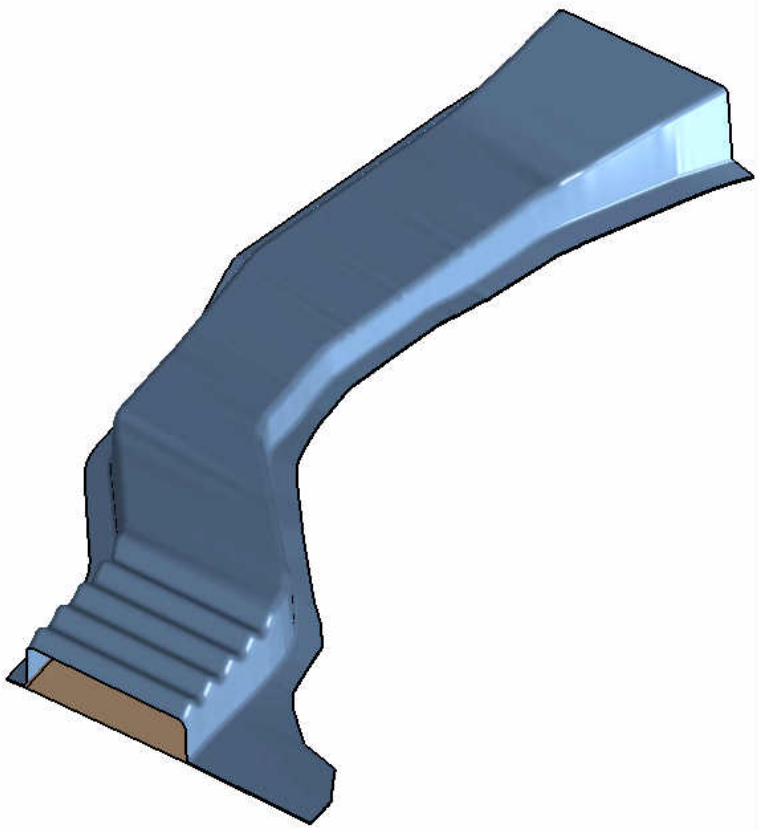

**Figure 6-33 Partial wave shape of the Frontal longitudinal rail**

Figure 6-33 shows partial wave shaped frontal longitudinal rail. The bottom plate is kept unchanged, while the top surface of the open hat section of the longitudinal frontal rail is changed into five short waves in the front section of the frontal longitudinal rail. Since the full wave model along the entire length of the rail showed a large decrease in energy absorption and resistance for crushing, the short waves are built only in the local region in front of the initial bend in the rail. It is hoped that this will help produce

controllable crush in the front section, without changed the global behavior of the longitudinal rail. A fillet of radius 5 mm provided at the sharp edges of the new top stepped shape frontal longitudinal rail.

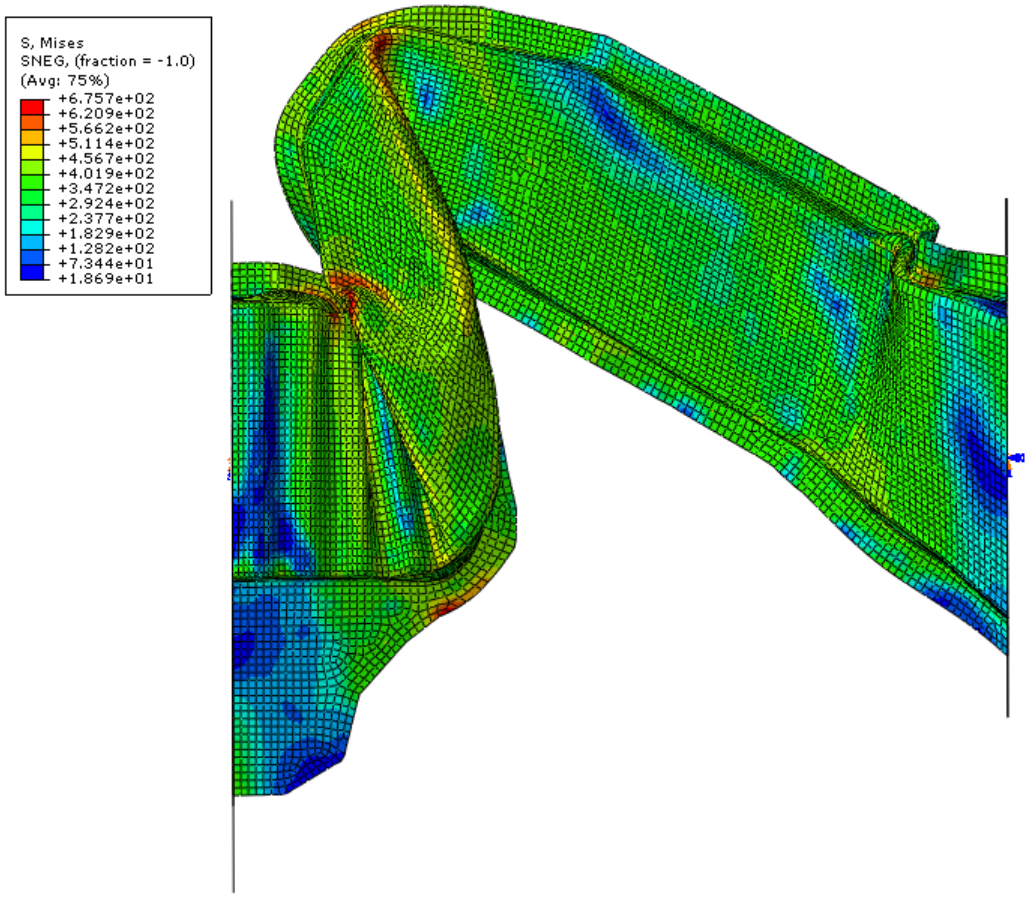


**Figure 6-34 Contours of Von-Mises Stress for crushing the partial wave shaped frontal longitudinal rail**

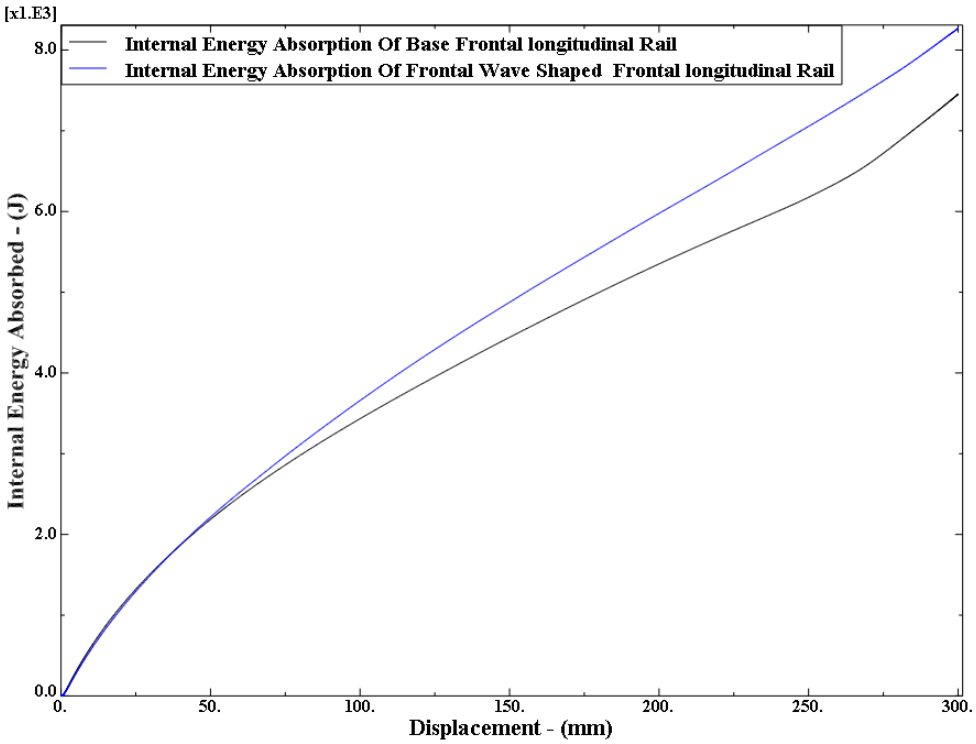


**Figure 6-35 Comparison internal energy absorbed by the base and partial wave shaped frontal longitudinal rail**

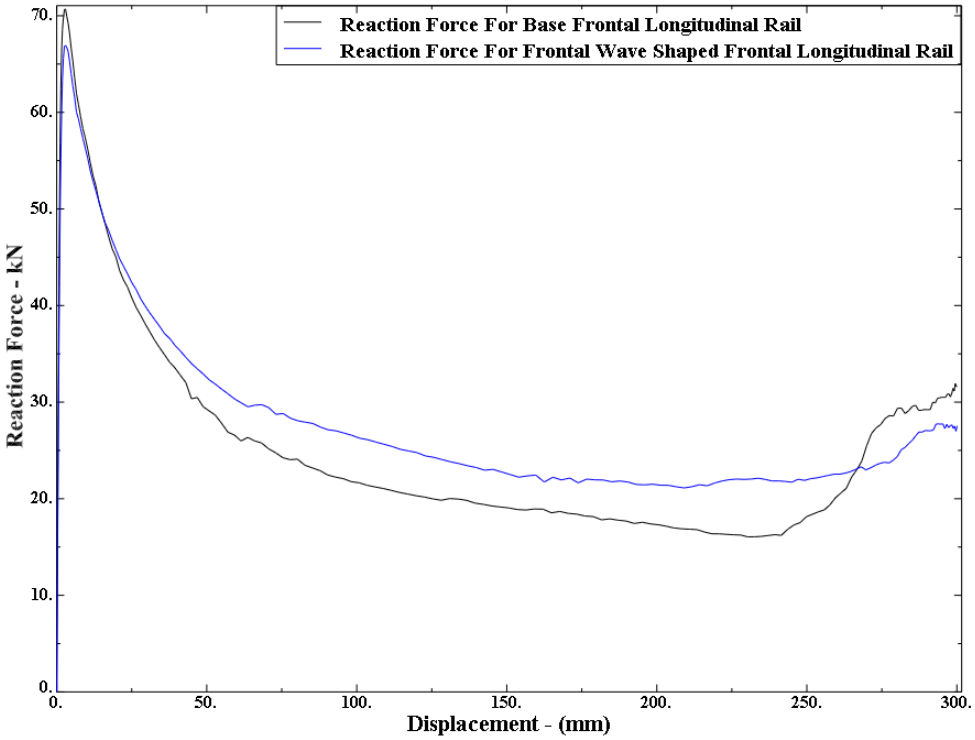


**Figure 6-36 Reaction force measured measure for partial wave shaped longitudinal rail at the fixed rigid wall**

A rigid mesh independent spot weld of diameter 6mm is created on both the sides of the flange at an equal spacing of 50 mm. The partial wave shape longitudinal rail crushed to a distance of 300 mm for a time of 200 ms. Figure 6-34 shows the Von-Mises stress distribution and mode of deformation of the partial wave shape frontal longitudinal rail. Figure 6-35 shows the comparison for internal energy absorption of both base and partial wave shape frontal longitudinal rail. The base frontal longitudinal rail reached a maximum value of 7449.5 Joule Energy absorption while the partial wave shape reached a value of 8259.78 Joules; about 10 % higher energy absorption compared to the base

frontal longitudinal rail. Figure 6-36 shows the dynamic mean crushing force vs. displacement plot for the partial wave shape frontal longitudinal rail. A peak force of 66848.8 N is reached during the initial crushing of the longitudinal rail. The specific energy absorption for base longitudinal rail is 1582.33 J/Kg and the crush force efficiency is 35.56 %. The Partial wave shape frontal longitudinal rail showed an increase of 4 % in crush efficiency.

Table 2-3 summarizes results for all the different shapes studied. Base on the crushing force efficiency comparison, the M-shape and the partial sinusoidal wave shape showed a very high increase in energy absorption. A comparison of the internal energy for the M-shaped and partial sinusoidal shapes with the base configuration is shown in Figure 6-37. Figure 6-38 shows the internal energy of the other shapes that had lower energy absorption compared to the base rail.

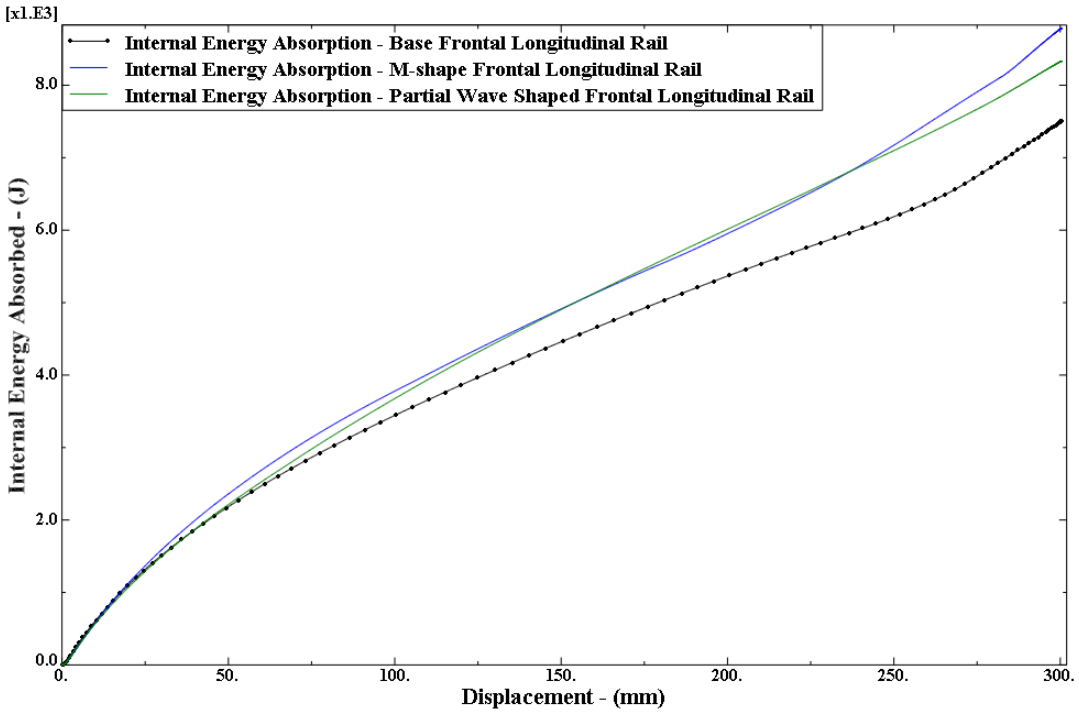


**Figure 6-37 Comparison of internal energy absorbed by the base, partial wave and M-shaped frontal longitudinal rails**

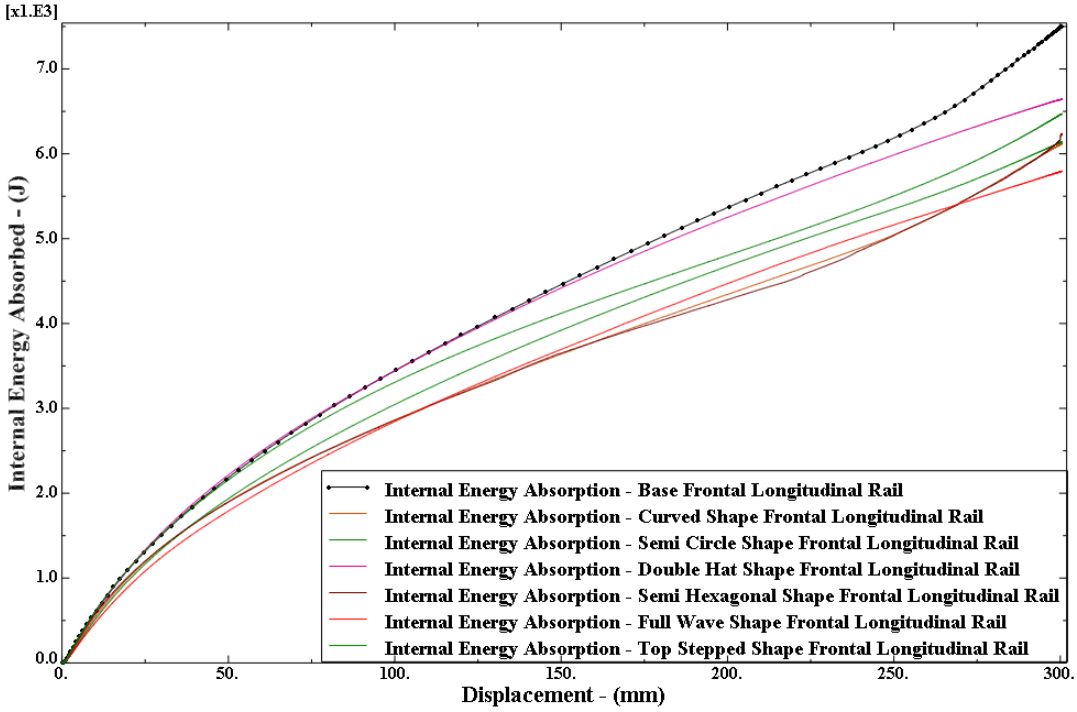


**Figure 6-38 Comparison of internal energy absorbed by different frontal longitudinal rails**

| Frontal Longitudinal Rail Shape | Weight-(kg) | Specific Internal Energy (Joules/kg) | Peak Force (N) | Crush Force Efficiency |
|---|---|---|---|---|
| Base | 5.14 | 1449.3 | 70692 | 41.2 |
| Semi Hexagon | 4.91 | 1188.1 | 68049 | 34.7 |
| Semi Circle | 4.92 | 1245.7 | 59714 | 38.2 |
| Curved Top | 5.0 | 1222.9 | 65664 | 37.0 |
| M-Shape | 5.80 | 1514.7 | 66257 | 50.3 |
| Double Hat | 5.04 | 1327.3 | 68910 | 35.6 |
| Stepped top | 5.30 | 1219.6 | 74332 | 34.5 |
| Full Sinusoidal Wave | 5.32 | 1088.0 | 55287 | 37.2 |
| Partial Sinusoidal Wave | 5.22 | 1582.3 | 66848 | 45.0 |

**Table 6-1: Shape study result summary**

## 6.10 Beads Study of Frontal Longitudinal Rail

Figure 6-39 shows shapes of one, two, three and four beads in the front section of the longitudinal rail. Results for energy absorption are shown in Figure 6-40. Table 6-2 summarizes results for specific energy absorption, peak force and crush force efficiency. The most energy absorbed per kg is achieved with 2 step beads with significantly improved crush force efficiency and reduced peak force. Figure 6-41 shows the shape with 2 beads and a small rib forming a notch at the corner of the bend region. Results for energy absorption is shown in Figure 6-40 and results for energy absorption and crush force efficiency are given in Table 6-3. Results indicate that adding this small rib helps initiate controlled crush and further increases energy absorption and crush force efficiency.

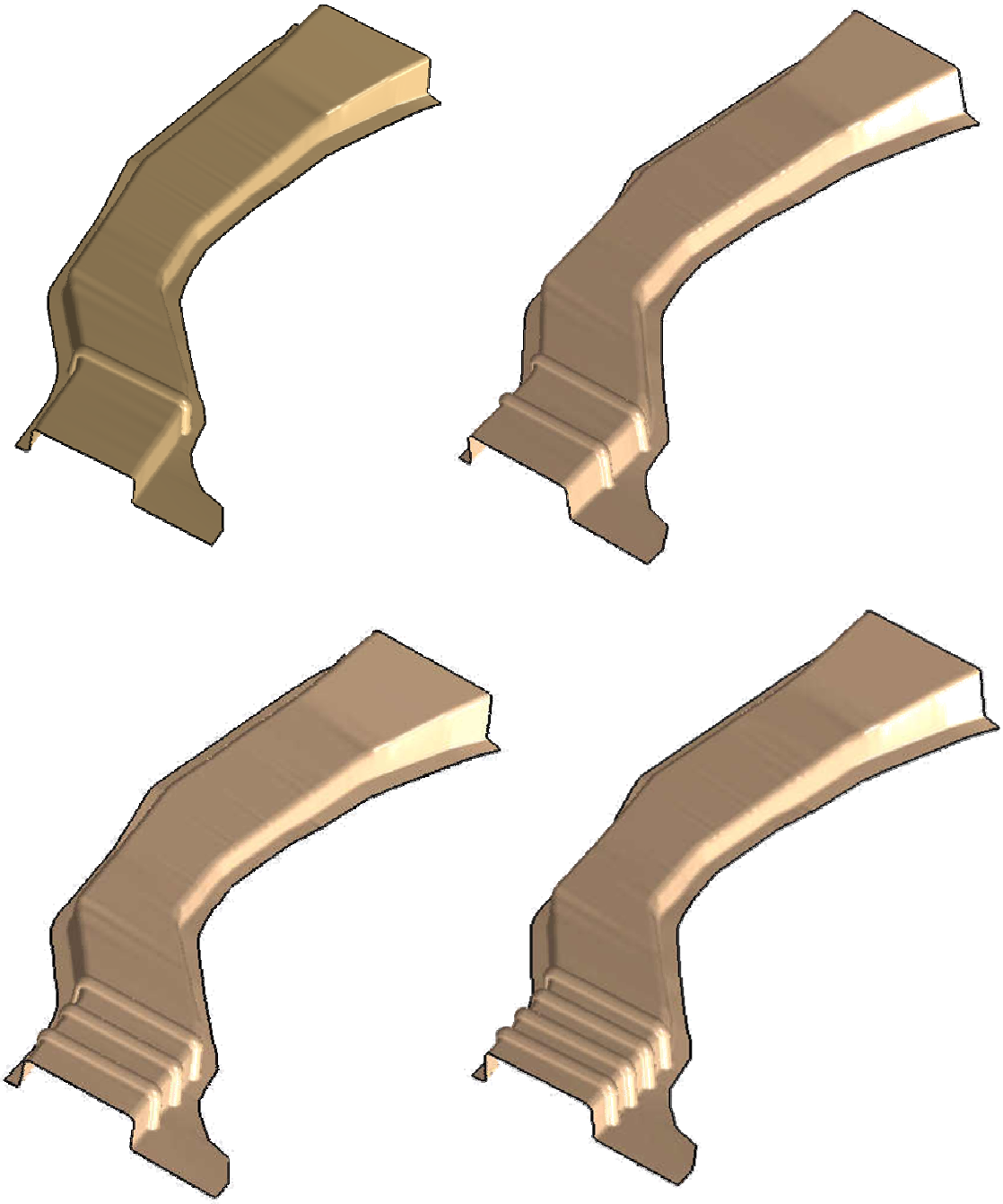

**Figure 6-39 Beads shape study (1, 2, 3, and 4 beads) of the Frontal longitudinal rail**

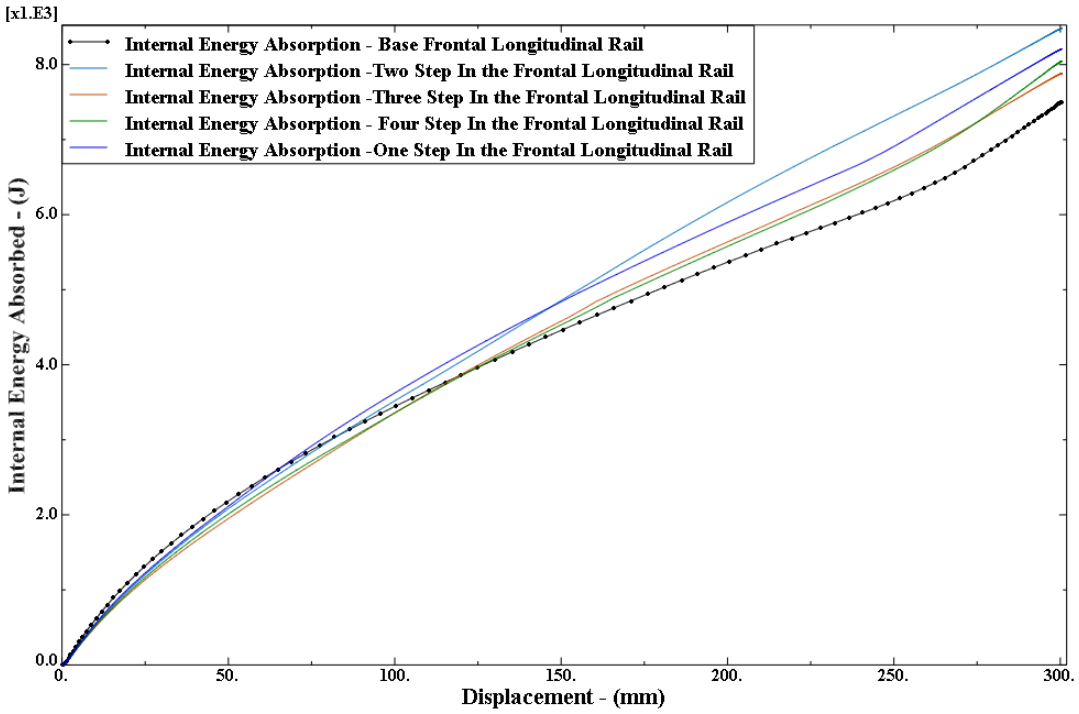


**Figure 6-40 Comparison of internal energy absorbed by the base with 1, 2, 3, and 4 beads for frontal longitudinal rails**

| Frontal Longitudinal Rail | Weight- (kg) | Specific Energy Absorbed (Joules/kg) | Peak Force- (N) | Crush Force Efficiency (%) |
|---|---|---|---|---|
| Base | 5.14 | 1449.3 | 70692 | 41.2 |
| 1-Step | 5.18 | 1584.3 | 64183 | 45.3 |
| 2-Step | 5.22 | 1623.8 | 61971 | 47.3 |
| 3-Step | 5.24 | 1499.6 | 60574 | 47.4 |
| 4-Step | 5.28 | 1514.1 | 61131 | 49.0 |

**Table 6-2: Bead study result summary**

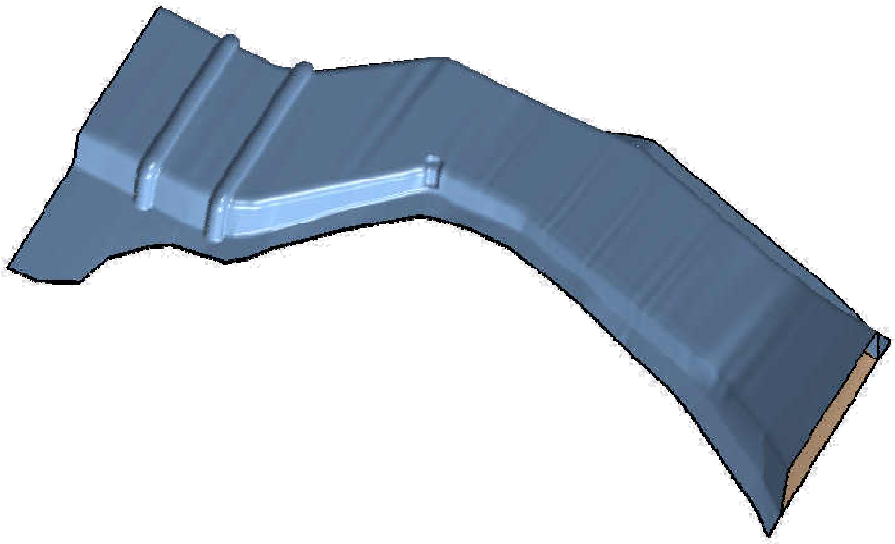

**Figure 6-41 Study of the Frontal longitudinal rail with beads and Notch in Bend Section**

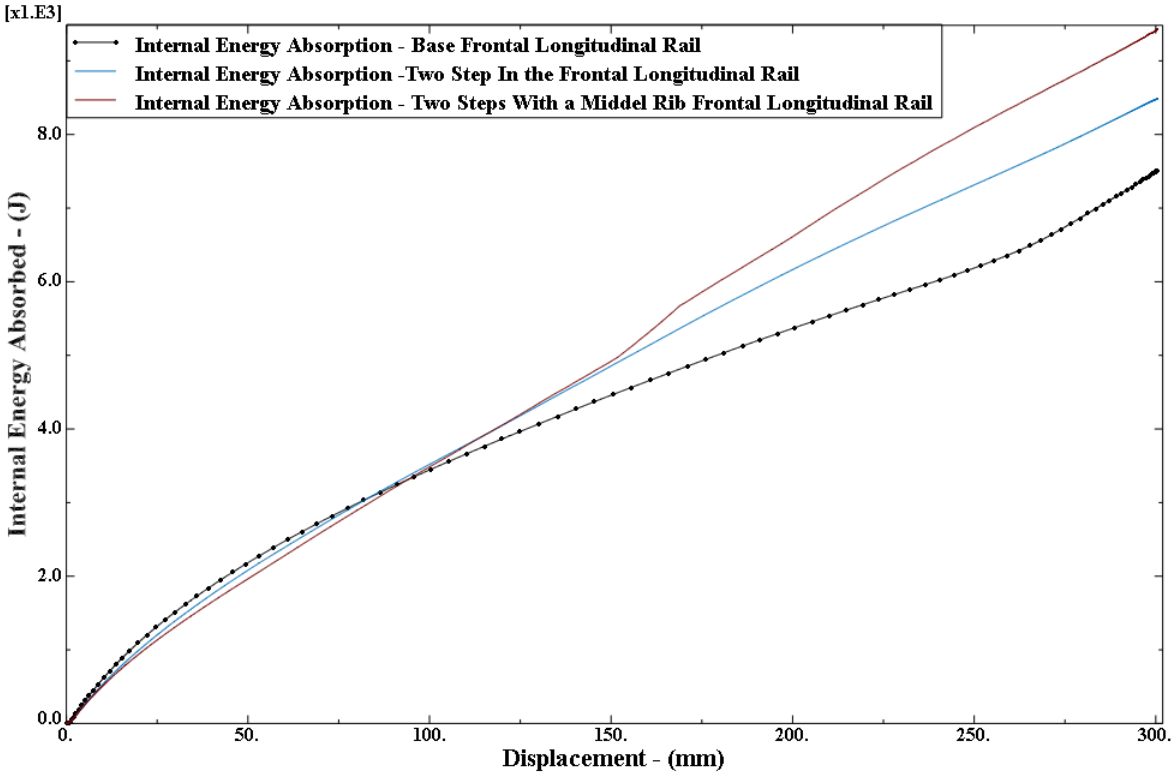


**Figure 6-42 Study of Middle Rib Crush Initiator for the Frontal longitudinal rail**

| Frontal Rail | Weight-(kg) | Specific Energy Absorbed (Joules/kg) | Peak Force (N) | Crush Force Efficiency (%) |
|---|---|---|---|---|
| 2-Step | 5.216 | 1623.77 | 61971.3 | 47.3 |
| 2-Step with Middle Rib | 5.226 | 1787.98 | 59350.9 | 52.5 |

**Table 6-3: Middle Rib Crush Initiator study result summary**

# CHAPTER SEVEN

# CONCLUSION

In this work, different levels of complexity in spot weld modeling are examined in terms of sufficient accuracy which can be used efficiently for impact analysis. In order of increasing complexity, the following spot weld models are considered and results compared: (a) simple node-to-node rigid connection, (b) rigid mesh independent spot welds, (c) elastic mesh independent spot welds, and (d) elastic with failure mesh independent spot welds. In order to study the fundamental behavior of the different mesh-independent spot weld models, pull-out and peal tests between two thin ductile steel plates are performed which isolate different failure modes. Comparisons of reaction force versus displacement curves and internal energy versus displacement for the different types of spot weld models are given. Results indicate that the rigid connected results in a reaction force which is much larger than elastic spot welds. The spot weld model, which includes failure, follows the same path as the elastic weld but when reaching the particular failure force the reaction remains constant with additional applied displacement.

To better understand the behavior of the spot-weld models for crash analysis on a realistic and important automotive component which exhibits complex crushing modes with combined axial and bending a frontal longitudinal rail designed for strength and energy absorption was studied with a node-to-node rigid spot weld compared with mesh independent rigid and elastic spot weld connections. In addition to spot welds, the effect

of various shape and size parameter changes best suited for removal of kinetic energy for the rail component is studied.

The case study for the realistic bent longitudinal frontal rail has both axial and bending crush deformation. In this case, the single node-to-node spot-weld model showed 2% higher energy absorption compared to elastic spot weld, and the rigid mesh independent spot weld showed 4% higher energy absorption compared to the elastic mesh independent spot weld. The variation in energy absorption is about 2 % to 4 % on a component level for the front longitudinal rail studied. It is hypothesized that since the energy absorption predicted by the different types of spot weld models are not that different, the spot welds are not directly loaded as severely as in the simple peel and pull-out tests. However, even a change in a few percentage points in energy absorption could have a much larger effect on the acceleration outputs for a full vehicle during crash analysis. The studies on independent peel and pull-out tests show that spot-weld models which include failure will provide more accurate results when compared to another spot weld modeling for crash analysis. However, it is not clear that the difference in accuracy is significant for components with combination of loads such as the bent frontal longitudinal rail component studied. It is hypothesized that if the component is designed properly such that combined loads applied to spot-welds are minimized, the difference in spot weld modeling is not as critical. However, if high loads on the spot-welds cannot be avoided, especially during severe crushing and distortion where local peel can occur, then the more complex spot-weld models that include elastic properties and failure criteria will be important, as demonstrated by the simple peel and pull tests.

Different shapes like semi hexagonal, semi circular, curved top, M-shaped, double hat, stepped top, full sinusoidal wave and partial wave frontal longitudinal rail where studied to improve the energy absorption. The shapes like semi circle, semi hexagon, double hat and stepped top showed more than 10 % reduction in energy absorption and also loss of crush force efficiency and therefore did not improve the design. Even though the mass of the M-shape longitudinal rail is 0.8 kg higher than the base front rail, there was about 17 % increase in the energy absorption and significant improvement in crush force efficiency. Apart from M-shape, the partial sinusoidal wave shape showed 10% higher energy absorption compared to the base frontal longitudinal rail with a very small 0.1 kg increase in the mass. The use of beads in the front region significantly increases the energy absorption and crush force efficiency of the rail. Adding a small rib in the bend of the rail helps initiate controlled crush and further increases energy absorption and crush force efficiency.

## Future Work

In this Section, suggestions for extending the work in this study are offered:

- The empirical stiffness equation for elastic spot weld models given in [16] is not unique. Alternative models which depend on plate thickness could be proposed and validated. In addition, nonlinear stiffness relations could be developed.
- The study on spot-weld failures like peel, pull, shear and twist are uncoupled and each failure mode was studied individually. To couple these individual failure modes, experiments of spot-weld failure could be conducted. Based on the

experimental values, a more accurate failure model for spot welds can be developed.

- By default in ABAQUS, a damage initiation criterion is specified in terms of forces/moments in the connector. The damage initiation criterion can be specified in terms of an equivalent relative plastic motion in the connector. The user can provide the relative equivalent plastic displacement/rotation at which damage will be initiated as a function of the relative equivalent plastic rate. Suggested future work is to include damage initiation criterion in the spot weld models and compare results for the spot weld models with elastic failure, but with no damage.
- The results on energy absorption for the case study on different types of spot weld models on the frontal longitudinal rail did not show a clear difference of energy absorption between simple rigid and more complex elastic mesh independent spot welds. In addition, results using spot welds which have accurate coupled failure models should be investigated to see if a clear difference in energy absorption can be seen; especially for spot welds which may fail locally during high speed and large crush deformation with rapid energy change.
- To quantify how the variation in spot-weld complexity affects the acceleration results at key locations such as driver location, the full vehicle model that includes the frontal rail component studied in this work could be investigated. This can be compared by simulating full vehicle crash with the simple node-to-node rigid spot weld and the more complex mesh-independent rigid, elastic, and failure spot weld models.

- Individual shape change studies were performed with the goal of improving energy absorption of a realistic front longitudinal rail. Optimization of the cross-section shape, beads, as well as the number, spacing, and location of spot-welds, using commercially available software linked with crash simulation codes would provide a more direct path to improved energy absorption, while maintaining light weight.

# REFERENCES


[1] Cornille Jr., Henry, “A Frontal Rail Design for Efficient Crush Energy Absorption”. IBEC', 95 Automotive Body Interior & Safety Systems. Pages (88-111)

[2] Mahmoud Y. Ghannam, Matt Niesluchowski and Patrick M. Culkeen “Analysis of a Frontal Rail Structure in a Frontal Collision” SAE International, Warrendale, PA (ISSN 0148-7191)

[3] Yu Zhang, Ping Zhu, Zhongqin Lin and Guanlong Chen , “Study on Structural Lightweight of Key Auto-Body Parts in Energy Absorption Based on Crashworthiness Simulation” SAE International, Warrendale, PA (ISSN 0148-7191)

[4] Paul Du Bois, Clifford C. Chou, Bahig B. Fileta, Tawfik B. Khalil, Albert I. King, Hikmat F. Mahmood, Harold J. Mertz, Jac Wismans, 2004 “Vehicle crashworthiness and Occupant Proctection”, American Iron and Steel Institute

[5] E. Rusi´nskia, A. Kopczy´nskib, J. Czmochowskia 2004 “Tests of thin-walled beams joined by spot welding”, Journal of Materials Processing Technology

[6] J.Fang, C.Hoff, B.Holman, F.Mueller, D.Wallerstein,“Weld Modeling with MSC.Nastran”.

[7] Zaouk, A. K., Marzougui, D. and Kan, C.D.(2000) “Development of a Detailed Vehicle Finite Element Model Part II: Material Characterization and Component Testing”,International Journal of Crashworthiness

[8] Matteo Palmonella, Michael I. Friswellb, John E. Mottershead, ArthurW. Lees, 2004 “Guidelines for the implementation of the CWELD and ACM2”, Finite Element Analysis and Design spot weld models in structural dynamics, pp 193-210

[9] P. Wung, 2006 “A force-based failure criterion for spot weld design” Experimental Mechanics, Volume 41, (ISSN 0014-4851)

[10] Seeger, F., Feucht, M., Frank, T., Keding, B., Haufe, A. (2005). An Investigation on Spot Weld Modelling for Crash Simulation with LS-DYNA. LS-DYNA

[11] Karl D. Majeske, Patrick C. HammettI, “Identifying Sources of Variation in Sheet Metal Stamping”, International Journal of Flexible Manufacturing Systems, Volume 15, Number 1 / January, 2003

[12] Davies, Geoff,2003, “ Materials for Automobile Bodies”, Butterworth-Heinemann, ISBN-10: 0750656921

[13] DASSAULT SYSTEMS, Simulia, “ABAQUS: Analysis User’s Manual”, ABAQUS Documentation V6.8.

[14] Xin Sun, Mohammad A. Khaleel, 2006 “Dynamic strength evaluations for self-piercing rivets and resistance spot welds joining similar and dissimilar metals”, International journal of impact engineering ISSN 0734-743X

[15] Omar Faruque, Nripen Saha, Kiran Mallela, Tau Tyan, Chelliah Madasamy, Thierry Guimberteau, 2006 “Modeling of Spot Weld under Impact Loading and Its Effect on Crash Simulation” SAE International, Warrendale

[16] Lu, G. and Yu, T.X., 2003, “Energy Absorption of Structures and materials”, Woodhead Publishing Limited: Cambridge England, Boston, New York, Washington DC.

[17] Smith Robert, “Energy Absorption of Sine Wave Beams Subjected to Axial Impact Loading” M.S. Thesis, Clemson University, 2007.